Natali Unterberger, BSc

Development of a High Temperature Rheometer for Extensional Rheology and Examination of Polymer Solutions and -Melts under Free Surface Flows

Master's Thesis

to achieve the university degree of

Master of Science

Master's degree programme: Technical Chemistry

submitted to

Graz University of Technology

Supervisor

Priv.-Doz. Dipl.-Chem.Univ. Dr.rer.nat. Frank Wiesbrock

Institute for Chemistry and Technology of Materials

Company Partner: Anton Paar GmbH
Dipl.-Ing. Dr.techn. Wolfgang Baumgartner
Dipl.-Ing. Dr.mont. Matthias Walluch
Dipl.-Ing. Alexander Troiss

Graz, Februray 2021

Affidavit

I declare that I have authored this thesis independently, that I have not used other than the declared sources/resources, and that I have explicitly indicated all material which has been quoted either literally or by content from the sources used. The text document uploaded to TUGRAZonline is identical to the present master's thesis.

10.02.2021	
Date	Signature

Eidesstattliche Erklärung

Ich erkläre an Eides statt, dass ich die vorliegende Arbeit selbstständig verfasst, andere als die angegebenen Quellen/Hilfsmittel nicht benutzt, und die den benutzten Quellen wörtlich und inhaltlich entnommenen Stellen als solche kenntlich gemacht habe. Das in TUGRAZonline hochgeladene Textdokument ist mit der vorliegenden Dissertation identisch.

10.02.2021	
Datum	Unterschrift

Introduction

Extensional rheology is useful in many industrial processes. Many processing units and flow fields incorporate extensional deformations. During elongation deformation, polymer chains get stretched, which can result in significant modifications of the flow behavior. (1) These extensional properties can cause problems during processing. Thus, the understanding of the material behavior in extensional deformation is crucial for successful processing.(2) (3)

From research, it is known that a polymeric fluid or melt can exhibit similar properties in shear and oscillation rheology despite differences of the molecular structure.(4) In shear rheology, a spherical polymer coil is deformed to an elliptic structure in dependence of the shear rate.(5) In uniaxial elongation deformation, the polymer chains get stretched and orientated. Irrotational extensional flows are able to uncoil and orientate molecules in a much stronger way than shear flows can do.(2) Thus, extensional analysis can reveal differences in the microstructure and chain architecture of the sample.(4)

The extensional behavior of fluids can be tested by filament stretching or capillary break-up rheology, for which the capillary break-up extensional rheometer (CaBER) becomes relevant at shear viscosities lower than 10^3 Pa·s. (6) The CaBER apparatus was developed by the Cambridge Polymer Group.(7) Over the past 15 years, many papers were published in the field of CaBER analysis. The analysis of the apparent extensional viscosity and additional extensional properties were examined for Newtonian fluids (8), shear-thinning fluids (9), and non shear-thinning fluids (10). Due to the fact that the endplate separation velocity is zero, filament thinning is only affected by capillary forces and gravity.(11) The inherent material properties like viscosity, density, or elasticity determine relaxation times, capillary velocities, and break-up time.(10) During the experiment, the filament diameter evolution is plotted as a function of time, which enables the determination of the specific relaxation time, capillary velocity, and break-up time.(12) The predominant fluid thinning velocities or parameters have been identified by

Clasen *et al.* (*13*) in 2012 with the help of a PHD 4400 Hpsi syringe pump. Based on this research, it was found that the viscosity and elasticity have great influence on the yield results. Beside these parameters, also the polymer structure plays an important role.(*13*) Other comparable measurement techniques, like 4-roll mill (*14*) or opposed jet are very time- and sample-consuming.(*1*)

In general, CaBER measurements offer many advantages over other rheological investigation methods. The device covers a wide viscosity range form $5 \cdot 10^{-2}$ up to 10 Pa·s and allows the determination of free surface flows of low-viscosity fluids. During the measurement, the only influencing factors for filament thinning are capillary forces without any additional kinematic input.(*11*) Furthermore, only small sample sizes are used, and the measurement takes only a few minutes. For these reasons, CaBER measurements are suitable for numerous industrial fields like food, cosmetic and polymer industry.(*3*)

Motivation

The motivation for this master thesis was the development and evaluation of a high-resolution and high-temperature capillary break-up extensional rheometer. The extensional rheometer should enable the analysis of low-viscosity polymer melts and other high melting-point materials under uniaxial elongation. The analyses are to be used to improve the understanding of the material behavior and to predict the manufacturing process under consideration of the occurring elongation loads.

Especially polymer melts are exposed to extensional stress in many processes like film blowing, fiber spinning and extrusion. During polymer processing, occurring side-reactions can hinder or disable successful production runs. By precedent CaBER analyses, cross-linking or scission reactions can be quantified, and counter-measures can be initiated. Furthermore, the fire-retardant behavior of a polymeric material can be evaluated by melt-dripping. Thus, the measurement technique offers advantages for the improvement of industrial processes; in addition, safety issues for the product application can be clarified.

Currently, commercially available rheometers like filament stretch rheometers (FiSER) or sentmanat extensional rheometers (SER) are only suitable for high-viscosity materials. Also, the commercially available capillary break-up rheometer from Thermo Scientific (HAAKE CaBER1) shows major shortcomings for the analysis of polymer melts. Firstly, the operation temperature of the device is limited by a maximum temperature at 80 °C. This limitation makes the device unsuitable for the analysis of polymer melts, since most polymeric materials exhibit a much higher melting temperatures. Secondly, the data evolution takes place only by a laser-assisted method. Although the method provides a high temporal resolution at a fixed point, the optical evaluation by a high-speed camera offers more features. The data evaluation by a high-speed camera enables not only the measurement of the filament diameter, but also the interpretation of instability mechanisms. These instability mechanisms include effects like the

characteristic beads-on-a-string formation of viscoelastic fluids. In addition, the adhesion between the endplates and the sample fluid can be examined by this data evaluation method. The adjustment of the adherence conditions can yield more accurate experimental results.

For the development of a new high-temperature extensional rheometer, two elements are indispensable. These two elements are a heating element (Convection Temperature Device CTD) and a linear drive motor, which performs the endplate separation. The maximum operation temperature of the CTD chamber of Anton Paar GmbH is 600 °C. In addition, the chamber can be cooled by liquid nitrogen to -160 °C. Thus, the device offers a wide operation range, in which also high melting-point materials can be analyzed. Due to the fact that the chamber has no sufficient illumination for successful picture recording, a lighting concept needed to be developed. An additional indispensable element for CaBER analysis is the lower linear drive motor of the Modular Compact Rheometer (MCR) and the design of a personalized movement profile. By the programming of different endplate separation profiles, the optimum conditions can be adapted to the specific requirements of the samples.

Contents

1. State-of-the-Art

1.1. General Aspects of Polymeric Materials

The term polymer derives from *poly*, the Greek prefix for 'many', and *meros*, Greek for 'part'(*15*). Deduced from the name origin, polymers are chemical substances which consist of a great number of repeating units. The monomers are connected by covalent bonds formed during polymerization reactions, such as radical and ionic polymerizations, polycondensations or polyadditions. Most polymers are polydispersed, meaning that they consist of a mixture of polymer chains with different chain lengths and molecular weights. The dispersity index can be calculated by Equation 1.1 and indicates the width of the molar mass distribution. The molar mass distribution depends strongly on the polymerization reaction and conditions. In general, the ratio increases with increasing width of the molar mass distribution. This characteristic of polymers is important to keep in mind because a great number of physical, mechanical and rheological properties depends on the width of the molar mass distribution.

$$DispersityIndex = \frac{M_w}{M_n} \tag{1.1}$$

The *number-average molecular weight* M_n is the mean value of the frequency distribution of the molar mass. The M_n value is calculated as

$$M_n = \frac{\sum(n_i \cdot M_i)}{\sum n_i} \tag{1.2}$$

where n_i is the number of chains at a specific molecular weight M_i.(*16*)

The *weight-average molecular weight* M_w is calculated as

$$M_w = \frac{\sum(w_i \cdot M_i)}{\sum w_i} \tag{1.3}$$

and is defined as the mean value of the calculated mass distribution of the molar

mass. The abbreviation w_i is defined as the weight fraction of a specific polymer molecular weight M_i.

Generally, polymers are distinguished in natural and synthetic polymers. Examples for natural polymers are proteins and polysaccharides. The classification of synthetic polymers occurs according to different aspects, namely the chemical group, the type of polymerization, and their dynamic-mechanical behavior as a function of temperature. The different dynamic-mechanical behavior arises from their molecular structure. Possible architectures are linear or branched polymers.(*17*)(*18*)

1.2. Polymer Thermodynamics

1.2.1. Random Walk Model

The shape distribution of a polymer chain can be described with the *random walk model*. Due to micro-Brownian motion, the macromolecule is able to undergo conformational changes in shape. The rotations around single σ-C-C bonds enable changes in the orientation of the main chain. These rotations are thermally induced. The number of possible conformations is important since it gives the chain contribution to the entropy of the polymer system.(*19*)

The probability function of the random walk model is given by the *Gaussian approximation*, if the number of repeating units is large and the completely stretched conformation does not play a significant role. Exceptions are very stiff polymers, polymers with a very low degree of polymerization, rubbers at large deformations, and materials with frozen stresses at high degrees of orientations.

The mean square distance can be calculated by Equation 1.4, in which W(r)dr is defined as the probability of a chain with an end-to-end distance between r and

r+dr. The term b indicates the bond lengths between the segments n.

$$< r^2 >= \int_0^\infty r^2 W(r) dr = nb^2 \tag{1.4}$$

The dimension of the coil is calculated with the *radius of gyration* s.

$$< s^2 >= \frac{1}{6} < r^2 > \tag{1.5}$$

Figure 1.1 represents the difference between the end-to-end distance and the radius of gyration.

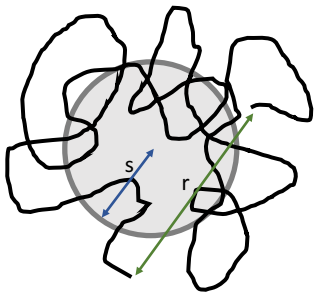

Figure 1.1: End-to-end distance (r: green) and the radius of gyration (s: blue) of the random walk chain.

In solution, the coil radius depends on the molar mass, the interactions with the solvent, and internal mobility of the macromolecule.(*18*) In conclusion, the micro-Brownian motion causes intrinsic stability and instability of a colloidal particle.

1.2.2. Gibbs Free Enthalpy

A binary system consists of a polymer (P) and a solvent (S). Per definition, a solution is ideal if:

$$\mu_i = \mu_i^\circ + RTlnx_i \tag{1.6}$$

is valid for each chemical potential μ_i. The abbreviation x_i designates the mole fractions and μ_i° the molar chemical potential in the pure state. The *free enthalpy of*

mixing G_m is the difference between the enthalpies after and before the dissolving process (Equation 1.7).

$$\Delta G_m{}^{ideal} = RT \sum_i n_i ln(x_i) \tag{1.7}$$

The index m acronyms mixture; n_i is the molar amount of compound i. In a binary system, polymer-solvent, polymer-polymer, and solvent-solvent interactions take place. Due to these interactions, the mixing process causes changes of the entropy S and the chemical potential μ_i. The energy of interactions of two molecules is sketched in Figure 1.2 as a function of their distance r. At the distance r_0, both molecules are in equilibrium. At r<r_0, strong repelling forces occur due to the interactions of the electron shells. In case of larger distances, weak attractive forces occur. The depth of the energy minimum w depends on the chemical composition.

The Gibbs free enthalpy dependents on the enthalpy H and the entropy S. As a consequence of this relationship, G_m can be expressed by Equation 1.8. (*17*) (*18*)

$$\Delta G_m = \Delta H_m - T\Delta S_m \tag{1.8}$$

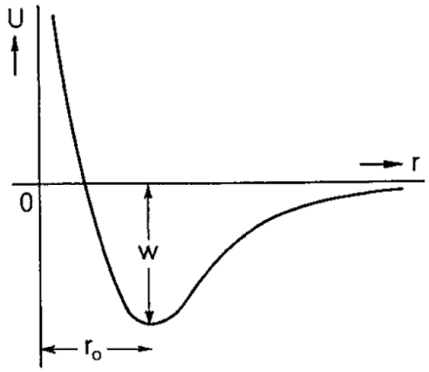

Figure 1.2: Potential energy (U) of two molecules as a function of their distance (r).(*18*)

1.2.3. Flory-Huggins Theory

The Flory-Huggins theory is based on the liquid-lattice model (Figure 1.3). It is assumed that the monomer and solvent molecules have the same size and will

arrange randomly within a lattice structure. Each lattice is set at the free volume occupied by one monomer or solvent molecule.(20)

A first approximation of the entropy of mixing S_m can be made with the *Boltzmann-entropy* (Equation 1.9). The *Boltzmann constant* k_B is $1.38 \cdot 10^{-23}$ J/K.

$$S = k_B ln(\Omega) \tag{1.9}$$

The equation reveals the relationship between the entropy S and the number of possible configurations Ω (Equation 1.10). Equation 1.10 describes the possible configuration of the solvent molecules N_s and the polymer molecules N_p on the free lattice sites N.

$$\Omega = \frac{(N_s + N_p)!}{N_s! N_p!} \tag{1.10}$$

For large values of N, the Stirlinger equation can be considered:

$$lnN! \sim NlnN - N \tag{1.11}$$

Since both particles of an ideal solution (Figure 1.3a) have the same free volume, an equal probability for occupying the free lattice sites can be assumed. Consequently, ΔH_m is zero for this model, and S_m can be expressed by equation Equation 1.12.

$$S_m = -R(n_s lnx_s + n_p lnx_p) \tag{1.12}$$

For diluted polymers (Figure 1.3b), the polarization degree plays an important rule for the calculation of Ω.

1.2.4. Tube Model

The *tube model* describes the random thermal motion of polymer molecules in concentrated solutions and melts.(21) Doi and Edwards postulated that the motion of entangled polymers resembles the motion in a tube, which is formed

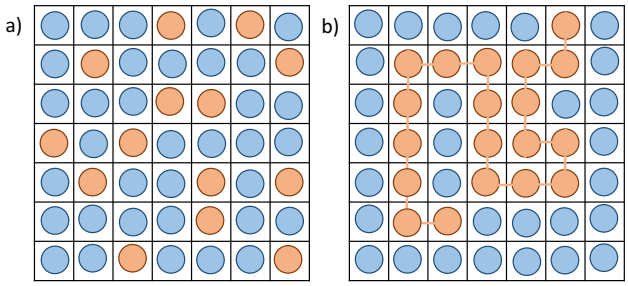

Figure 1.3: Schematic illustration of a liquid lattice. The polymer molecules are presented in orange and the solvent molecules in blue. a) Schematic illustration of diluted monomers where the solvent molecule and the monomer-molecule are of the same size. b) Schematic representation of a diluted polymer.

by the surrounding polymer chains. The friction coefficient of the diffusion along the virtual tube is proportional to the number of links N in the polymer chain. The maximum relaxation time corresponds to the time the chain requires to creep out of the initial tube.

$$\lambda \sim N^3 \tag{1.13}$$

The relaxation time λ and the molecular weight determine the viscosity.

$$\eta \sim N^3 \sim M^3 \tag{1.14}$$

For shorter unentangled systems, the viscosity and the molecular weight are proportional.(21)(22)(23)

1.3. Rheology

The word *rheology* originates from the Greek *rhein*, which means *to flow*. Thus, rheology is the science of the deformation and flow behavior of solid and liquid materials. The rheological behavior depends on many influencing factors such as type, degree, and duration of an applied load or temperature. Material properties such as concentration, chemical structure, chain length and molecular weight (and molecular weight distribution) play an important role in the rheological behavior of polymers.(24) The measuring technique of rheology is denominated as rheometry.(25) Rheometers operate with continuous rotation or rotational oscillation; also irrotational tensile tests are feasible.(5)(24)

1.3.1. Definition of the Term Viscosity

The term *viscosity* describes the fluid's resistance to flow or shear and is a fundamental characteristic of all fluids. The fluid resistance arises from inner frictions of molecules and particles. In general, all fluids consist of molecules and particles, which influence the individual viscosity of a sample: The greater the flow resistance, the higher the viscosity of the sample.(5) The term viscosity can be expressed in two different forms, namely absolute or dynamic viscosity and kinematic viscosity.(26) The kinematic viscosity ν (Equation 1.15) describes the relation between the shear viscosity η and the density ρ and can be determined if the gravitational force or the weight of the sample is the driving force. Measuring techniques of ν are, for example, the falling-ball or capillary viscometer.(5)(24)

$$\nu = \frac{\eta}{\rho} \quad [m^2/s] \tag{1.15}$$

1.3.2. Theory of Shear Rheology

The theoretic explanation of the flow behavior of a material can be accomplished by a two-plate model (Figure 1.4). In this model, the sample is placed between

two parallel plates, of which the lower one is at rest and the upper one moves at a constant speed v.

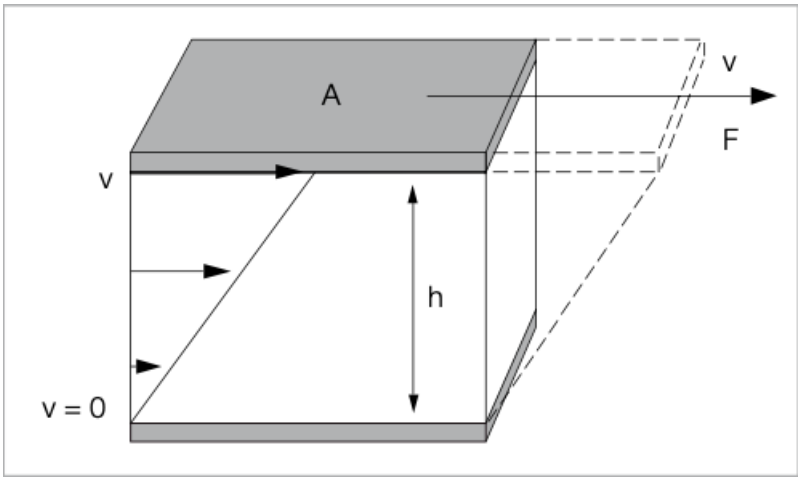

Figure 1.4: Two-plate model for shear analysis with a shear area A, a gap h and a shear force F. The resulting flow velocity is defined as term v.(5)

In theory, materials can be distinguished to show an ideal viscous or an ideal elastic behavior. Example of ideal viscous or Newtonian materials are water, silicone oil or acetone. These fluids are not able to regenerate after the deformation process, and they behave according to *Newton's law*. The relationship between the viscosity η, the shear rate $\dot{\gamma}$ (Equation 1.18), and the shear stress τ (Equation 1.17) was formulated by I. Newton and G.G. Stokes. The shear viscosity η for Newtonian fluids is defined according to Equation 1.16. According to the law of viscosity, τ and $\dot{\gamma}$ are in linear correlation (Figure 1.5). Thus, an ideally viscous flow behavior means that the only influencing factor on η is the temperature.(5)(24)

$$\eta = \frac{\tau}{\dot{\gamma}} \ [Pa \cdot s] \tag{1.16}$$

$$\tau = \frac{F}{A} \ [Pa] \tag{1.17}$$

$$\dot{\gamma} = \frac{v}{h} \ [1/s] \tag{1.18}$$

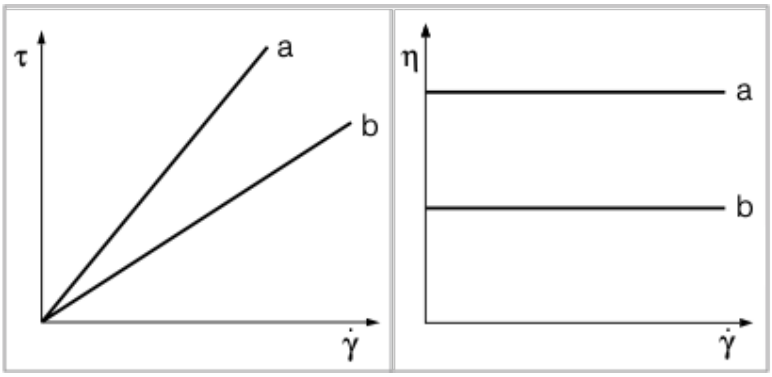

Figure 1.5: Exemplary flow curve (left) and viscosity curve (right) of a Newtonian fluid. For both samples (a: high viscosity; b: low viscosity), the viscosity remains constant over the whole shear rate range.(5)

An ideal elastic material behaves according to *Hooke's law* (Equation 1.19), according to which G is defined as shear modulus and γ (Equation 1.20) as shear strain or shear deformation. The formula describes the correlation of force and deformation of a solid material. Ideal elastic materials have the ability to store the deformation energy and regenerate after the deformation process. Therefore, the elasticity can be seen as the capacity to regain a primary shape after being deformed. The two-plate model for elastic materials is shown in Figure 1.6.(5)

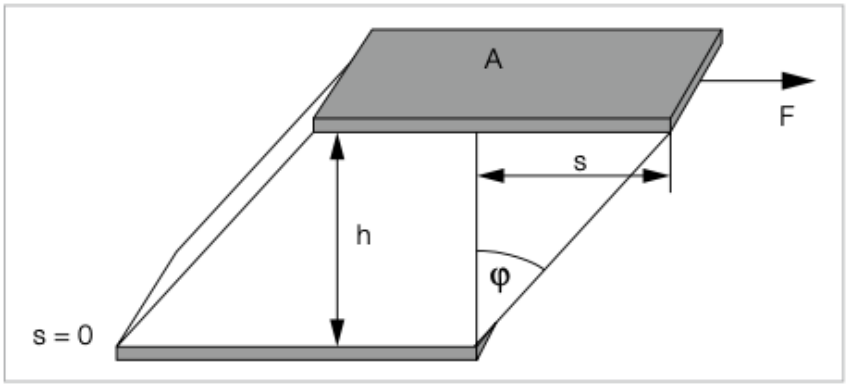

Figure 1.6: Two-plate model for shear analysis with a shear area A, a gap h, a shear force F, a deflection s, and a deflection angle ϕ. (5)

$$G = \frac{\tau}{\gamma} \ [Pa] \tag{1.19}$$

$$\gamma = \frac{s}{h} \ [1] \tag{1.20}$$

If a material shows both, elastic and viscous behavior, it is called *viscoelastic*. Examples for viscoelastic materials are glues, polymer solutions, and polymer melts. During the shear experiment, they show a shear-thinning or pseudo-plastic behavior. The shear-thinning behavior is related to the internal structures of a sample and leads to a decrease of the viscosity with increasing shear rates (Figure 1.7). A polymer solution consists of polymeric chains which are aggregated in coils. At the basis of the Brownian motion, the shape of a coil is the energetically most favorable conformation of a polymeric chain in its resting position. Under shear stress, shape transformation occur that form coils into an elliptical shapes.

These shape transformations cause polymer chain disentanglements and lead to a decreased flow resistance. The observation of a reduced shear viscosity at high shear rates can be explained by the disentanglement process. Figure 1.7 shows a typical shear viscosity curve of a non-branched shear-thinning fluid. In the region of low shear rates, the viscosity has a constant value (region 1) and is defined as zero-shear viscosity. After the shear-thinning behavior (region 2), the fluid reaches a second plateau at high shear rates (region 3). The course of the shear-thinning curve is dependent on the molecular weight and the molecular weight distribution. The shear viscosity shows a sharper gradient if the polymer has a narrow molecular weight distribution in comparison to broad molecular weight distributions. Additionally, the average molecular mass can be identified by the level of the zero shear viscosity plateau (Figure 1.8).(5)

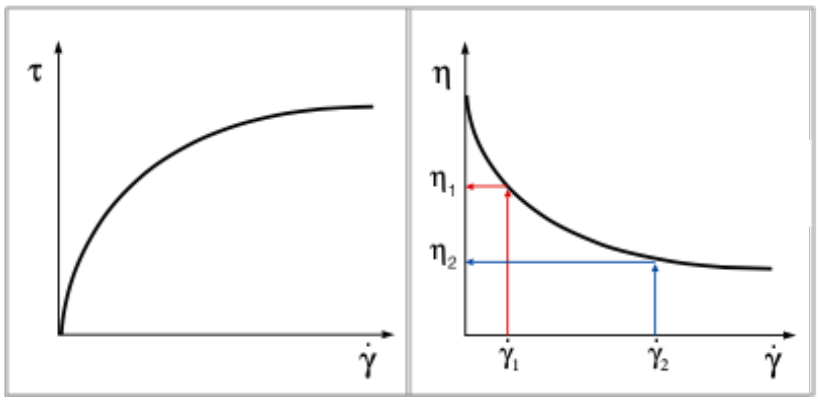

Figure 1.7: Exemplary flow curve (left) and viscosity curve (right) of a shear thinning fluid. The flow curve is obtained by plotting shear stress vs. shear rate. According to the flow curve, the viscosity function is calculated (Equation 1.16).(5)

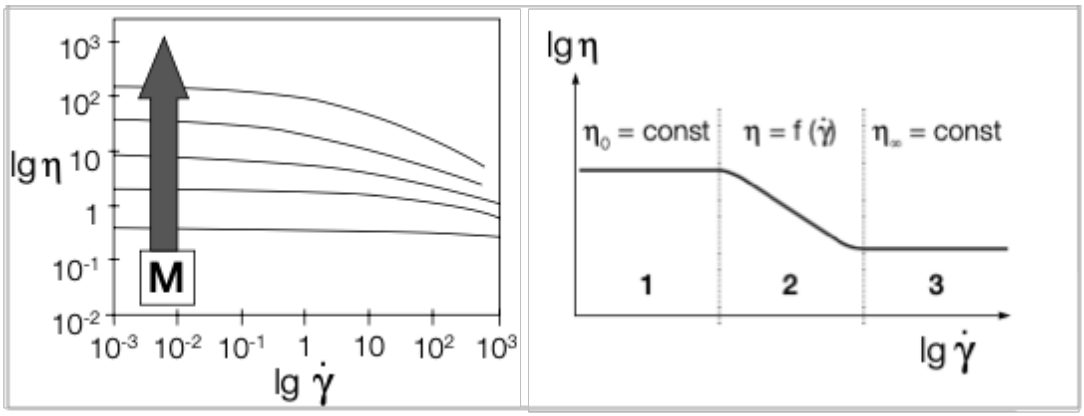

Figure 1.8: Illustration of the shear-thinning behavior of a non-branched polymer solution. Left: Viscosity curves of polymer solutions with different molecular weights. Right: Typical shear viscosity evolution of a non-branched polymer with an initial and final plateau. (5)

Beside the shear-thinning of viscoelastic solutions, also a shear-thickening behavior can be observed for filled dispersions. According to dilatant flow behavior, the viscosity increases with increasing shear rates.(5) The reason for shear thickening is the aggregation of particles into clusters at high shear rates. The main influencing factors on this rheological phenomenon are the size, shape, and softness of the dispersed particles.(27)(28)

1.3.2.1. Storage Modulus G' and Loss Modulus G''

The storage modulus G' represents the elastic amount of a viscoelastic material. The elastic component describes the ability of a viscoelastic material to return to its original shape after deformation. The resetting energy is stored in the material during the deformation without any energy loss.

The loss modulus G'', on the other hand, characterizes the viscous amount. The fluid or viscous behavior describes the energy losses due to inner frictions. The energy is transferred from deformation to heat energy and causes a dissipation of energy. Based on this theory, the amount of G' and G'' are descriptive of the behavior of the viscoelastic material. If $G' > G''$, the material has a higher input of the energy storage processes and is named viscoelastic solid. On the other hand, a material is called viscoelastic fluid if $G' < G''$. The loss factor (Equation 1.21)

describes the ratio of the storage and loss modulus. The *sol-gel transition* ($G^{'} = G^{''}$) describes the phase transition point of a viscoelastic material during the shear measurement.(5)

$$tan\phi = \frac{G^{''}}{G^{'}} \tag{1.21}$$

1.3.2.2. Amplitude-Sweep

Amplitude sweep tests are mainly performed to identify the linear viscoelastic range of a material. The results are plotted as a diagram with $\log G^{'}$ and $\log G^{''}$ [Pa] on the y-axis and the logarithmic stress sweep on the x-axis (Figure 1.9). The linear-viscoelastic region (LVE region) defines the plateau, and a linearity limit γ_L can be defined. In addition, the predominant modulus can be found according to variable deflection angles. In Figure 1.9, amplitude sweeps of two different materials are plotted. The fluid behavior changes with increasing deflection angle. Furthermore, the material property illustrated in the left and right diagram show completely different behaviors. In the LVE of the left diagram, the storage modulus G' is larger than G'', which means that the sample has a gel-like structure. For higher deflection angles, the position of the predominant modulus changes. The second material in the right diagram shows a fluid-like material behavior ($G^{'} < G^{''}$).

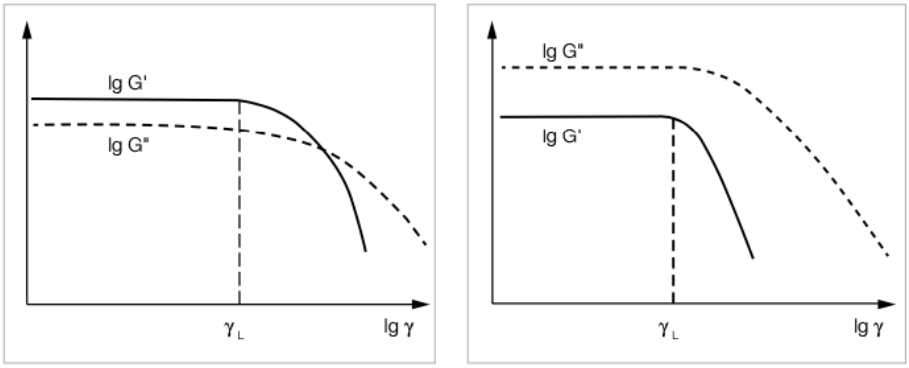

Figure 1.9: Exemplary amplitude sweep tests of two different materials. The boundary of the LVE is marked in dashed line. Left: Gel-like structure $G^{'} > G^{''}$. Right: Fluid behavior $G^{'} < G^{''}$.(5)

1.3.2.3. Frequency-Sweep

Frequency sweep analyses deliver information about the time-dependent behavior of a sample. The sample gets analyzed at a constant deflection angle and increasing or decreasing oscillatory frequency. The setting of the deflection angle describes a position in the non-destructive deformation range (LVE) obtained from precedent amplitude sweep tests. The variation between high and low frequencies is used to simulate fast or slow motions in short or long time-scales. The test is useful for the generation of information about the inner structure and molecular weight of the polymer. The typical behavior of non-branched polymers during frequency sweep tests is named *Maxwell behavior*. A predominant viscous behavior is visible at low frequencies and an elastic behavior at high frequencies. The limitations for a Maxwell behavior are defined in a curve slope of 2:1 for G' and 1:1 for G'' at low frequencies. At the transition point between predominant viscous and elastic behavior, a crossover point at a specific deflection angle is yielded at $\omega_{G''=G'}$. The crossover point in non-branched polymers is dependent on the molecular weight, meaning that the crossover point decreases with increasing molar mass. From the inverse value of $\omega_{G''=G'}$, the shear relaxation time of the sample can be calculated (Equation 1.22).(5)(29)

$$\lambda_S = \frac{1}{\omega_{G''=G'}} \quad [ms] \tag{1.22}$$

1.3.3. Design of Extensional Rheometers

The analysis of extensional flows can be performed with various methods. A general map of the commercially available extensional rheometers is provided in Figure 1.10 with their specific range of operation. The selection of the rheometer depends on the properties of the sample to be analyzed. High-viscosity materials like polymer melts can be analyzed by a filament stretch rheometer (FiSER) or a Sentmanat extensional rheometer (SER). Due to the high viscosity, the preparation of homogeneous sheets or rods is possible and enables conditions of either con-

stant deformation rate or constant stress. (*11*) The principle of a FiSER is the monitoring of tension stress and molecular conformation evolutions as a function of stretching and the total imposed strain.(*2*) Low-viscosity fluids can be analyzed with a capillary break-up extensional rheometer (CaBER). CaBER and FiSER contain two plates that are pulling apart. The sample to be examined is located between these two plates and forms a liquid bridge. The endplate displacement for CaBER is exemplarily represented in Figure 1.13.(*11*)(*12*) The main difference between these two rheological analysis methods is that CaBER imposes an initial axial step strain, and the subsequent thinning of the filament occurs due to capillary forces without additional kinematic input at the boundaries. Typically, the only measured quantity is the time evolution of the midpoint diameter of the necking filament. The relaxation time is determined by the exponential decay of the filament diameter with time.(*11*)

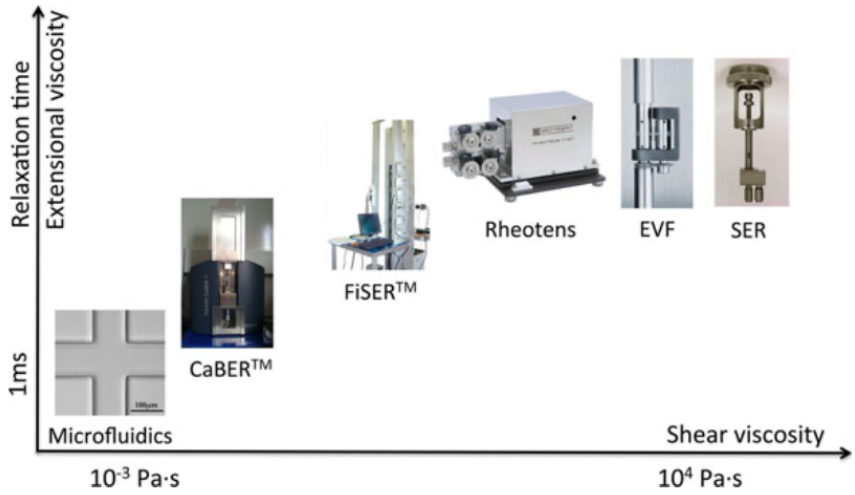

Figure 1.10: The diagram exemplifies the operational range of the different commercially available rheometers in terms of the fluid shear viscosity of the materials which are measured. The abbreviation 'EVF' stands for 'extensional viscosity fixture'.(*11*)

1.3.3.1. Filament Stretching Rheometer (FiSER)

The development of a filament stretching rheometer by Sridhar *et al.* in 1991 has enabled the characterization of extensional viscosities of moderately viscous non-Newtonian fluids such as polymer solutions.(*2*)(*10*) A basic schematic diagram

of FiSER is shown in Figure 1.11, in which the basic elements of the device are illustrated.(2) The workflow of FiSER allows the simultaneous measurement of the tensile force in the filament and the mid-filament diameter, as the endplates move apart according to a controlled separation history.

The filament gets elongated between the two endplates, which are attached to a motion control system. In an ideal uniaxial extensional flow, the extensional rate is constant, and the separation endplate profile increases exponentially with time. The filament stretching extensional rheometer imposes an exponential velocity on one or both of the end plate(s) in order to induce an uniaxial extensional flow with constant strain rate. The temporal evolution of the tensile force exerted by the fluid column on the bottom endplate and of the filament radius at the axial mid-plane of the filament are both measured and used to compute the transient extensional viscosity (Figure 1.11).(*11*)

The operating range for FiSER is limited, besides internal and elastic effects, also by the motor capacity (V_{max}) and the maximum length of the device (L_{max}). The limited range of operability for the filament stretching device is illustrated in Figure 1.12. The diagram shows the endplate velocity as a function of its position and the occurring instability mechanisms. Depending on the sample nature, different instability mechanisms are possible during the measurement, namely elastic endplate instability, internal effects, and gravitational sagging. The linear relation between V_{max} and L_{max} is defined as characteristic strain rate $\dot{E}^*$. Following this gradient, the motor limit and the maximum length are reached simultaneously.(2)

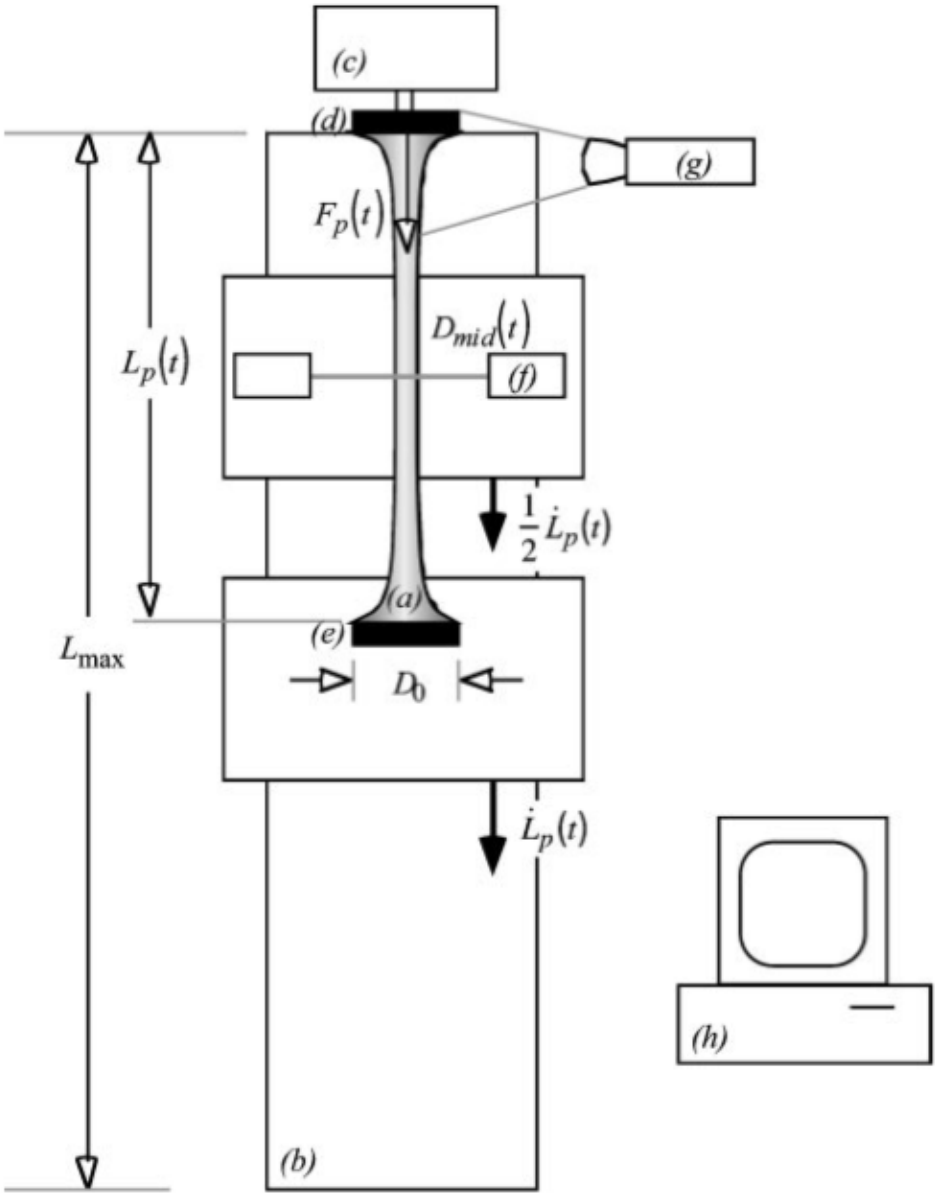

Figure 1.11: Schematic set-up of a FiSER with an illustration of the principal components of the device: a) Filament fluid. b) Linear motor. c) Force transducer. d) Upper endplate. e) Lower endplate. f) Diameter sensor. g) Optical camera. h) Computer system for control and data acquisition. (*10*)

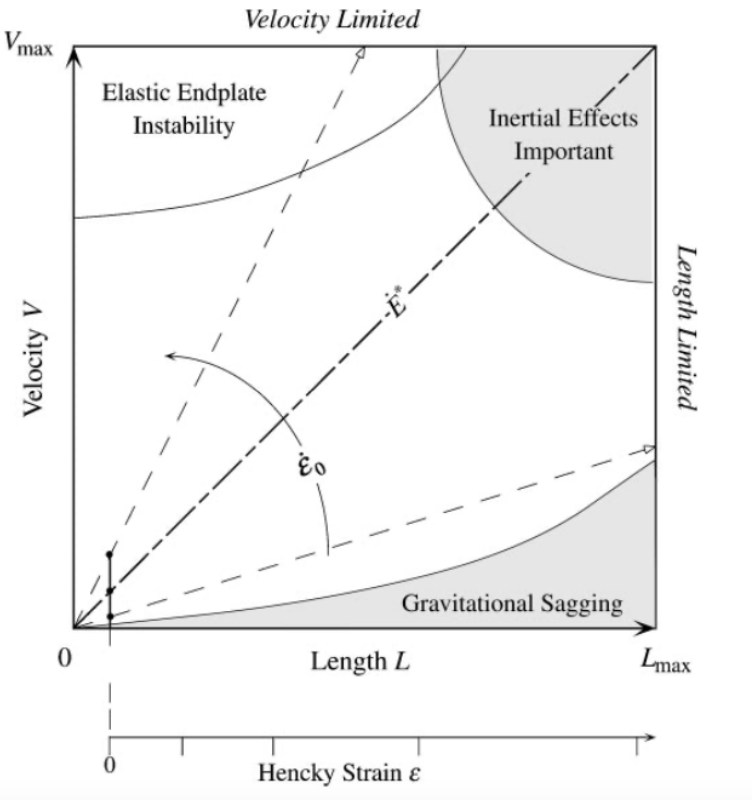

Figure 1.12: Diagram of the typical range of operation of a filament-stretching rheometer. The instabilities, which are plotted on the diagram's corners, are known to influence and constrain the operating space.(2)

1.3.3.2. Capillary Break-Up Extensional Rheology (CaBER)

Over the past 15 years, capillary break-up extensional rheometry has become an important technique for measuring the transient extensional viscosity of Newtonian fluids (8), shear-thinning fluids (9)(12), non shear-thinning fluids like Boger fluids (10), and yield stress fluids (30). Also, a huge number of biopolymers has been analyzed in CaBER experiments. (6)(31)(32)(33)(34) The technique has become especially important for fluids with a shear viscosity lower than 10^3 Pa·s.(6)

In this technique, a liquid bridge of the test fluid is formed between two cylindrical test fixtures as schematically indicated in Figure 1.13.(12) At the resting state, the liquid completely fills the gap between the two plates and exhibits a slightly convex conformation. After the elongation process, the distance between the two

plates is fixed. It can be observed that the cylindrical fluid filament that forms during the pulling-apart process continues to constrict even after the plates have stopped moving. The mechanism of this wake flow are normal stresses which relax in finite time and maintain elasticity-driven flows even after the Newtonian flow has stopped. This effect is valid only for viscoelastic liquids, but not for viscous solutions. For viscous solutions, changes in the filament diameter are only visible as long as the two plates move apart. From the development of the filament diameter, the extensional viscosity can be calculated. By the measurement of the filament diameter, the relaxation time can be determined from the slope of the curve after application against time. The relaxation time is linked to the polymer concentration n and viscosity η_s by the power law (Equation 1.23). The superscripts 'ac' and 'bc' correspond to material parameters.(35)

$$\lambda_E = n^{ac}{\eta_s}^{bc} \quad [ms] \tag{1.23}$$

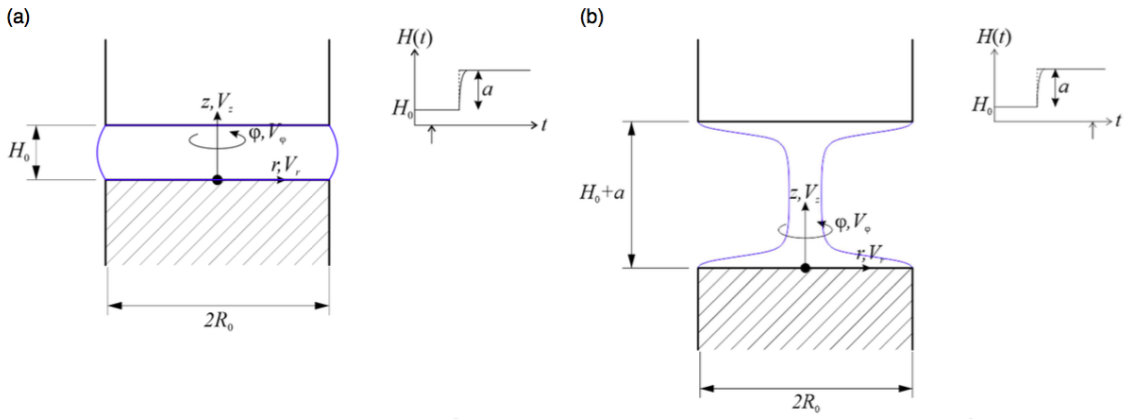

Figure 1.13: Schematic illustration of the gap ratio and the filament evolution between the two endplates. The small diagrams illustrate the development of the gap distance. a) Resting state position. b) Position after elongation.(35)

In summary, the capillary break-up rheometer provides many advantages over other extensional rheometers, like:(3)

- Small sample sizes,
- Large Hencky strains,
- Wide range of viscosities ($5 \cdot 10^{-2} - 10$ Pa·s),
- Rapid test procedures,
- Useful for food, dyes and consumer products.

1.3.4. Basics of the CaBER Technique

Extensional flows and the underlying instability mechanisms are of extreme relevance in the efficient operation of various industrial processes. Influences on processing operations and on the final product properties are caused by the orientation of polymer molecules and asymmetric particles in strong extensional flows.(11) Extensional flows are irrotational.(2) Due to the thermodynamic influences described in section 1.2, uncured polymer molecules adapt the shape of a coil at resting state. The resulting entanglements between the molecules induce increased flow resistance. During deformations, the molecules become orientated and change the properties of the material.(5) Many materials, including polymer melts and solutions, exhibit shear-thinning during shear and strain-hardening during uniaxial extension.(3)

Since characterizations under simple shear flows fail to describe the dependency on both, strain and strain rates, in strong extensional flows, the rheological characterization of materials in both, shear and extensional flow conditions, is recommended. For example, the extensional relaxation time of Boger fluids and dilute polymer solutions can be much higher than in shear rheology.(4)

For large extensions, the strain and stress can be calculated by relating the change of length L to the actual length L_0.(18) The extensional or Hencky strain rate is named after the physicist H. Hencky (1885-1951) and is detailed in Equation 1.24. The equation describes the natural logarithm of rate of extension. The deformation

rate (Equation 1.25) can be calculated by the temporal change of the sample diameter caused by the necking process. For viscoelastic fluids, the deformation rate changes exponentially with time (Equation 1.26).(5)

$$\epsilon(t) = \ln(\frac{L}{L_0}) = 2\ln\frac{D(t)}{D_0} \tag{1.24}$$

$$\dot{\epsilon}(t) = \frac{1}{L}\frac{dL}{dt}\ [1/s] \tag{1.25}$$

$$\dot{\epsilon}(t) = \frac{d\epsilon(t)}{dt} = -\frac{2}{D(t)}\frac{dD(t)}{dt} = \frac{2}{3\lambda_E}\ [1/s] \tag{1.26}$$

Early uniaxial extension determinations of Trouton *et al.* (1906) revealed that the uniaxial time-dependent extensional viscosity η_E (Equation 1.27) is three times of the time-dependent shear viscosity η_S (Equation 1.28 and Equation 1.29). In rheology, the ratio between η_E/η_S is called the Trouton ratio *Tr*.(18)

$$\eta_E = \frac{\sigma}{\dot{\epsilon}} = \frac{\sigma_{zz} - \sigma_{rr}}{\dot{\epsilon}} \tag{1.27}$$

$$\eta_S = \frac{\tau}{\dot{\gamma}} \tag{1.28}$$

$$\eta_E(\dot{\epsilon}) = 3 \cdot \eta_S(\dot{\gamma}) \tag{1.29}$$

Equation 1.30 describes time-dependent Newtonian and non-Newtonian effects that determine the flow behavior of a material. According to Renardy (1995), the evolution of the filament profile can be described by the force balance in a slender fluid filament: (8)(36)(37)

$$\boxed{3\eta_S\dot{\epsilon}} = \boxed{\frac{4F_Z}{\pi D_{mid}(t)^2}} - \boxed{\eta_{app}\dot{\epsilon}} - \boxed{\frac{2\sigma}{D_{mid}(t)}} \tag{1.30}$$

The viscous stress (red rectangle) is balanced by the tensile stress (blue rectangle) minus the elastic/non-Newtonian stress (green rectangle) and the capillary pressure (yellow rectangle).

The balance Equation 1.30 is based on the idea of Schuemmer and Tebel (1983). The tensile stress σ can be split in the axial normal stress σ_{zz} and the radial normal stress σ_{rr} in the fluid filament. In many publications, σ_{zz} was assumed to be zero; this assumption is only true if X in Equation 1.31 is one. Equation 1.31 illustrates that the surface tension force F_z is dependent on the time-dependent diameter evolution.(*10*)

$$F_Z(t) = X\pi\sigma D_{mid}(t) \tag{1.31}$$

The midpoint diameter evolution of Newtonian fluids decreases linearly with time (Table 1.1) and yields a numerical constant of X=0.7127 (Papageorgiou,1995). This result shows that the axial force is not only affected by the surface tension. Referring to Equation 1.31, a formula for the *apparent extensional viscosity* is given in Equation 1.32. The viscosity is called 'apparent' due to the time-dependent axial force during filament thinning (Equation 1.31). Therefore, CaBER experiments with simultaneous force measurement enable to determine the true extensional viscosity.(*8*)(*36*)(*37*)

$$\eta_{E,app} = \frac{(2X-1)\sigma}{\frac{dD_{mid}(t)}{dt}} \tag{1.32}$$

The diameter evolution of viscoelastic fluids occurs in an exponential way (Table 1.1) and leads to the Trouton equation (Equation 1.33). (*10*)

$$Tr_{app} = \frac{\eta_{E,app}}{\eta_0} = 3\frac{\lambda\sigma}{2D_0\eta_0}e^{\frac{t}{3\lambda}} \tag{1.33}$$

1.3.4.1. Operating Range

The uniaxial extensional viscosity is a characteristic material property and affects the filament lifetime during capillary break-up. The process of break-up is dynamic and gets accelerated by capillary forces. Capillary forces minimize the interfacial energy of the free surface of the fluid thread. The resistance of a fluid thread against surface tension and capillarity depends on the fluid composition, as well as on viscous, internal, and elastic forces. All these parameters affect the necking evolution and must be taken into account when planning extensional experiments. Especially in the case of CaBER, the liquid bridge evolves purely under the action of viscous, internal, and capillary forces, since the imposed velocity is zero. The two most important parameters for free surface flows are the *Deborah number (De)* and the *Ohnesorge number (Oh)*. The *De* number is the ratio of the time-scale for elastic stress relaxation and the *Rayleigh time-scale (t_R)* for interio-capillary break-up (Equation 1.34).(*38*) The *Rayleigh time-scale* is a time constant arising in interio-capillary processes and plays a key role in controlling the operability of filament thinning devices.(*12*) The dimensionless *Oh* number is indicative of the relation between viscous and interio-capillary effects (Equation 1.35). The calculation of t_v/t_R reveals a *Oh* limitation of 0.1418 for CaBER experiments (Equation 1.36).(*6*)

$$De = \frac{\lambda}{t_R} = \frac{\lambda}{\sqrt{\frac{\rho R_0^3}{\sigma}}} \tag{1.34}$$

$$Oh = \frac{\eta_0}{\sqrt{\rho R_0 \sigma}} \tag{1.35}$$

$$\frac{t_v}{t_R} = \frac{\frac{0.1418 \eta_0 R_0}{\sigma}}{\sqrt{\rho R_0 \sigma}} = 0.1418 Oh \tag{1.36}$$

For aqueous polymer solutions, t_R is very small. Therefore, it can be assumed that it is possible to analyze low-viscosity fluids with small relaxation times. The specific limitations were explored by Rodd *et al.* in 2005. The results are presented in Figure 1.14.(*12*)

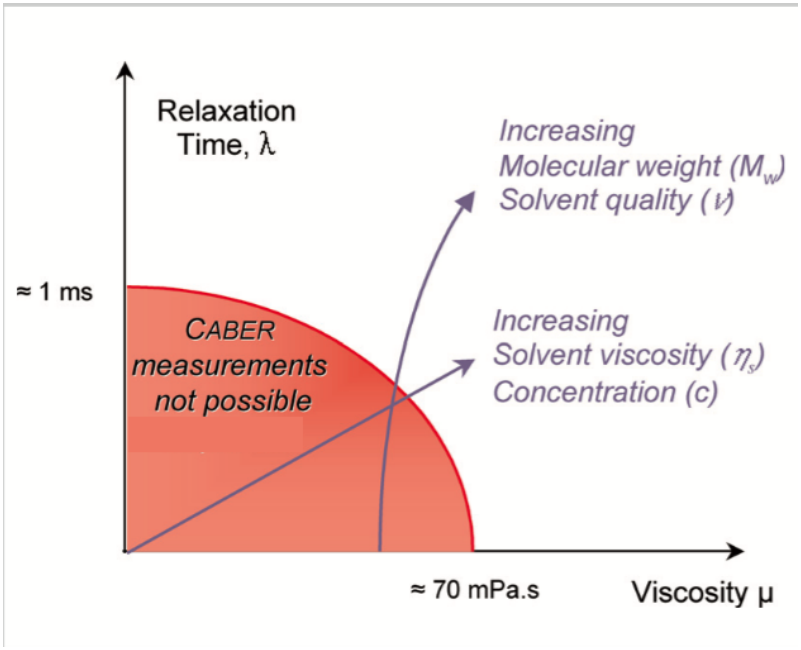

Figure 1.14: Sketch of the CaBER operational range based on the shear viscosity and relaxation time.(12)

This diagram defines a minimum limit for the measurable relaxation time at around 1 ms for liquids with a shear viscosity of about 70 mPa·s. Additionally, it was found that the relaxation time depends on the solvent viscosity and on the polymer concentration. Thus, internal effects considered in the *De* and *Oh* numbers become less important, and capillary break-up experiments become easier when increasing one of these two factors. The limitations for successful CaBER experiments are $De < 1$ for low-viscous fluids and $Oh < 0.14$ for Newtonian fluids. Additional parameters like the sensitivity to internal aspect ratio and gravity influence the operational range.(12)

1.3.4.2. Fluid-Thinning Mechanism

The behavior of different model liquids in extensional flows (Table 1.1) was analyzed in controlled dispensing experiments by Christian Clasen in 2011. (13) Based on this research, Clasen and his working group postulated three different thinning controlling velocities.

Table 1.1: Filament radius decay mechanisms and the additional parameters of Newtonian, power law fluids and elastic fluids.

Fluid	Filament radius decay	Parameters found from regression of data
Newtonian Fluid $\tau = \eta_S \dot{\gamma}$	$\frac{D_{mid}(t)}{D_0} = 0.1418 \frac{\sigma}{\eta_S}(t_c - t)$	t_c, $v_{cap} = \frac{\sigma}{\eta_S}$
Power Law Fluid (Oh<<0.2; E_C >4.7)	$\frac{D_{mid}(t)}{D_0} = \Phi(n) \frac{\sigma}{K}(t_c - t)^n$	t_c, $\frac{\sigma}{K}$, n
Elastic Fluid (Oh>>0.2; E_C <<4.7)	$\frac{D_{mid}(t)}{D_0} = (\frac{GD_0}{4\sigma})^{\frac{1}{3}} e^{-\frac{t}{3\lambda_E}}$	t_c, λ_E, $\frac{G}{\sigma}$

Viscocapillary thinning

In general, the driving force of filament thinning originates from the capillary pressure, which depends on the surface tension σ. The capillary pressure of a high-viscosity Newtonian liquid is influenced by the viscous stress and the extension rate $\epsilon\cdot$ (Equation 1.25). Assuming a cylindrical shape, this influence leads to a linear filament radius decay in time according to the evolution equation $R_{mid} \propto (t_v - t)/\eta_E$ (Table 1.1). This relationship for Newtonian fluids was firstly described by Papageorgiou (1995). (*4*) The viscosity-controlled thinning velocity (Equation 1.37) is constant and independent of the filament radius and can be determined by linear regression. Additional to the capillary velocity, also the specific viscous time for breakup t_v can be calculated (Equation 1.38).(*8*)(*13*)

$$V_\eta = 0.0709 \frac{\sigma}{\eta} \tag{1.37}$$

$$t_v = 14.1 \frac{\eta R_0}{\sigma} \tag{1.38}$$

Inertiacapillary thinning

From the investigations of Rodd *et al.*, it is known that the thinning process of fluids with a viscosity lower than $\eta_0 = 0.07\ Pa \cdot s$ is mainly controlled by inertia-capillary processes.(*12*)(*6*) For these low-viscosity liquids, the dominant resistance against surface tension originates from inertia effects. In this case, the capillary viscosity depends on the density ρ and the inverse value of the filament radius (Equation 1.39).(*13*) The critical break-up time for low-viscosity and inelastic fluids can be determined by the Rayleigh time-scale t_R (Equation 1.40).(*12*)

$$V_\rho = 0.3413\sqrt{\frac{\sigma}{\rho R}} \tag{1.39}$$

$$t_R = \sqrt{\frac{\rho R_0^3}{\sigma}} \tag{1.40}$$

Elastocapillary thinning

In viscoelastic fluids, also elastic effects contribute to the filament resistance against surface tension. Entov and Hinch (1997) showed that for an Oldroyd-B fluid the filament radius decays exponentially with time $R_{mid} \alpha exp(-t/3\lambda_E)$. In these free surface flows, the constant extension rate $\dot{\epsilon} = 2/3\lambda_E$ is directly related to the longest relaxation time. The characteristic viscosity (Equation 1.41) decreases linearly with the filament radius, and is dependent on the surface tension. The amount of elastic response can be calculated by the elastocapillary number E_C (Equation 1.42).(*4*)(*13*)(*39*)

$$V_\lambda = \frac{1R}{3\lambda} \tag{1.41}$$

$$E_C = \frac{2\lambda_S \sigma}{\eta_S \cdot D} \tag{1.42}$$

In conclusion, the filament thinning process is determined by the balance of surface tension and the resisting fluid properties (ρ, η, λ). The predominant

velocity changes over the pathway from the initial diameter to the broken filament. The general rule is that the lowest characteristic velocity determines the filament thinning. Figure 1.15 illustrates the diameter evolution of a low-viscosity fluid. In this case, the thinning dynamics are controlled initially by inertiacapillary forces (Oh<0.2077). Between Oh= 0.2077 and E_C= 4.7015, the thinning process is viscosity-controlled. Above E_C= 4.7015, elastocapillary thinning determines the diameter evolution.

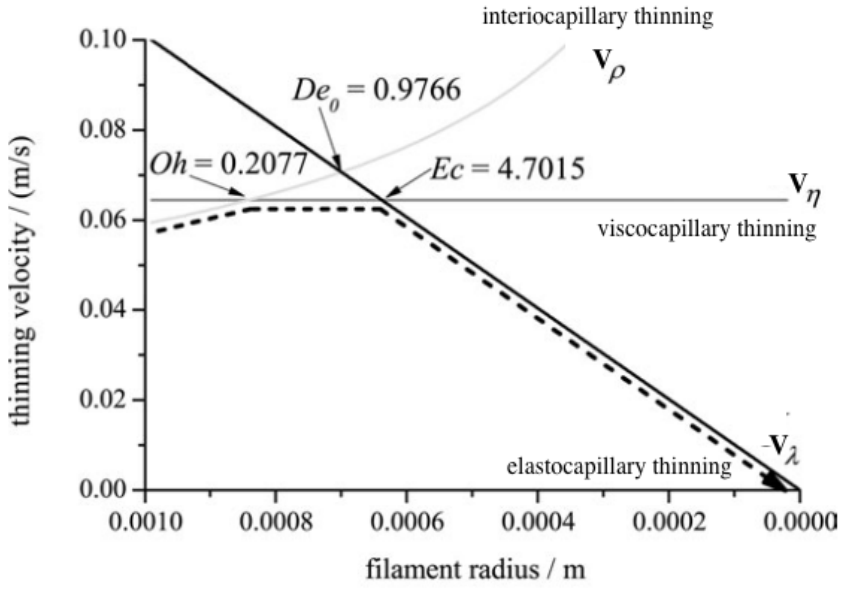

Figure 1.15: Sketch of the characteristic velocities for a low-viscosity fluid (η= 0.033 Pa·s, λ= 0.0033 s). The thinning process is marked in dashed line.(*13*)

1.3.4.3. Beads-on-a-String

The formation of 'beads-on-string' is a nonlinear dynamic process and occurs if internal stresses dominate over viscocapillary and elastocapillary stresses.(*6*)(*40*) This effect takes place in low-viscosity non-Newtonian fluids and leads to increased difficulties in the evaluation of the elastocapillary exponential decay (Table 1.1).(*41*) The phenomenon of 'beads-on-string' has been described by Goldin *et al.* in 1969.

This instability is related to the flow-induced phase separation. The polymer and solvent are segregated by the occurring large extensional strain during capillary

thinning. The solvent is enriched in the beads, while the connecting filament consists mainly of highly extended polymer chains.(3) In both situations, different forces define the size of the spheres and the thinning process of the filament. The molecules in the spherical beads are relaxed, and the size and diameter is controlled by surface tension. By contrast, viscoelastic stresses are predominant in the thin ligament.(40)

An alternative explanation for the 'beads-on-string' formation has been given by Chang *et al.* (42), who predict a regime-termed 'iterated stretching' if elastic instabilities lead to elastic recoil mechanisms close to the neck. This recoil results in the formation of smaller secondary spherical beads, which are connected to the primary drop by a thinner cylindrical thread. During the thinning process, the former primary and secondary bead become unstable, resulting in the formation of other beads.(40)

1.3.4.4. Data Evaluation

The filament diameter can be determined using optical devices such as laser micrometers or high-speed cameras. The former method provides better temporal resolution at a fixed point, whereas the latter one yields the entire diameter profile.(2) Problems with the laser-assisted method can arise from malpositioning of the laser and the narrowest part of the filament. For this reason, the usage of high-speed cameras has become more preferred. In addition, for CaBER, the data evolution by video images can extend the usage limits.(11)(12)

Oliveira *et al.* (40) and Niedzwiedz *et al.* (30) have shown that the data evolution with a high-speed camera enables not only the determination of the filament diameter, but also the analysis of occurring instability mechanisms. As mentioned before, diluted polymer solutions show beads-on-a-string formations. From image analysis, the size and diameter of the beads can be determined.

The extension of the measurable parameters is possible by normal force analysis. The normal force arises during filament stretching and can be measured by using

a highly sensitive and fast piezoelectric force sensor. This technique can be used for measuring properties like strand formation, sickness, and spreadability due to their relation to extensional viscosities. For example, Klein *et al.* measured the normal force arising in CaBER analysis of honey, glue, day care emulsions, and polystyrene solutions. The results show that normal force measurements yield information about the sample that can not be obtained with diameter evolution analysis exclusively.(*43*)

1.3.4.5. High-Temperature Mode

Understanding the flow behavior of polymer melts is important for the prediction and validation of successful polymer processing operations.(*44*) Many industrial processing routines involve elongation, namely fiber spinning, film blowing, and extrusion.(*2*) In fact, the behavior of polymer melts during extensional deformation can be influenced by the degree of branching, changes in the molecular weight distribution, the structure, and the composition of the polymer.(*44*)(*45*) Polyethylene (*46*)(*47*)(*48*)(*49*), polystyrene (*37*)(*44*)(*50*), polycarbonates (*51*) and poly(isoprene) (*52*) are prominent examples of extensional analyses according to CaBER or FiSER.

First investigations of high-temperature measurements in combination with filament-stretching rheometers were investigated by Bach *et al.* in 2002. They analyzed branched low-density polyethylene LDPE and linear low-density polyethylene LLDPE at 130 and 150 °C. The polymers were used for the investigation of the difference of (strong and slightly) strain-hardening samples under uniaxial elongation. By comparison with measurements on a commercial RME rheometer, they concluded that the high-temperature FiSER is suited to measure elongation viscosities. However, they found that FiSER is not suitable to measure extensional viscosities of strong strain-hardening polymer melts. Difficulties were caused by very rapid-necking processes of the filament. Conversely, extensional viscosities of less strain-hardening LLDPE melts were well suitable for FiSER analysis. Due to end-plate slips, each experiment was performed at least in triplicate.(*46*)

In 2015, the working group of Huang *et al.* pointed out the potential of independently controlling shear and extensional rheology. Commercial LDPE resins were analyzed at 150 °C. The experiments showed that LDPE with different linear viscoelastic properties have similar steady-state viscosity at high Hencky strain rates.(*47*)

1.3.4.6. Pre-Shear Mode

In 1987, James *et al.* described the influence of shearing during the channel flow of diluted poly(ethylene oxide) (PEO) and poly(acrylamide) (PAM) solutions. They found that the extensional viscosity of PEO solutions was largely affected by pre-shear conditions, whereas the PAM solution was not affected.(*53*) Based on these findings, further investigations were performed by the Massachusetts Institute of Technology in 2001. Newtonian and non-Newtonian fluids as well as dairy products and printing inks were examined with a modified CaBER set-up. The pre-shearing was enabled by the addition of a new bottom cylinder, which was placed in a ball bearing and attached to a motor. For Newtonian fluids like glycerol, no effects of pre-shearing were found. As expected, the filament radius decreased linearly with time. The viscoelastic fluid PEO showed a reduced filament lifetime if pre-shearing was applied, which confirmed the results from James *et al.* Similar results were found for yogurt: The pre-shearing processes cause a breakage of the gel structure and lead to a reduced filament life time. Additionally, significant effects were noted for fluids with volatile solvents. The filament life time of acrylic paints is significantly reduced by the applied pre-shearing, as pre-shearing causes solvent evaporation.(*54*)

The influences of pre-shearing in FiSER and CaBER measurements were compared by Clasen *et al.* (*4*) and Bhardwaj *et al.* (*55*). In both studies, worm-like micelle solutions were examined under pre-shearing conditions. Worm-like micelle solutions are much more sensitive to pre-shearing than polymer solutions. Filament stretching experiments show a delay of the onset of strain hardening to larger Hencky strains. Bhardwaj referred this behavior to size reductions or

changes in the interconnectivity in the micelle network.(55) Interestingly, the opposite effect of pre-shearing was observed in CaBER measurements. Pre-shearing leads to faster strain hardening and larger extensional viscosities and relaxation times. These experiments demonstrate the sensitivity of self-assembling systems not just for pre-shear, but also to the stretching dynamics.(4)

1.3.4.7. Applications of the CaBER Technology

Materials showing similar behavior at steady shear conditions can exhibit significant differences in rheological investigations in an extensional flow field. In the following section, some examples of different fields of application are given.

Food Industry
Typical flow processes in food processing include coating, spraying, pumping, filling, chewing, and swallowing. The rheological characterization involves the quantification of functional relationships between the deformation, stress, and rheological properties.(56)

Many bubbly liquids used in food manufacturing involve non-Newtonian solutions or suspensions as continuous phase. Examples like cake batters and whipped creams comprise significant volumes of air in their viscous hydrocolloid matrix. The results of Torres *et al.* using the example of water-soluble guar gum samples emphasized that the steady-state shear data are largely independent of the bubble size, whereas the dynamics of filament thinning are significantly influenced by the bubble size distribution.(57) Similar results were obtained from rheological examinations of cake batter (Chesterton *et al.* (58)).

For liquid foods, the shear viscosity is not sufficient to predict flavor perception in viscous solutions as shown by the studies of Choi *et al.*(59) It was found that interactions between salvia and xanthan gum cause an increased filament breakup time, while the presence of salvia had no impact on the shear rheological properties.(34)

Thus, the analysis of both, steady shear and extensional flow, is important for the formulation of new food recipes. Beside influences on flavor perception, also daily products like shampoos, liquid soaps, and shower gels, are affected by rheological effects. The extensional flow of products of this type occurs primarily when they are dispensed. The flow from a nozzle determines dispensing and can be classified into a dripping and a jetting regime. (*13*) Research on cocamidopropyl betaine (CAPB, zwitterionic surfactant) and sodium dodecyl sulfate (SDS, anionic surfactant), which are commonly used as surfactants in the manufacturing of home and personal care products, illustrated similar rheological behavior of worm-like micelles.

Inks and Coating Industry

Coating is the process of applying thin liquid layers to a solid surface.(*60*) In industry, different coating processes need different properties of the coating. The determination of extensional properties of typical water-based used coatings can be regulated by the addition of thickeners. As example, paper coatings and automotive spraying are compared: If automotive coatings are sprayed, short break-up times are advantageous in order to obtain the finest possible drop distribution. If paper coatings are applied with rollers, spraying and 'misting' should be prevented as much as possible, which means that formulations with long break-up times are advantageous.

Significant industrial issues in coating processes are the generation of droplets upon splitting a liquid film between two counter-rotating rolls. This process is called misting. Misting occurs for low-viscosity silicone oligomers as well as high-viscosity adhesives and inks and leads to reduced production speeds and, consequently, increased costs.(*61*)

Petroleum Industry

Controlling the extensional flow behavior of high molecular weight polymers is also useful for chemical-enhanced oil recovery. One method of chemical-enhanced oil recovery is polymer flooding. During polymer flooding, the viscosity of water is increased by water-soluble polymers, which results in a reduced water/oil mo-

bility ratio. Heavy oil production has become more important over the past years due to the expected supply short-fall in conventional oil production.(62)(63) Precedent laboratory analysis of the extensional flow behavior of polymers throughout a porous medium is important for cost- and time-saving. Viscoelasticity can provide stable sweep and, consequently, an increased volumetric sweep efficiency. However, viscoelasticity can also detrimentally cause injectivity issues that would result in the flood front delay.(62)

An exemplary analysis of enhanced oil recovery with hydrolyzed poly(acrylamide) polymers (HPAM) is given by Azad *et al.*(62)

2. Experimental Set-up and Sample Description

2.1. Experimental Set-up

The capillary thinning experiments were carried out using the air-bearing-based modular compact rheometer (MCR) from Anton Paar GmbH (Graz, Austria) with an additional lower linear drive. For these experiments, the experimental approach of capillary extensional rheology was preferred over filament stretching rheology. The maximum displacement of the linear drive is limited by the scope of the CTD (Convection Temperature Device) chamber; therefore, the MCR is unsuitable for high-temperature filament stretching operation modes. Furthermore, the temperature controlling over a small sector is much easier than for the required larger scope for filament stretching analysis. High-temperature measurements in FiSER would require a large, tall oven to enclose the whole covered distance of the extended filament. By the manufacturer of the CTD 600, a completely homogeneous temperature distribution is warranted. Due to the small required convective gas flow rates, undesired measuring impacts like air turbulences can be avoided.

The measuring system is composed of two stainless steel endplates (PP04, PP08, and measuring shaft with detachable plates 'PP06' (Figure 2.1)). For each experiment, an upper und lower endplate with the same diameter were used (Figure 2.2). In this study, endplate diameters of $D_P = 4\ mm$, $D_P = 6\ mm$, and $D_P = 8\ mm$ were used. The endplate diameter of $D_P = 4\ mm$ was used most often in this work, as the first prototype offers a limited image area of 5 x 5 mm.

Firstly, the performance of the optical set-up (Figure 2.3) aiming to efficiently picture the filament thinning during the experiment was evaluated.

A viscoelastic sample liquid of 3 wt% PEO (10^6 $g \cdot mol^{-1}$) was prepared because of its very small thread diameter during extensional deformation. The exponential filament thinning of the viscoelastic fluid was used to identify the resolution limitations of the optical set-up. Additional performance checks were made with Newtonian model liquids at room temperature (T = 20 °C). Secondly, influencing factors like temperature, initial plate separation (h_0), endplate diameter (D_P), and velocity of extension were examined. After the CaBER experiments using the MCR were successfully validated, polymer melts were analyzed at higher temperatures.

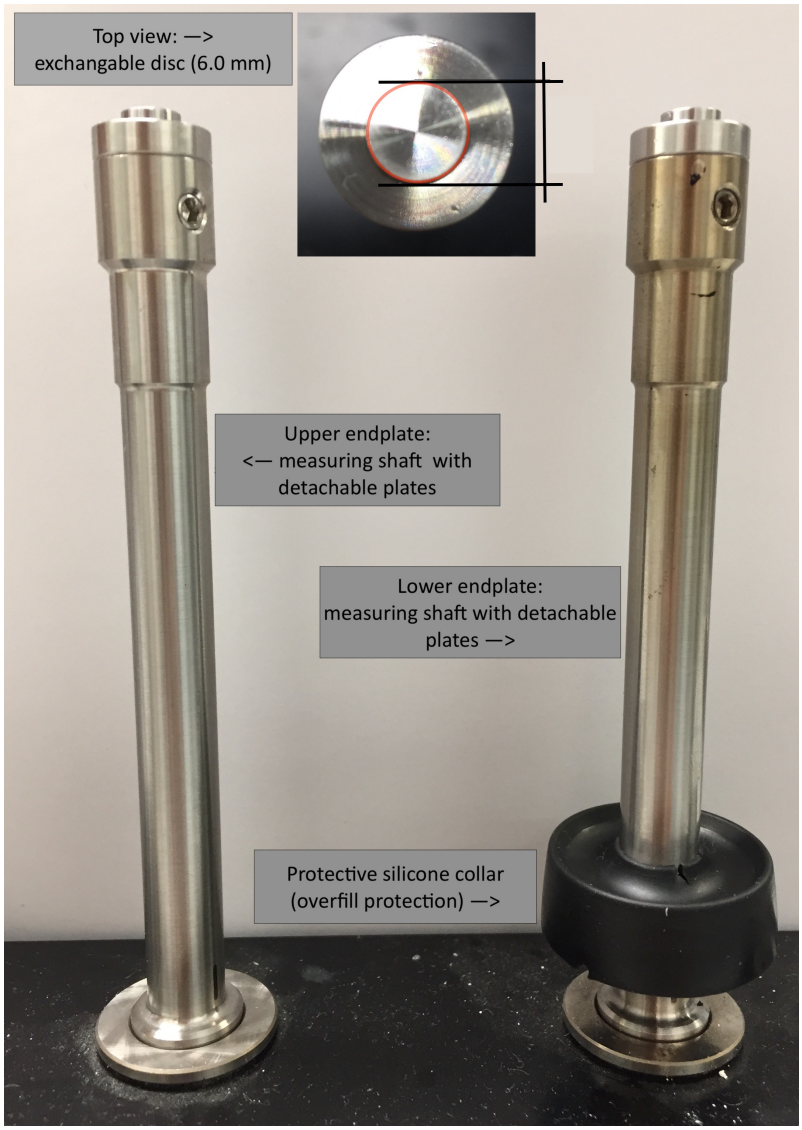

Figure 2.1: Measuring shaft with detachable plates. By exchangeable discs, an endplate diameter of D_P= 6 mm can be realized.

2.1.1. Modular Compact Rheometer (MCR)

The MCR MultiDrive enables dynamic-mechanical measurements of solid soft and liquid samples. The device consists of an air-supported upper rotational power unit and an air-supported lower linear motor. This combination enables measurements under tension, bending, and compression as well as torsional analysis of the samples (Figure 2.2). The design of the oven leads to a homogenous temperature distribution with the absence of untargeted temperature gradients and turbulences.

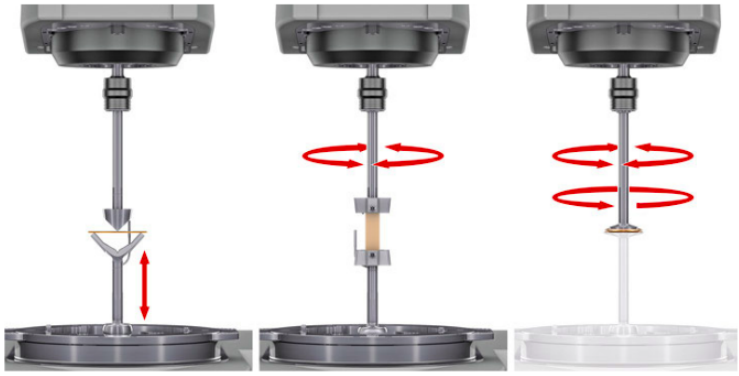

Figure 2.2: Illustration of the different application methods in the Anton Paar MCR rheometer with additional lower linear drive motor. The image at the left side illustrates an exemplary bend experiment. In the middle and right side, torsional analysis of a sample is shown. (*64*)

2.1.2. Software Rheocompass

Of high importance for the operability of the MCR rheometer for CaBER analysis is the installation of a specific software to avoid fault reporting if the measuring system drops to the bottom of the device at high separation speeds. With this adjustment, the lower endplate can be accelerated and held at the final position. The value of the final position is limited by the maximum displacement of the linear drive inside the furnace chamber to a distance of $h_f = 9.55\ mm$. The Rheocompass software is able to record the time-dependent displacement of the lower endplate. The endplate displacement is influenced by the separation speed, the initial endplate position, and the damped or non-damped run adjustments. In

general, the separation of the endplates is realizable in three different movement profiles, namely non-damped step displacement, semi-damped step displacement, and damped step displacement. The ideal speed-up and slow-down ratio was established by evaluation of the intensity and duration of oscillations after the collision. An accurate explanation of every movement profile with its advantages and disadvantages is compiled in subsection 2.2.4.

2.1.3. Optical Set-up

2.1.3.1. First Approach: Prototype 1

The MCR was equipped with additional optical features to enable the analysis of filament evolution during the stretching process in the enclosed system. The set-up of the parabolic reflector and telecentric objective is shown in Figure 2.3. From previous literature research (Table 2.1), it was found that many studies refer to the optical set-up in the work of Niedzwiedz *et al.*(*30*) They describe the advantages of the telecentric objective over a conventional endocentric objective on the examples of the absence of image effects such as monochromatic aberrations, curvature of the field of image or image distortion and chromatic aberration. In telecentric systems, only the light parallel to the optical axis passes through the lens and is analyzed. Size and shape of an image do not depend on the object's distance from the lens and position in the view field, meaning that the real dimension of the object is pictured. (*30*) Also in this study, a telecentric objective (Telecentric SilverTL^{TM}-Objective TECHSPEC) was preferred with a magnification of 2.0. The indirect lighting of the Convection Temperature Device (CTD 600) chamber was performed with a LED light and a quartz rod with cone tip on one side and a spherical area on the other side (Figure 2.4). Because of this arrangement, the heat-sensible LED light-source can be placed in a larger spacing to the CTD chamber. For directional illumination of the sample with a parallel beam bundle, it is possible to use a rotational symmetric parabolic reflector. Comparing the illumination distribution profile of LED light with (Figure 2.5) and without

(Figure 2.6) a parabolic reflector, one can see that the light distribution is more uniform if a parabolic reflector is used. Only a slightly distinct maximum can be seen in the center of the image (Figure 2.5). In general, the light can be focused parallel to the optical axis with the help of the parabolic reflector, which is favorable for picture analysis.

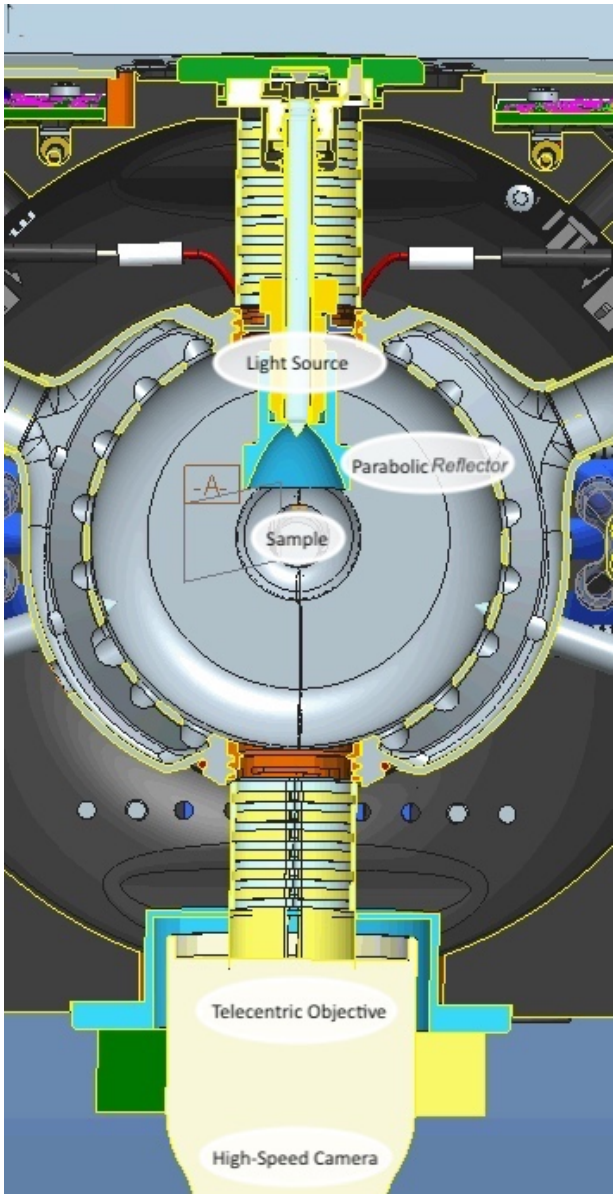

Figure 2.3: Engineering drawing of the first optical prototype. The technical sketch shows the CTD 600 chamber with additional telecentric objective, high-speed camera, and the mounted backlight illumination. For this prototype, LED light with a parabolic reflector was used.

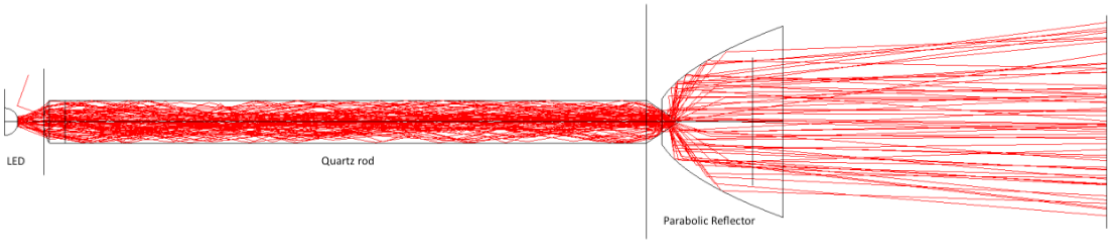

Figure 2.4: LED light source, plano-convex lens, quartz rod with cone tip, and parabolic reflector.(65)

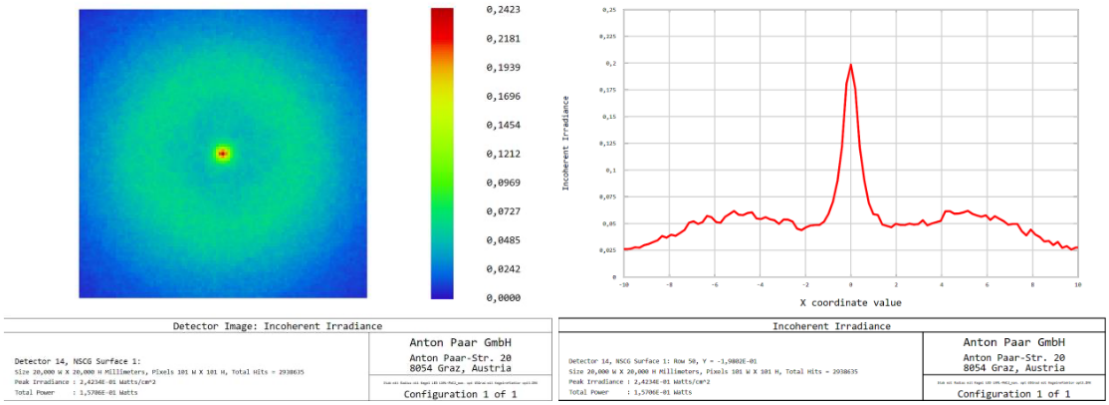

Figure 2.5: Simulation of the illuminance distribution produced by the parabolic reflector. On the left side, the illuminance inside the CTD chamber is illustrated, in which the red dot represents an intensity maximum in the middle. The diagram on the right side shows the observed light intensities in horizontal section.(65)

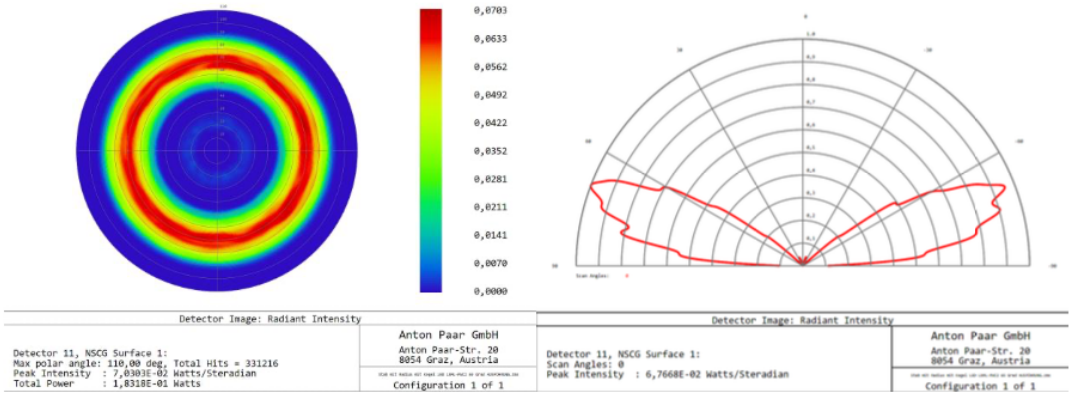

Figure 2.6: Simulation of the illuminance distribution without a parabolic reflector. The images provide information about the radial characteristic of the illumination arrangement of the quartz rod with a cone tip.(65)

Table 2.1: Results from literature research about the commonly used objective set-up for CaBER analysis.

High-Speed Camera	Telecentric Objective	Resolution	Contrast Light	Reference
Photron Fastcam-X 1024 PCI	MaxxVision TC4M 16 (magn.: × 1.00)	1.024×1.024 px (1 px ≈ 16 μm)	telecentric blue light monochromatic	(36)
Photron Fastcam-X 1024 PCI	MaxxVision TC4M 16 (magn.: × 1.06)	1.024×1.024 px (1 px≈16.13 μm)	telecentric blue light monochromatic	(30)
Photron Fastcam-X 1024 PCI	MaxxVision TC4M 16 (magn.: × 5.00)	1.024×1.024 px (1 px ≈ 3.55 μm)	telecentric blue light monochromatic	(30)
Photron Fastcam-X 1024 PCI	MaxxVision TC4M 16 (magn.: × 5.00)	1.024×1.024 px (1 px ≈ 3.55 μm)	telecentric blue light monochromatic	(3)
Photron Fastcam-X 1024 PCI	MaxxVision TC4M 16 (magn.: × 20.0)	1.024×1.024 px (1 px ≈ 0.7 μm)	telecentric blue light monochromatic	(3)
CMOS Phantom 5	Infinity K2	no information	no information	(40)
Phantom V5.0	Nikon (magn.: × 1.7)	512 × 216 px (1 px ≈ 26.8 μm)	no information	(12)
IDT X-Vision X3	Nikon (magn.: × 20)	(1 px ≈ 0.6 μm)	halogene backlight	(31)
FASTCAM MINI UX100	OTEM Zoom 70 XL (magn.: ×1-5.5)	1.280×1.20 px (1 px≈2.44-0.62 μm)	white light connected with	(66)
Phantom V5.0	no information	1.024 × 1.024 px (1 px ≈ 10.0 μm)	no information	(67)
Kodak SR-c	LEICA Zoom seven	256 × 240 px (1 px ≈6-21 μm)	no information	(68)
Phantom Micro-310	VSZ-0745 VS Technology	767 × 576 px (1 px ≈ 20.0 μm)	no information	(69)

2.1.3.2. Evaluation of the First Model (Prototype 1)

Initial tests were performed in order to evaluate the set-up for the MCR MultiDrive rheometer. In more detail, the suitability of the parabolic reflector for the lighting of the experimental area of interest was estimated. It was tried to adjust operational conditions to ensure a high resolution and enough contrast between the filament and the background for the examination of further experiments. For this first experimental set-up, a iSD high speed camera was used for the measurement of PDMS 5000 and PEO (3%, 10^6 $g \cdot mol^{-1}$) as sample liquids. The specifications of the camera are listed in Table 2.2. PDMS 5000 could be analyzed due to the comparatively long time of reaching the break-up event of 1.68 s, although the frame rate of the camera is limited. The theoretical break-up time-scale was calculated by Equation 1.38. The analysis of PEO was much more difficult due to its faster relaxation time and exponential necking. Nevertheless, it was important to assess the performance of the parabolic reflector in combination with viscoelastic liquids in order to elucidate if the required picture quality for further experiments can be achieved.

Table 2.2: Specifications of the iDS high-speed camera for capturing of images with the first Prototype.

iDS High-Speed Camera	
Gate drive	USB 3.0
Pixel clock	474 MHz
Frame rate	86.61 fps
Exposure time	0.268 ms
Black level	4
Gamma factor	1.02
Grain source value	24

Background illumination degree

The effects of illumination on the resolution and the interpretability of the images is illustrated in Figure 2.7 and Figure 2.8. Firstly, the inhomogeneous light distribution and an intensity maximum at the middle of the parabolic reflector can be revealed in both images by the formation of darker gray cycles around the center

of the light source. These observations are in accordance with the theoretical calculations of the light distribution for the parabolic reflector (see Figure 2.5).

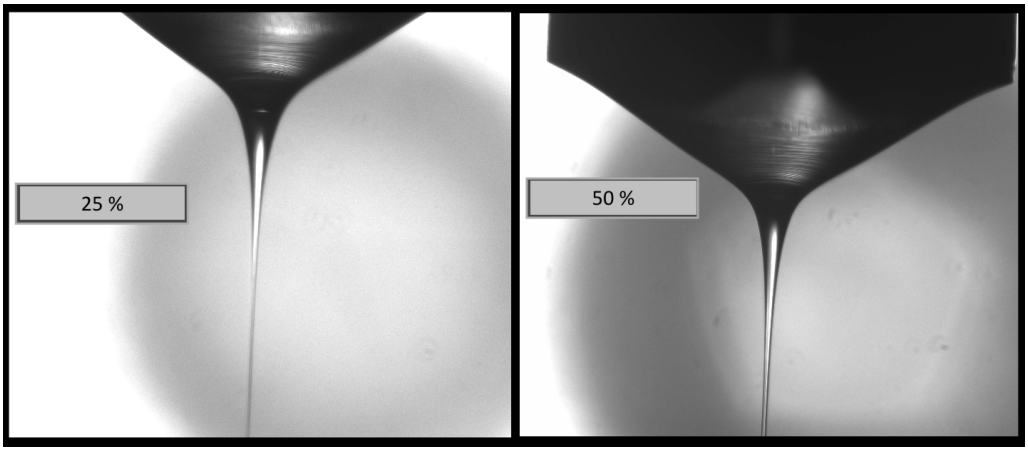

Figure 2.7: Evaluation of the light intensity impacts on the distinction of the sample from the background. The picture illustrates the sample PDMS 5000 just before the break-up event at different light intensities.

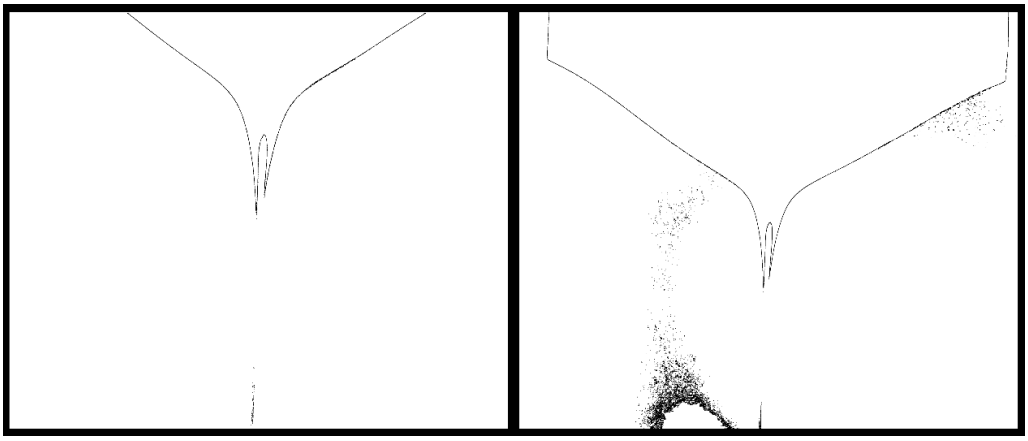

Figure 2.8: PDMS 5000: The image processing was performed by the ImageJ software. Left: Light intensity degree of 25%. Right: Light intensity degree of 50%. The grey circle at the right side results from hindered distinction of the sample thread from the background (Figure 2.6).

Furthermore, it can be seen that the reflector is not located directly behind the sample, but its position is displaced rightward. In conclusion, it was found that the exact positioning of the light source was not possible. Thus, the wavelengths of the LED could not be focused in a parallel way. The images gave information about the slightly cone-shaped diffusion of the light (Figure 2.4) and the requirement of additional adaptions of the reflector. The main problems of this experimental set-up were the over-exposure in the image center and the strong reflections on the filament, which led to image interpretation failures at very small diameters

(Figure 2.8). The figure shows the results after the performance of the image processing program ImageJ, in particular the failure to analyze small filament diameters. Additional problems were found at a higher light intensity of 50%, at which the distinction of the sample and background is much more difficult. Based on the increased illumination, the light shade must be adapted in order to reduce over-exposure. Due to the formation of darker areas, ImageJ is not able to separate the filament completely from the background, and this set-up is unsuitable for further experiments.

Position adjustment

As described in the previous paragraph, the initial position of the parabolic reflector was not optimum for the traceability of filament evolution. Firstly, the distance of the light source to the sample was changed. With the help of a piece of paper, the light distribution could be monitored all over the experimental area.

The best results were obtained nearby the sample, while at positions farther apart, huge light intensity in the middle of the two endplates can be observed. The results can be seen in Figure 2.9. The influence of the position was simulated with the help of a piece of paper (Figure 2.10). The problem of the instability of the parabolic reflector can be solved by the use of a fixing nut.

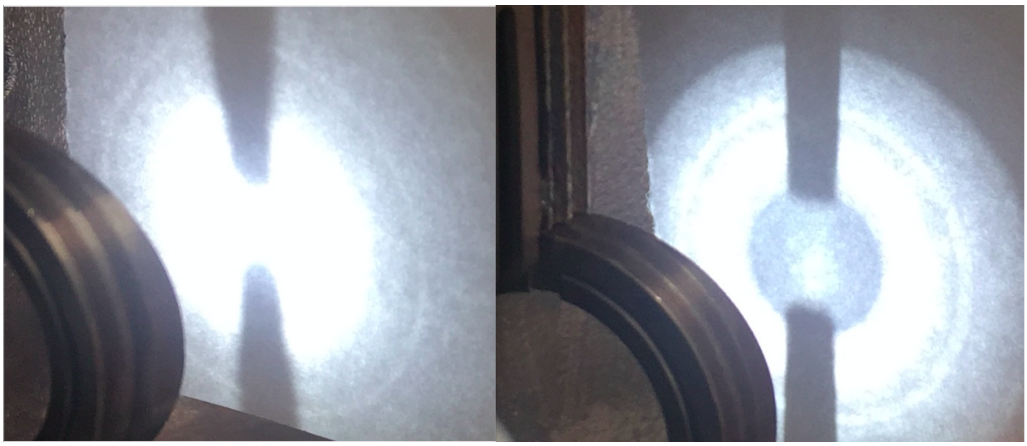

Figure 2.9: Illustration of the light distribution around the experimental area. For the visualization of the light distribution, a piece of paper was used. Left: Light distribution in long distance from the reflector position. Right: Reflector positioned very close to the measuring system. At the centre, the light intensity maximum is visible.

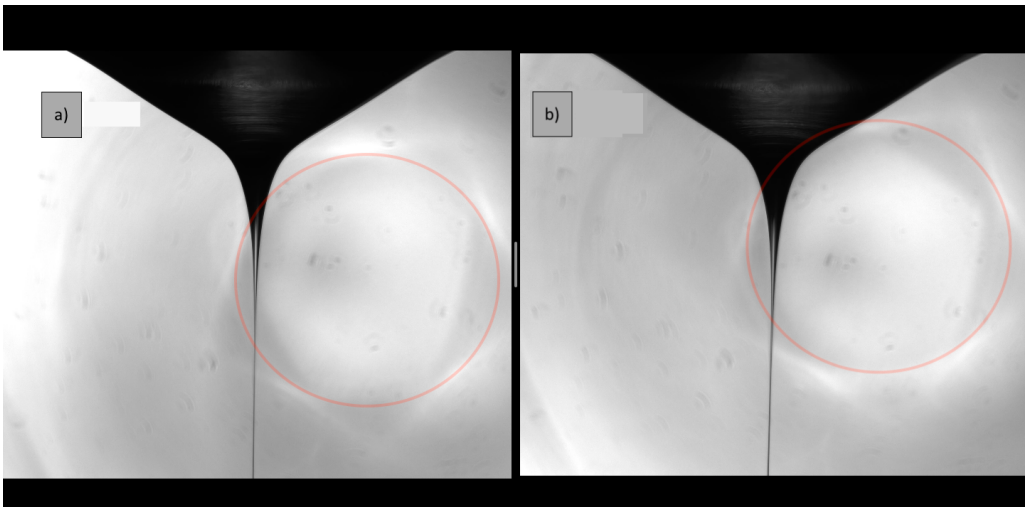

Figure 2.10: Comparison of the immobilized and normal set-up of the parabolic reflector. The picture was used for the evaluation of the influence of the light source position. The position of the light source centre is marked in red circles. a) Normal set-up. b) Immobilization of the parabolic reflector with a piece of paper.

2.1.3.3. Second Approach: Prototype 2

From the initial tests, it could concluded that the performance of the parabolic reflector was not sufficient for the illustration of the sample diameter over the whole experimental time. Despite the improvements of the position and the adjustment of the illumination degree, the limited experimental area had thwarted the optimal alignment of the light source. Based on these results, a new light source was designed with a collimator lens instead of the quartz rod and the parabolic reflector. The collimator homogeneously illuminates the sample due to the formation of a parallel beam bunch (Figure 2.11 and Figure 2.12). Simulation of the illumination with Bitmap image analysis showed that the center of the sample liquid was always brighter than the rest of the liquid. The intensity of the light-shade reflexes depends on the refraction index of the liquid and cannot be avoided completely. Therefore, it must be ensured that the outside edges of the filament can be well separated from the background in order to monitor the filament evolution. The more homogeneous illumination leads to a decreased influence of the illumination degree. The capillary velocity (v_{cap}) of PDMS 5000 as well as the relaxation time of PEO (3 wt%, 10^6 $g \cdot mol^{-1}$) could be detected over the experimental time and with all illumination degrees tested (25 - 100%).

It is known from literature (3), that the smallest diameter of PEO (3 wt%, 10^6 $g \cdot mol^{-1}$) before the break-up event is defined as $d/d_0 = 5 \cdot 10^{-3}$ [mm/mm]. With the illumination of the parabolic reflector, neither the filament diameter nor the formation of the beads-on-a string could be detected. Figure 2.13 shows the results generated with the collimator lens at different illumination degrees.

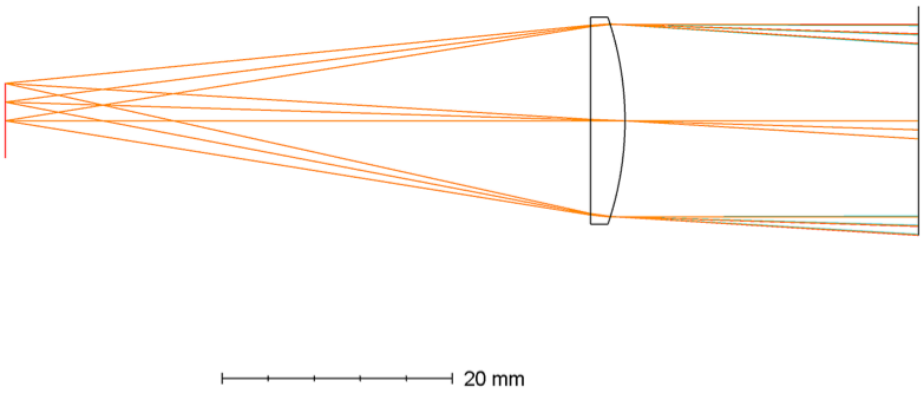

Figure 2.11: Light beam dispersion by a collimator lens.(70)

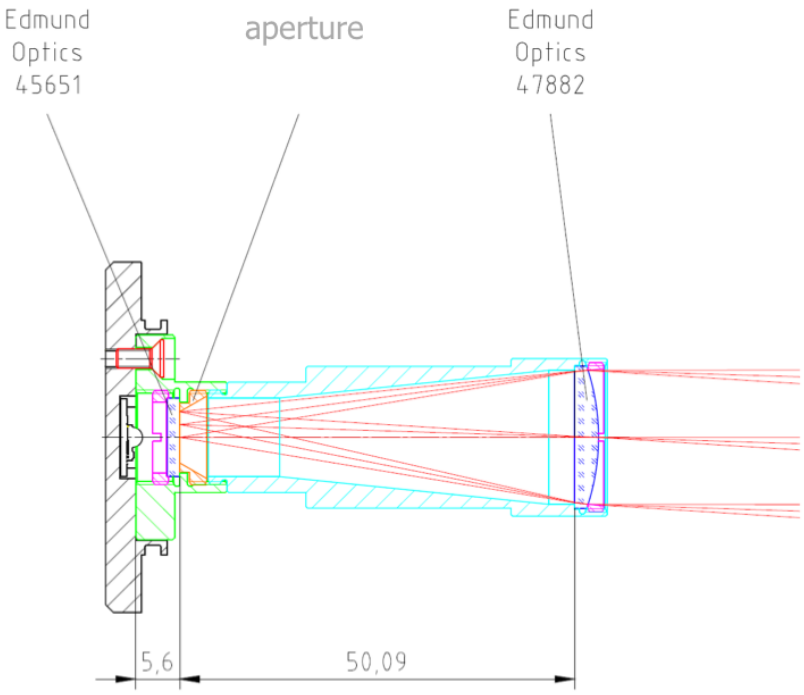

Figure 2.12: Engineering drawing of the Prototype 2.(70)

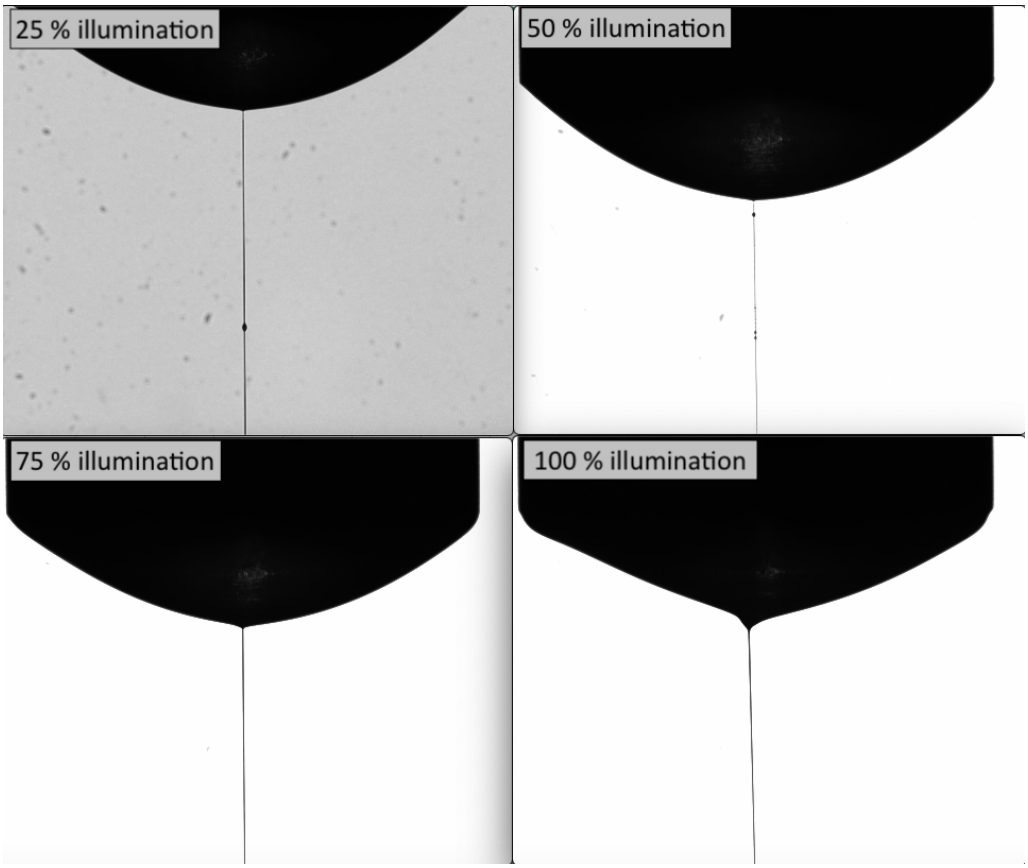

Figure 2.13: Beads-on-a-string formation of PEO (3 wt%, 10^6 $g \cdot mol^{-1}$) during CaBER measurements in the CTD 600 chamber; illumination with a collimator lens and illumination degrees from 25 to 100%. The differences in the filament evolution could be explained by composition changes of the sample during the repetition of the CaBER experiment for several times.

2.1.4. High-Speed Camera

The filament evolution of the sample liquids was determined using a HXC20 high-speed camera from the manufacturer Baumer GmbH (Germany, Friedberg). The manual of the camera foresees that the maximum housing operation temperature should not exceed 65 °C. Therefore, a heat exchanger from Anton Paar was mounted on the top of the camera. Due to this additional assembling, the temperature of the camera could be reduced to 52 °C (Figure 2.14). The working computer has access to the camera by an installed frame grabber. Additionally, controlling of the camera is necessary due to the non-constant frame rate. The frame rate is dependent on the buffer-store load and, consequently, is not always the same. The resulting fluctuations impede equidistant temporal measurements.

This issue could be solved by using a frequency generator with a constant square wave and a fixed frequency. The specifiactions of the camera and frequency generator are given in Table 2.3.

Table 2.3: Specifications of the HXC20 high-speed camera and the frequency generator. Additional information can be found in the Appendix.

Baumer HXC20 High-Speed Camera	
Gate drive	Frame grabber
Trigger	Frequency generator (Agilent; 33500B series Waveform Generator)
Frequency signal	Square wave
Frequency	Sample-dependent
Amplitude	10.00 Vpp
Offset	5.0 V
Duty Cycle	50%
Start Phase	0.0 °
Silicon Software	
Display	2048(weidth) x 1088(height)
Output Format	8 bit
Trigger/Exsync	Mode: External Trigger
Flash	OFF
Number of Framebuffer	2700
Acquisition timeout	1000 s
CL ConfigTool	**(Version: 64 bit)**
Device clock	SENSOR 48
Exposure	Mode: TIMED; Time: 4
Frames Per Seconds	22222.22
Gain	1
Image Format	Full Frame (2048x1088)
Interface Taps	10
Partial Scan	Sample-dependent
Pixel Format	Mono8
ReadoutMode	OVERLAPPED
Sensor Digitization Taps	SIXTEEN
Timer control	TIMER1 (Duration: 10 ms)
Trigger	HARDWARE1

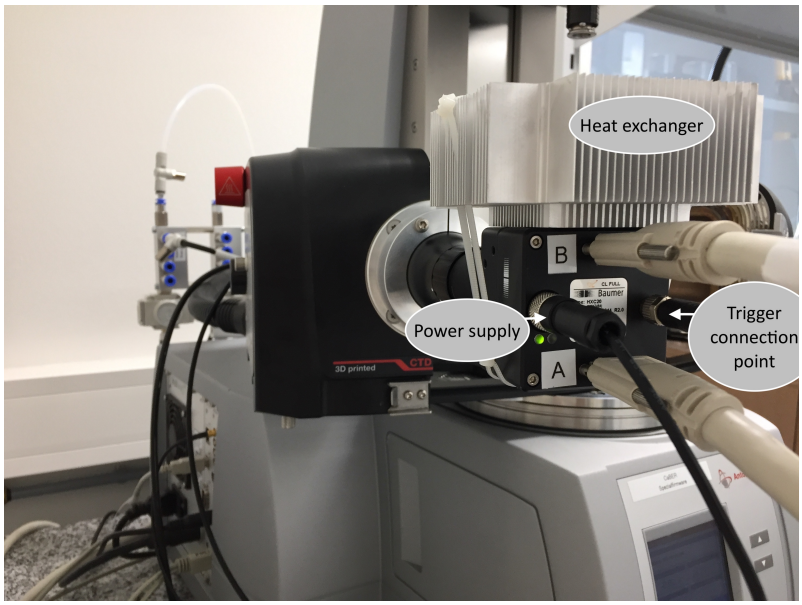

Figure 2.14: Set-up of the high-speed camera with a heat exchanger mounted on top of the camera and marked connection points for the power supply and the trigger cable.

2.2. Test Procedure

The test procedure is emblematically pictured in the eight-step flow diagram hereinafter (Figure 2.15). Every blue rectangle represents a new operating step. The green rectangles at the right side deliver a short description. Furthermore, the major steps are described in detail hereinafter.

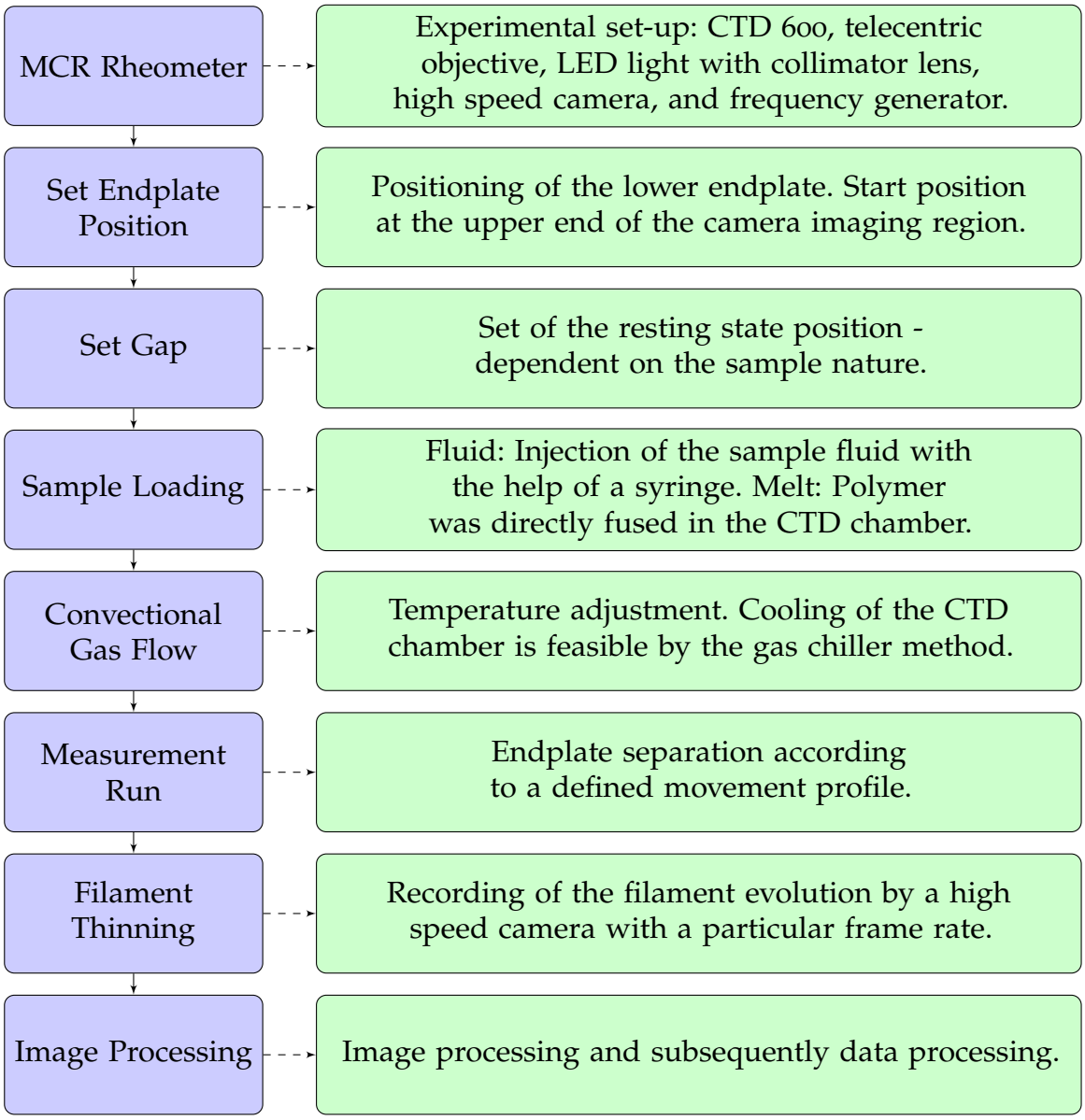

Figure 2.15: Test procedure.

2.2.1. Initial Endplate Separation: Resting State

The most important parameter to keep the cylindrically shaped fluid sample between the two endplates is the surface tension. Hence, the initial endplate separation must be set small enough to support a static liquid bridge. In the case of additional axial gravity, the sample size depends on the fluid volume and the Bond number (Equation 2.1). (*12*) To ensure successful sample loading, the capillary length l_{cap} (Equation 2.2) was calculated for all liquid samples. If l_{cap} is greater than or equal to the initial endplate separation h_0, an initial cylindrical shape of the sample can be ensured. If Equation 2.3 or Equation 2.4 is fulfilled, the sample is stable against gravitational sagging. The calculated values of all samples are given in Table 2.4.

$$B_0 = \frac{\rho g R_0^2}{\sigma} \tag{2.1}$$

$$l_{cap} = \sqrt{\frac{\sigma}{\rho g}} \tag{2.2}$$

$$\frac{h_0}{l_{cap}} \geq 1 \tag{2.3}$$

$$\frac{h_0}{R_0} \leq \frac{1}{\sqrt{B_0}} \tag{2.4}$$

Table 2.4: Optimal sample volume and initial endplate separation for each sample.

Sample	ρ *[kg/m^3]*	σ *[N/m]*	l_{cap} *[mm]*	h_0 *[mm]*
PDMS 5000	974.4	0.00205	1.4868	1.5
PDMS 100	966.0	0.0202	1.4599	1.5
PDMS 5	911.2	0.0186	1.422	1.5
PEO[1]	993.0	0.0628	2.539	3.0

[1] 3wt% 10^6 $g \cdot mol^{-1}$

2.2.2. Sample Loading

During initial plate separation h_0, the apparatus was completely loaded with the sample. It is of high importance that the gap is not crowed or insufficiently filled, and that there are no air bubbles in the fluid bridge. All these factors could cause problems during the experiment. Thus, the sample loading needs to be done accurately to avoid these problems and to obtain reproducible results. The loading of the liquid samples was performed with a syringe. The over-flow of the sample was wiped away with a piece of paper. The loading of the polymer melts between the two endplates was more complex: The solid polymeric sample was directly fused in between the endplates. By subsequent removal of the over-loaded sample, it was tried to load samples with the same mass and volume. An explanation of the procedure and a calculation of the error rate is given in subsection 2.3.4.

2.2.3. Convection Gas Flow

The temperature adjustment was performed by the heating device (CTD chamber) in combination with continuous convectional gas flow. In order to achieve temperatures lower than room temperature, a gas chiller device was mounted. The function of the gas chiller was to pre-cool the injected gas by an external cold water flow. The flow diagram (Figure 2.16) illustrates the main flow directions. The rectangle represents the gas chiller device with an incoming and outgoing continuous gas flow ($\dot{m}_2$); the mass flow $\dot{m}_1$ represents the cold water stream. The principle of this device is based on a heat exchanger and results in a cooling of the injection gas. Insulation of the gas cable ensured the temperature maintenance during the path in the CTD chamber. Mass flow $\dot{m}_2$ reaches the CTD chamber with a temperature of approximately 15 °C. By heating of the CTD chamber, temperature adjustment of 20 °C could be achieved.

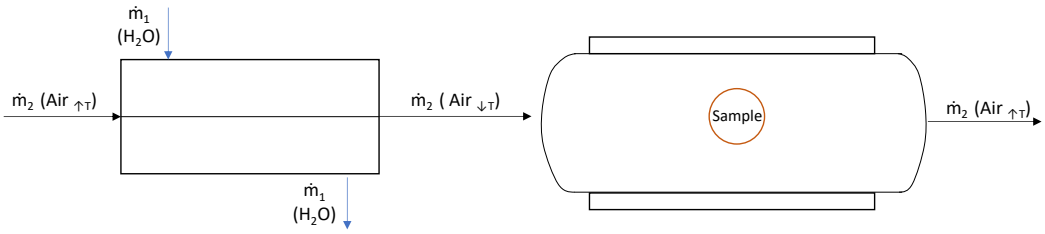

Figure 2.16: Flow diagram of the CTD 600 chamber in combination with an air cooling system. The gas chiller is illustrated at the left side as rectangle. The CTD chamber is pictured as cylinder (right) with the included sample marked in a red circle. The water and gas flow are represented as $\dot{m}_1$ and $\dot{m}_2$ mass steam ($\dot{m}_2$= 30 L/min).

2.2.4. Endplate Separation Profile

In dependence on the required conditions, different movement profiles can be set. In general, the Rheocompass software is not constructed for CaBER measurements and, thus, the adjustments of the movement profiles is one of the biggest limitations of the system. The acceleration and the position of the electromagnetic brake impulse must be set by an experimental trial-and-error method. In this study, three endplate separation profiles were designed, namely non-damped step displacement, semi-damped step displacement, and damped step displacement. A comparison of the measured maximal separation velocities and times for the separation process are given in Table 2.5.

Non-Damped Step Displacement

In the non-damped step displacement, the lower endplate reaches the final position as fast as possible without additional electromagnetic brake impulses that affect the linear drive movement. That means that the measuring body collapses with the linear drive housing and induces mechanical vibrations. The arising vibrations cause oscillations of the filament thread and hinder the evaluation of the filament evolution in the first micro-seconds. The plotted diagram (Figure 2.17) shows the velocity of the lower endplate, the underling endplate displacement, and electrical force as a function of time. The electric force F_{el} during the experiment is illustrated on the secondary axis as green line. The lower endplate reaches its final position after 40 ms, and the subsequent stabilization of the mechanical

vibrations takes 20 ms (Figure 2.17). The occurring vibrations got transferred to the filament thread, caused destabilization, and the diameter evaluation was impeded. Notably, the consumed stabilization time was too long for an accurate evaluation of low-viscosity samples.

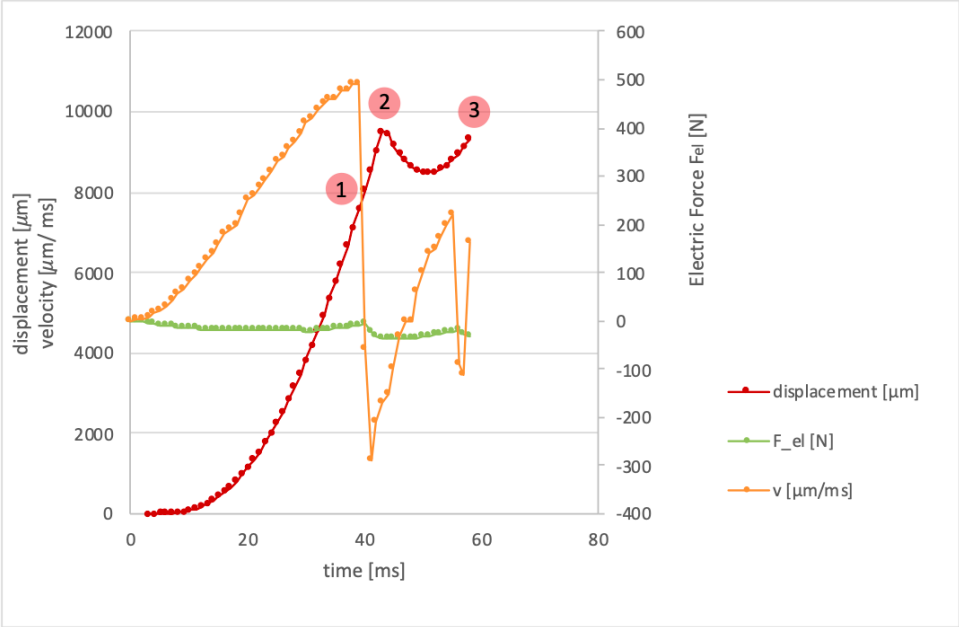

Figure 2.17: Non-damped step displacement of the lower endplate. The velocity of the lower endplate is indicated as yellow line. The electrical force is plotted on the secondary axis as green line. Number 1 represents the position of the maximum velocity v_{max}. Number 2 and 3 represent $t_{collision}$ and $t_{resting}$.

Semi-Damped Step Displacement

A better movement profile for the analysis of a low-viscosity sample is the slightly damped step displacement, in which the measuring system is damped after a specific period of time. Thereby, the impact of mechanical vibration on the filament thread can be reduced. The resulting displacement profile is illustrated in Figure 2.18. In general, the acceleration of the endplate is performed in two sub-steps. In the first step, the endplate is accelerated up to a maximum velocity of 0.21 m/s (1a). Then, the linear drive movement was damped by an electromagnetic brake between the time period of 21 to 37 ms. After this slow-down process, the second acceleration step is initiated. In this last section before the collision event, a maximum velocity of 0.33 m/s (1b) can be reached. In this region, the mean velocity is around 0.189 m/s. At the collision event, the actual velocity of the linear drive motor is 0.117 m/s (2). The impact of the mechanical vibrations

is represented by oscillations at the time interval between t = 51 - 57 ms. After the final endplate stabilization, it is held for 10 s at its final position (3). In conclusion, an accurately set electromagnetic brake impulse leads to a delayed achievement of the final position. However, one can see that the mechanical vibrations can be decreased significantly. Also, the consumed time to achieve a stabile resting position after the collision event is much shorter than for the non-damped profile.

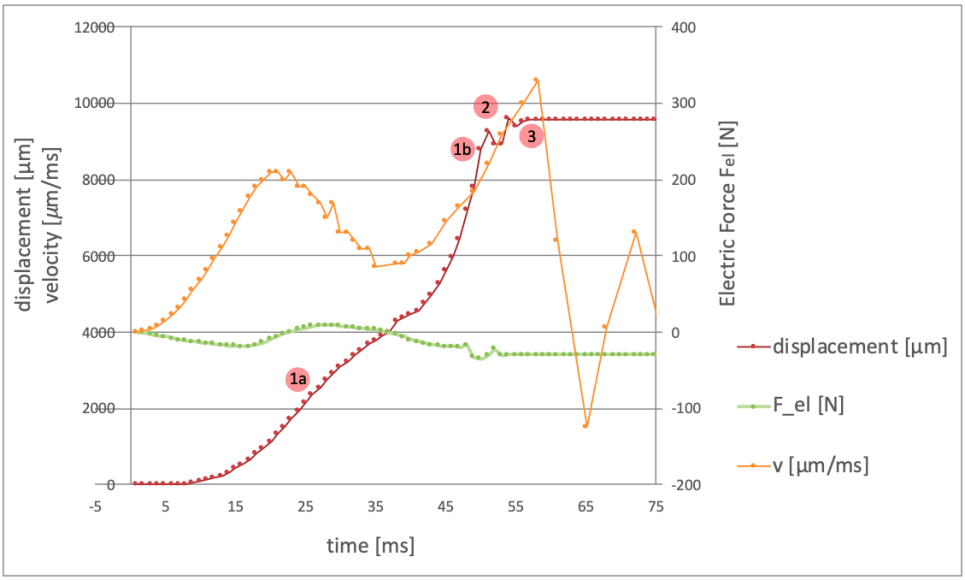

Figure 2.18: Endplate separation profile during a semi-damped endplate separation. The velocity of the lower endplate is indicated as yellow line. The electrical force is plotted on the secondary axis as green line. Number 1a represents the position of the maximum velocity in the first acceleration section. Number 1b is the overall maximal velocity v_{max}. Number 2 and 3 represent $t_{collision}$ and $t_{resting}$.

The evaluation of the influence of the remaining vibrations was examined by the medium-range viscosity sample PEO and the low-viscosity sample PDMS 100 (Figure 2.19). The diagram shows the ability of balancing the initial vibrations as a function of time. Both samples show a completely different impact of the remaining oscillations. While PEO shows strong variations in the first microseconds, PDMS 100 only gets slightly (but longer) affected. However, the medium-range viscosity sample is able to re-stabilize the occurring interferences after a short period of time. The region of measurable oscillation ranges over a time period of 0.011 ms, in contrast to the low-viscosity sample, in which small oscillations are noticeable over the whole filament thinning experiment.

In the end, the transferred vibrations caused a premature filament break. This evaluation shows that the semi-damped separation profile is not suitable for the observation of the filament thinning of low-viscosity samples.

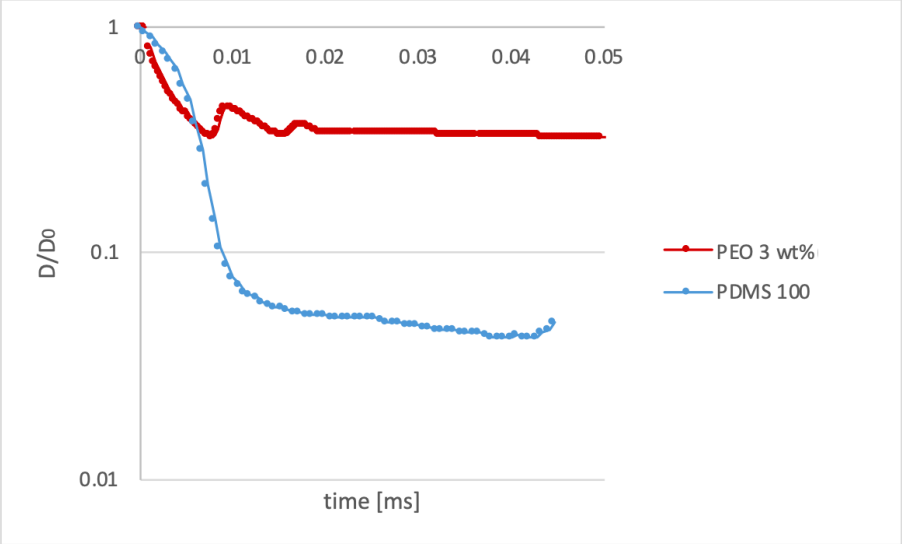

Figure 2.19: Filament diameter evolution as a function of time. The diagrams illustrate the filament evolution in the first milliseconds with predominant oscillations caused by the collision event. Red: Initial oscillations of PEO (medium-viscosity sample). Blue: Overall thinning with predominant oscillations of PDMS 100 (low-viscosity sample).

In addition to the evaluation of the collision event of the semi-damped movement profile, also the influence of the sample nature was examined. Figure 2.20 illustrates the endplate separation during the CaBER measurement of a high-viscosity sample (PDMS 1,000,000) and a low-viscosity sample (PDMS 5). The resulting movement profile was used to investigate the influence of the sample viscosity and to detect the maximum time to reach the endplate position. The result of this investigation is that the endplate movement is independent of the sample as both curves are completely congruent.

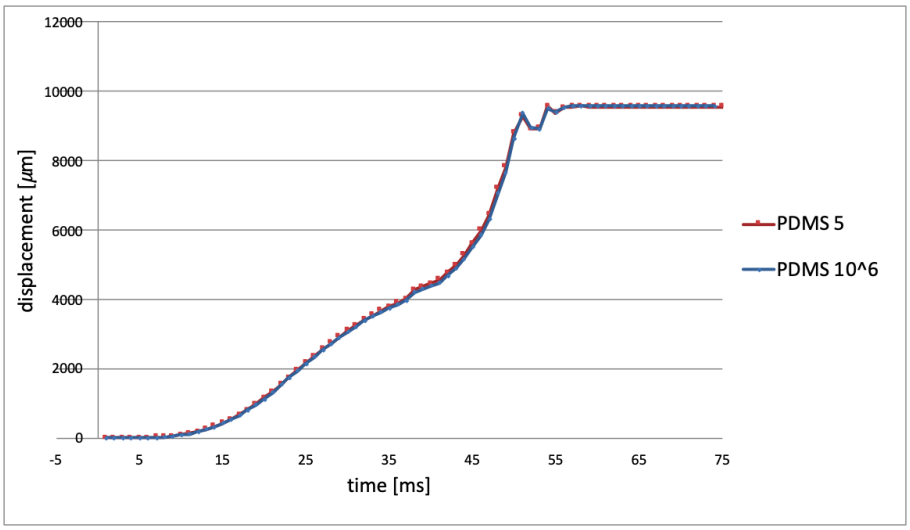

Figure 2.20: Viscosity influence on the endplate separation profile. Comparison of a high- (PDMS 1,000,000) and low-viscosity (PDMS 5) sample with the aim to estimate the influence of the sample nature on the endplate separation profile.

Damped Step Displacement

Based on the previously made investigations, a damped endplate separation profile was designed, in which no mechanical vibrations should be noticeable. In comparison to Figure 2.18, the slow-down process was set earlier and softer, such that the change from the maximal acceleration (-50) to maximal deceleration (50) was set in a value ramp. These adjustments yield a velocity evolution similar to a Gaussian curve. Hence, a slow approach of the endplate to the final position can be accomplished.

Figure 2.21 illustrates the endplate separation of the damped step displacement mode. The endplate reaches its end position after a time period of $t_{resting}$= 60 ms (3). The maximal velocity of v = 0.34 m/s is reached after t = 30 ms (1).

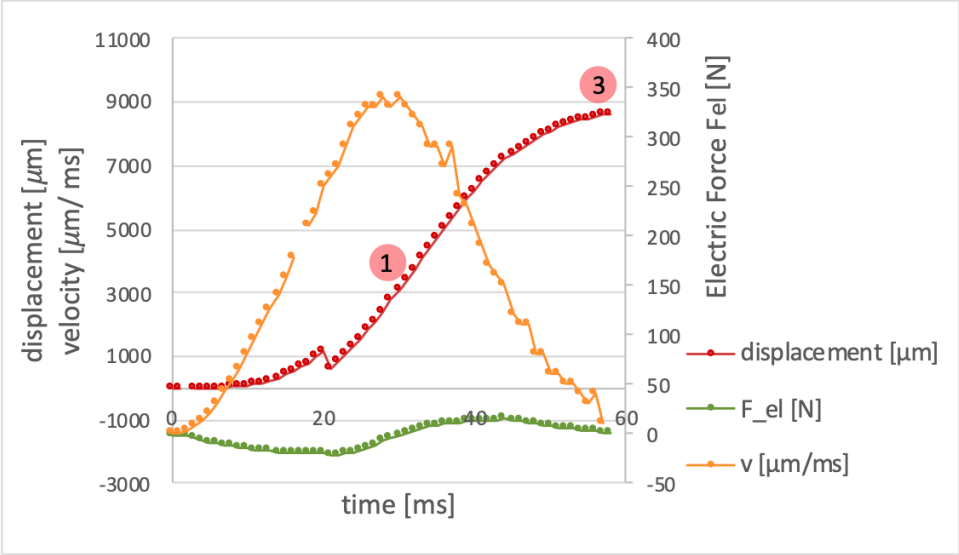

Figure 2.21: Endplate separation profile during a damped step displacement of the lower endplate. Number 1 represents the position of the maximum velocity v_{max}. Number 2 illustrates the time until the resting state position of the endplate is achieved, $t_{resting}$.

Summary

The result of the studies of the three endplate displacement profiles show that the damped step separation was the best option for CaBER measurements. Due to the fact that the CaBER operability range should include samples with a low viscosity (70 mPa·s), initial mechanical vibrations need to be avoided. As proved before, transferred oscillations from the collision event are able to cause premature filament break. Also, additional interferences during filament thinning were observed.

The damped endplate separation profile shows none of these interferences. Despite the brake event, the endplate reaches its final resting position nearly as fast as in the non-damped profile (Table 2.5). Thus, it is evident that the damped endplate displacement is also suitable for low-viscosity samples with short filament lifetimes. Accordingly, the damped step displacement was used for all CaBER experiment in this study.

Table 2.5: Summary of the most important data of the three endplate separation profiles. The list contains the maximum observed velocity v_{max}, the time period that was consumed until the collision event ($t_{collision}$), and the time at which the endplate remains stable at its final position ($t_{resting}$).

Movement Profile	v_{max} *[m/s]*	$t_{collision}$ *[ms]*	$t_{resting}$ *[ms]*
Non-Damped	0.49	44	59
Semi-Damped	0.33	51	57
Damped	0.34	-	60

2.2.5. Image Processing

The recorded experimental region is exemplarily documented in Figure 2.22 as red rectangle. Due to optical limitations, it is impossible to record the whole experimental region. The evaluation of the filament diameter evolution was accomplished by the image progressing program ImageJ. The image sequence was imported as an image stack, to which image processing was adopted simultaneously for all pictures of the sequence. The motivation behind the evaluation method was the conversion of the 8-bit pictures into pictures in which only the edges of the filament were pictured as black pixels. The ”Fill Hole” step is able to correct errors originating from dust on the camera lens. Thus, no interferences of background noise were observed. The measuring body with its defined diameter of 4.0 mm was used as reference value. According to this scale, the measuring unit was converted to 357 pixels/mm. As final step, at a defined position, an observation line was set (Figure 2.22: red line). The observed line was marked at the same height for all image stacks, independent of their frame rate or partial scan. The pixels on this line were exported as value list (0 = white and 255 = black) and were transferred in an Excel sheet. In Excel, the distance between the black pixels on every image of the image sequence was calculated. Based on this calculation, the filament evolution could be followed, and further calculations of the relaxation time and capillary velocity were enabled.

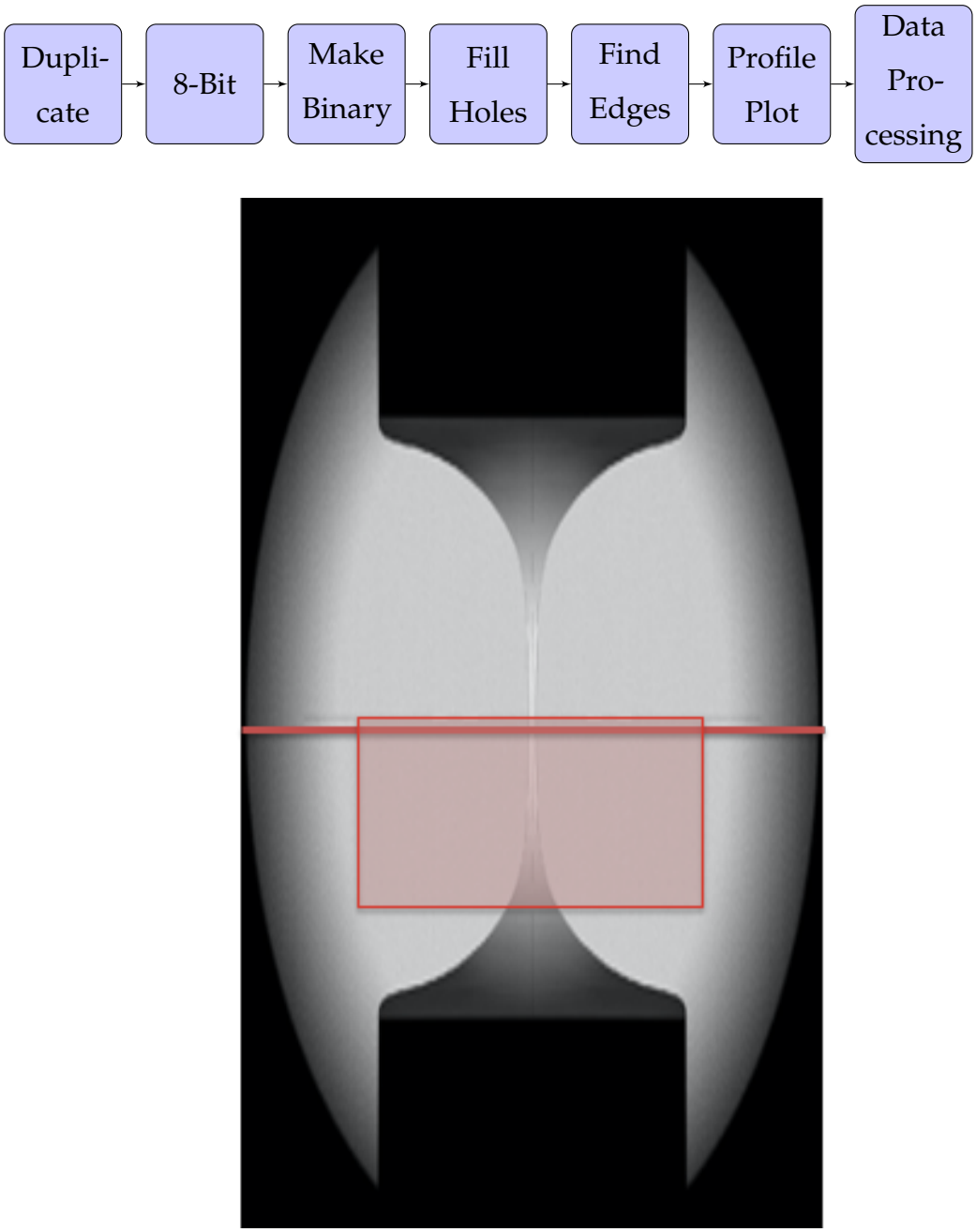

Figure 2.22: Top: Strategy for picture evaluation Bottom: Exemplary illustration of the recorded image region (red rectangle) during the elongation experiment inside the CTD chamber. All pictures were evaluated at the same level (red line): upper distance y = 0.06 mm; angle = 0 °

2.3. Samples

This section provides a short overview of the samples used in these studies. Furthermore, the preparation of the 3 wt% poly(ethylene oxide) solution is detailed. It is highly important to choose the correct preparation path in order to yield reproducible results. PEO is hygroscopic and changes its concentration upon wrong storage or experimental conditions. The elastic amount of the PEO samples was determined by shear rheology. Moreover, gel permeation chromatography GPC was performed to quantify the molecular weight distribution and the dispersity index of the Newtonian liquids. The shear viscosity of PDMS 5000 was analyzed at different temperatures to evaluate the temperature limits for the subsequent CaBER measurements.

2.3.1. Poly(dimethyl siloxane) (PDMS)

Poly(dimethyl siloxane) is an inorganic polymer composed of a Si-O-Si backbone with attached organic methyl groups. The repetition unit is illustrated in Figure 2.23.(*71*)

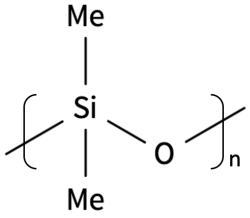

Figure 2.23: Repetition unit of poly(dimethyl siloxane).

From literature, it is known that PDMS is widely used as standard Newtonian fluid for rheological measurements.(*8*)(*13*)(*72*) Hence, the determination of the Newtonian fluid behavior in the newly developed extensional rheometer was performed by silicon oils based on the study of Clasen *et al.* in 2011 (*13*).

The PDMS samples with a viscosity of 5 mPa·s and 5,000 mPa·s were supplied by Bluestar Silicones. The other PDMS sample was obtained from AMETEK Brookfield. The silicon oil is specified as standard viscosity sample with a viscosity of

100 mPa·s with an accuracy of ± 1%. Due to the fact that the rheological behavior is influenced by the molecular weight and the molecular weight distribution, GPC analyses were performed. The chain length of PDMS 5 was too small, for a successful quantification by GPC. Hence, the molecular weight range of 9000 to 1,100 $g \cdot mol^{-1}$ (Rodorsil Oils 47V 5), given by the data sheet and measured by exclusion diffusion chromatography EDC, was considered. The GPC results are summarized in Table 2.6 and Figure 2.24.

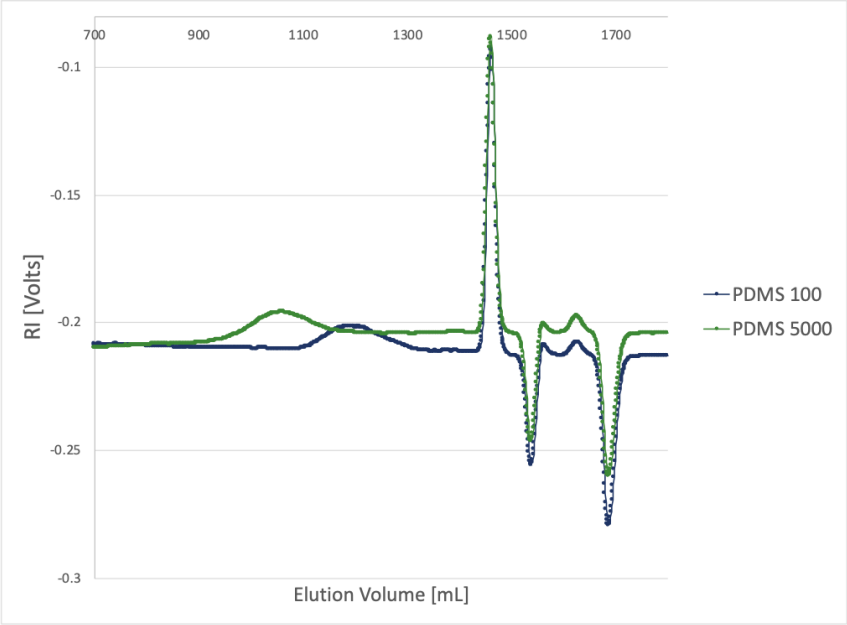

Figure 2.24: Gel permeation chromatography of PDMS 100 (blue curve) and PDMS 5000 (green curve).

Table 2.6: List of the molecular weight and the molecular weight distribution of PDMS 100 and PDMS 5000.

Sample	M_n $[g \cdot mol^{-1}]$	M_w $[g \cdot mol^{-1}]$	M_w/M_n
PDMS 100	$8.0 \cdot 10^3$	$1.12 \cdot 10^4$	1.41
PDMS 5000	$3.36 \cdot 10^4$	$6.08 \cdot 10^4$	1.81

2.3.2. Poly(ethylene oxide) (PEO)

Poly(ethylene oxide) is a water-soluble thermoplastic resin with a general repetition unit $CH_2 - CH_2 - O$ (Figure 2.25). The non-ionic polymer is widely used in the cosmetic and pharmaceutic industry for humidification or as carrier agent. (73)

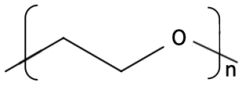

Figure 2.25: Repetition unit of poly(ethylene oxide).

The PEO powder was supplied by Sigma-Aldrich. Due to the fact that the relaxation time can only be described for viscoelastic fluids up to their entanglement concentration, the sample preparation was performed according to the study of Arnolds *et al.* (*3*). They describe that PEO ($M_w = 10^6$) concentrations above 3% of do not show a distinct period of exponential thinning. According to these findings, a concentration of 3% was chosen to determine the rheological behavior of viscoelastic polymeric solutions. The molecular weight of the sample was evaluated by GPC measurements with dichloromethane as eluent. The values for M_n and M_w can be found in Table 2.7.

Table 2.7: Molecular weight and the molecular weight distribution of PEO.

Sample	M_n $[g \cdot mol^{-1}]$	M_w $[g \cdot mol^{-1}]$	M_w/M_n
PEO	$2.42 \cdot 10^6$	$3.38 \cdot 10^6$	1.40

Sample Preparation (3 wt% Solution)
In a 100 mL beaker, 0.3744 g of PEO and 12.584 g distilled water were added. After the addition of a magnetic stirring bar, the beaker was closed air-tight with Parafilm. The 2.98 wt% solution was stirred for 17 h at room temperature.

2.3.3. Poly(isobutylene) (PIB)

Poly(isobutylene) is a copolymer composed of isobutylene and small percentages of isoprene. The basic repetition unit is illustrated in Figure 2.26. The elastomeric polymer is widely used in industry because PIB exhibit many favorable properties like the impermeability to water and gases, high chemical stability, and high elasticity. (*74*)

The sample preparation was performed according to the SRM 2490 NIST special publication. SRM 2490 is a Standard Reference Material (SRM) introduced

in 2001 by the National Institute of Standards and Technology (NIST) as a non-Newtonian reference fluid which consists of poly(isobutylene) dissolved in 2,6,10,14 tetramethylpentadecane. (*75*) The SRM was selected because it exhibits similar characteristic viscoelastic behavior like polymer melts, with the advantage of being liquid a room temperature.(*13*) Thus, the characterization of the SRM enables a further interpretation of the CaBER data obtained of the polymer melts.

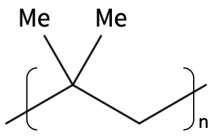

Figure 2.26: Repetition unit of poly(isobutylene).

2.3.4. Polystyrene (PS)

Polystyrene (Figure 2.27) is an amorphous, non-polar thermoplast that shows viscoelastic behavior.

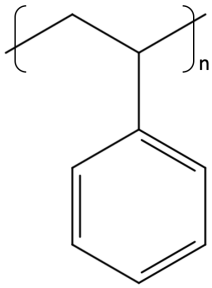

Figure 2.27: Repetition unit of polystyrene.

The viscous and elastic amount of the sample is influenced by the molecular weight and molecular weight distribution.(*76*) Based on this theory, three different molecular weight samples were prepared for the CaBER experiment. The 1,200 $g \cdot mol^{-1}$, 45,000 $g \cdot mol^{-1}$, and 260,000 $g \cdot mol^{-1}$ molecular weight PS pellets were supplied by Scientific Polymer Products. Based on the behavior and appearance of the solid structure and the density values (see Table 2.8), it can be assumed that all PS samples are present in amorphous form. In general, isotactic and syndiotactic

polymerization methods of PS have been reported, yielding polymers with a varying ratio of crystallinity.(77)

Sample Preparation

In order to improve the reproducibility and to optimize the measurement itself, plates were pressed from the pellets, from which test specimens were cut out. Due to the extremely brittle material behavior, however, no satisfactory sample quality could be achieved. For this reason, the measurements were performed directly on the pellets. The PS sample was fixed between the parallel plates, and the temperatures were set according to Table 2.8. As the sample began to soften, a gap of 1.0 mm was set, and the overlapping sample was removed with the help of a spatula and tweezers. After this treatment, the gap was reduced to its final position of 0.8 mm. A verification of the reproducibility of the sample preparation method was performed by triple determinations of the specimens (diameter of 4.0 and thickness of 0.8 mm) with a precision balance. The determination of the mass of the sample yielded an average mass of 9.35 mg. The variance between the analyzed samples was 0.093 $(mg)^2$, which corresponds to a deviation of 0.305 mg ($\sim$ 3.26%) for this type of sample preparation.

Due to the fact that the error rate is about 3%, the preparation method has been identified as a simple alternative for the loading of brittle specimens.

Table 2.8: List of the PS masses after the sample preparation.

M_w $[g \cdot mol^{-1}]$	*CaBER-Temperature* $[^\circ C]$	*density* ρ $[g/cm^3]$	*Solid Consistency*
1,200	100	1.06	BEADS (brittle, glassy)
45,000	200	1.05	GRANULAR (brittle, haze)
260,000	250	1.05	PELLETS (stiff, haze)

3. Results and Discussion

3.1. Shear Rheology

3.1.1. Poly(dimethyl siloxane) 5000 (η= 5.0 Pa·s)

The silicon oil sample with η= 5.0 Pa·s was analyzed by rotational shear rheology at different temperatures. The viscosity curves obtained are shown in an overview diagram in Figure 3.1. The measurement was performed to identify the correlation of viscosity and temperature and to obtain information for the subsequent CaBER measurements, performed at the same temperatures. The zero shear viscosity was used to evaluate the suitability of the sample for CaBER measurements. In addition, the capillary velocity and the break-up time could be calculated from the obtained viscosity values.

In general, the viscosity is a temperature-dependent parameter and decreases as the temperature increases. This was also verified in the measurements made in this study (Figure 3.1). The zero shear viscosity decreases significantly with increasing temperature. Thus, the highest viscosity value was obtained at a temperature of 20 °C, and the lowest viscosity value at 100 °C. Furthermore, it was noticed that small temperature fluctuations of 5 K can induce large viscosity shifts. The difference of the viscosity obtained at 20 °C and 25 °C is 0.28 Pa·s and demonstrates the necessity of precise temperature adjustment for rheological measurements. The viscosity levels and the standard deviation (triple measurements) are given in Table 3.1. The viscosity of PDMS 5000 at 100 °C drops to only 1.66 Pa·s compared to 5.48 Pa·s at 20 °C, which corresponds to a viscosity decrease of about 70%.

An additional influencing factor on the shear results is the sample loading. The amount of sample and the trimming process have large influence on the shear viscosity. The curves shown in Figure 3.2 clearly show the influence of sample preparation; it was found that the measurement error for the sample loading is very high. The mean zero shear viscosity is 5.478 Pa·s, and the standard deviation

between the first two curves (blue and orange) and the third measurement (green curve) is 97.38 mPa·s.

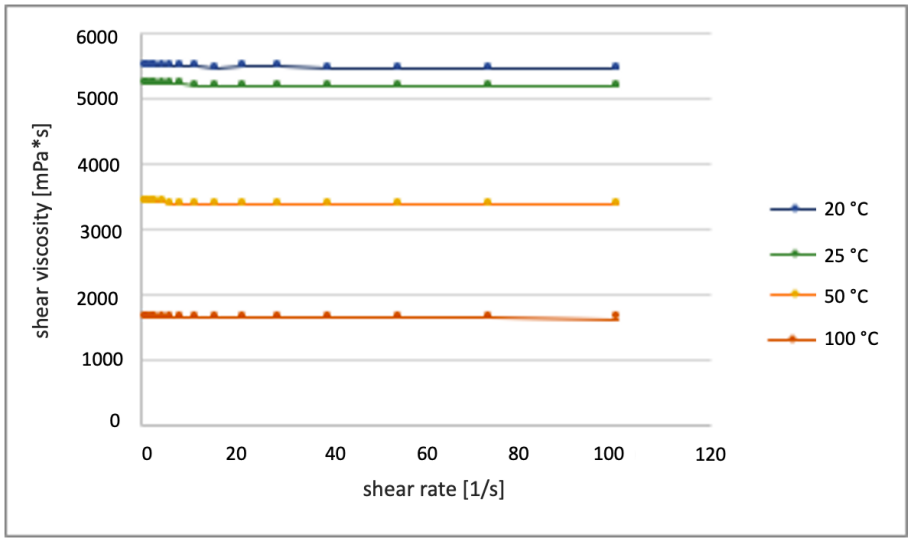

Figure 3.1: Summary of the rotational shear analyses of PDMS 5000 at different temperatures.

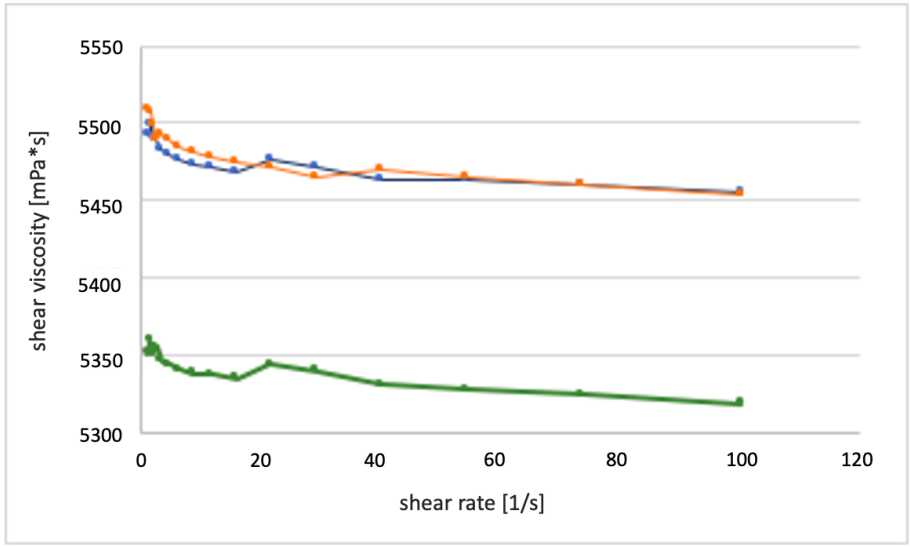

Figure 3.2: Threefold determination of the shear viscosity of PDMS 5000 at 20 °C.

Under the premise that the behavior of the sample is not changed or influenced by shear rheological analysis, it was decided that the influencing factor of sample preparation can be eliminated by loading each sample only once in order to obtain more accurate results. The standard deviation between the shear viscosity curves at a given temperature was below 0.5% for all experiments. Hence, with this measuring method, very well reproducible results can be achieved.

Table 3.1: List of zero shear viscosities of PDMS 5000 at different temperatures.

Sample	*Temperature [°C]*	*Zero shear viscosity [Pa·s]*	*Standard deviation [Pa·s]*
PDMS 5000	20	5.48	$3.43 \cdot 10^{-3}$
PDMS 5000	25	5.20	$3.12 \cdot 10^{-3}$
PDMS 5000	50	3.40	$8.96 \cdot 10^{-3}$
PDMS 5000	100	1.66	$2.96 \cdot 10^{-3}$

From the previous work of Rodd *et al.* (*12*) (see subsubsection 1.3.4.1) it is known that the CaBER set-up is limited to fluids with viscosities above 70 mPa·s. The lowest zero shear viscosity of PDMS, which was achieved at a temperature of 100 °C, has a mean value of 1.66 Pa·s and therefore fulfills the requirements for CaBER measurements. In conclusion, the shear rheology analysis of PDMS 5000 shows that the sample is suitable for CaBER analysis in a temperature range of 20 to 100 °C.

3.1.2. Poly(ethylene oxide) Solution (3 $wt\%$, $M_w = 10^6\ g \cdot mol^{-1}$)

The shear viscosity of the 3 *wt*% PEO solution was examined by recording a flow curve. The flow curve illustrates the viscosity in dependence of the shear rate $\dot{\gamma}$. The zero shear viscosity plateau was used for the calculation of the mean shear viscosity of the sample. The experiment was repeated twice; both curves are congruent with each other (Figure 3.3). A zero shear viscosity of 2.49 mPa·s was found. In comparison with the literature value of 2.61 mPa·s (*3*), the experimental result show a small deviation of 0.085 mPa·s.

Amplitude Sweep

The amplitude sweep was performed at an angular frequency of 6.28 rad/s and a temperature of 20 °C. In the diagram shown in Figure 3.4, the measured storage and loss modulus are plotted as a function of the strain γ. The loss modulus is larger than the storage modulus ($G' < G''$); thus, the sample shows viscoelastic fluid behavior. Furthermore, the boundary of the linear viscoelastic region (LVE) can be estimated from the amplitude sweep measurement. The boundary of

the LVE region is important for further frequency sweep tests. The LVE region reflects the stable linear viscosity plateau. In this example, a constant plateau was identified up to approximately 50% shear strain.

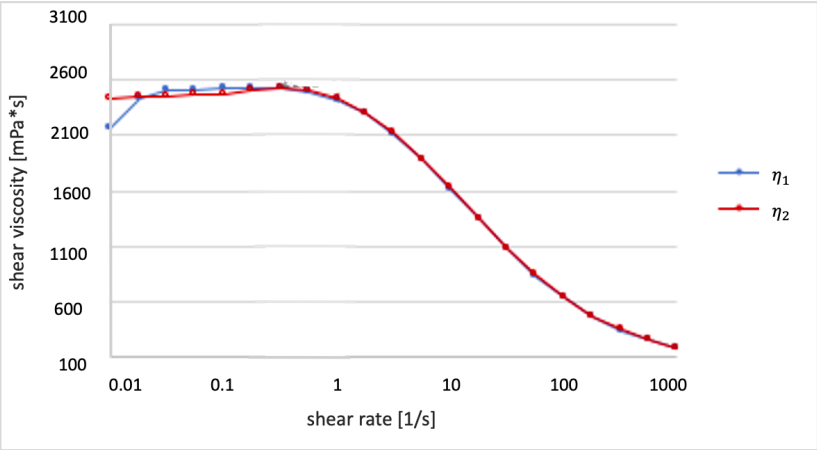

Figure 3.3: Diagram of the recorded flow curve of the 3 wt% PEO soultion.

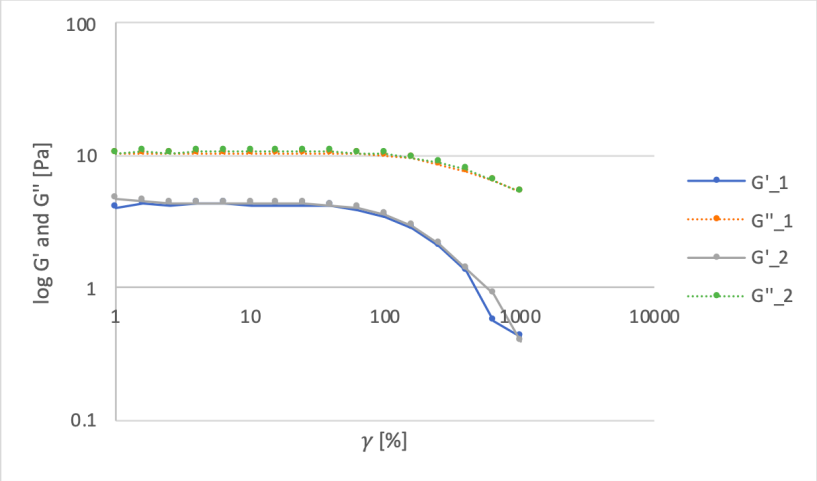

Figure 3.4: Shear analysis curves of PEO under amplitude sweep conditions.

Frequency Sweep

By rotational frequency analysis, the dependence of the storage and loss modulus is recorded as a function of the angular frequency ω [rad/s]. During the measurements, a fixed strain rate of 10% was set. The measurement was repeated twice; both curves show interferences at high frequencies, while no crossover point was observed. Such interferences can occur if the measuring system is not ideal for the sample fluid or if agglomerations of molecules occur at high frequencies. The crossover point was calculated by the interpolation of the $G^{'}$ and $G^{''}$ curve.

The results are shown in Figure 3.5, in which the blue and red line illustrate the interpolation performed by the Rheocompass software. The calculated crossover point of the 3 wt% PEO solution was found at a frequency of ω = 109.53 rad/s and 71.026 Pa ($G^{'} = G^{''}$). Additionally, the shear relaxation time was calculated according to Equation 1.22; an average specific shear relaxation time of 151.66 ms was found. This value was used for the calculation of the elastocapillary number *Ec* (Equation 1.42). *Ec* was used to evaluate if the viscosity or elasticity determine the resistance of the sample against surface tension. The value for the surface tension was extracted from the publication of Man Won Kim (*78*). The resulting low elastocapillary number (Ec= 0.2999) indicates that the sample is only slightly affected by elastic forces. Therefore, it can be assumed that the thinning mechanism in the following extensional experiments is mainly controlled by viscosity effects. Table 3.2 summarizes the results obtained by interpolation of the storage and loss modulus curve.

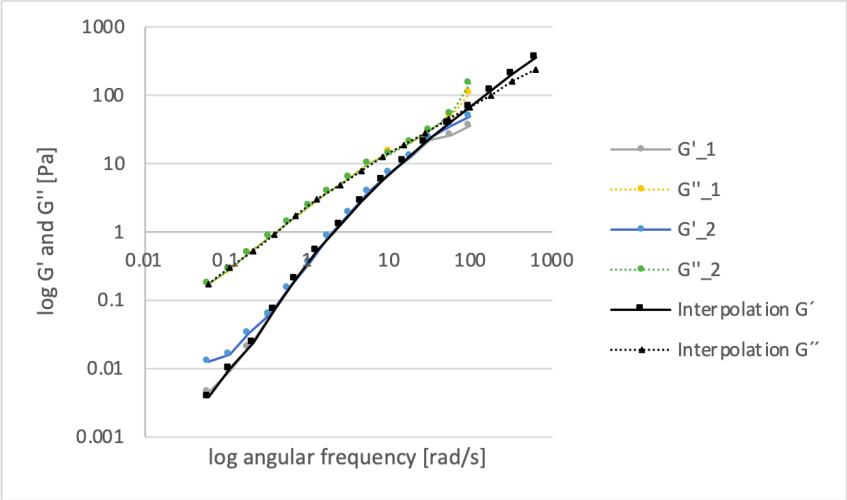

Figure 3.5: Summary of the shear analysis curves of PEO under frequency sweep conditions. Due to interferences at high angular frequency, the crossover point was calculated by interpolation. The interpolated curves are shown as black squares and triangles.

Table 3.2: Summary of the results from shear analyses of PEO. From the crossover point of G′ and G″, the shear relaxation time and the elastic number were calculated.

$G' = G''$ [Pa]	ω [rad/s]	λ_S [ms]	E_C
71.026	109.53	151.66	0.2999

3.1.3. Poly(isobutylene) in Decaline

Amplitude Sweep

The amplitude sweep of the NIST-standard is illustrated in Figure 3.6. The curves for storage and loss modulus were observed over a shear strain range from 0.01 to 1000%. The solution was identified as viscoelastic fluid: For the whole deformation region, the storage modulus has lower values than the loss modulus $G' < G''$. In comparison with the PEO solution, the difference between G' and G'' amounts to lower values. Furthermore, the measured values cover a higher range of about 100 Pa. Thus, it can be argued that the elastic amount of the sample is higher. This hypothesis was also supported by large ropey effects at room temperature.

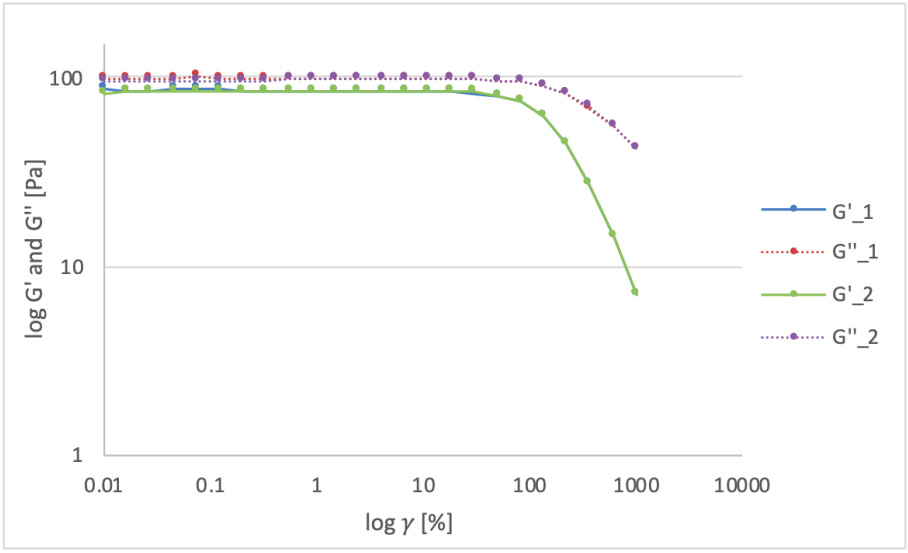

Figure 3.6: Amplitude sweep of PIB in decaline.

Frequency Sweep

The crossover point ($G' = G''$) was determined by frequency sweeps tests at a constant shear strain of 10%. The evolution of the storage and loss modulus were recorded as function of a variable angular frequency (Figure 3.7). The observed crossover point at ω= 11.93 rad/s and 181.51 Pa shows a less viscous behavior in comparison to the PEO solution. In summary, the crossover point was received at lower frequency and higher modulus values. Already above an angular frequency of 11.93 rad/s, the storage modulus is higher than the loss modulus. In addition,

the higher *Ec* number supports this hypothesis. The calculated values are listed in Table 3.3. Consequently, the elastic amount of PIB is higher than that of PEO.

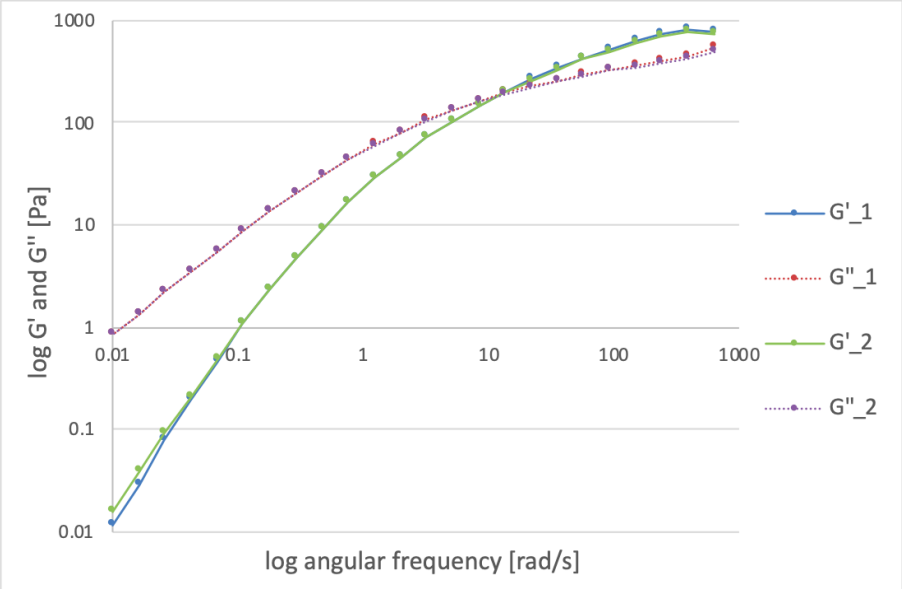

Figure 3.7: Frequency sweep of PIB in decaline. Dual determination of the behavior of G′ and G″ under variable angular frequency with the illustration of the obtained crossover point (G′= G″) at 11.93 rad/s.

Table 3.3: Summary of the results from the shear analysis of PIB in decaline.

$G' = G''$ [Pa]	ω [rad/s]	λ_S [ms]	E_C
183.51	11.93	83.80	1.061

3.1.4. Polystyrene

Amplitude Sweep

The analysis of the PS sample at variable shear strain was performed exemplarily for the sample with the highest molecular weight. The resulting diagram is shown in Figure 3.8. The red dotted line represents the loss module G', and the blue line G''. After initial fluctuations, $logG'$ and $logG''$ follow a linear trend. At shear rates above 10%, the storage modulus starts to decrease, which is indicative of the end of the LVE range. As a result, the constant shear strain for the frequency sweeps were examined by the boundary range of the LVE region (γ= 10%). In addition, it was found that the polymer melt shows a viscoelastic fluid behavior ($G' < G''$) at this specific temperature. The test temperature was selected according to the ideal

CaBER fluid thinning properties. For lower temperatures, a gel-like behavior was found and, thus, no filament evolution was possible.

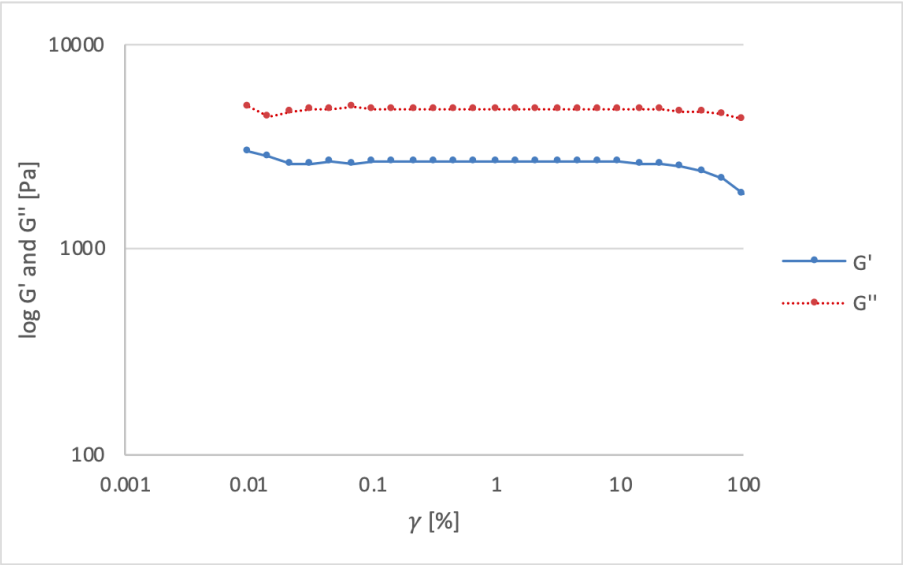

Figure 3.8: Amplitude sweep of PS $M_w = 260,000\ g \cdot mol^{-1}$ at a temperature of 250 °C.

Frequency Sweep

From Figure 3.9 and Figure 3.10, it can be seen that the crossover point lies outside the measurable range of the plate-plate system of the rheometer for PDMS with a molecular weight of M_w = 1,200 and 45,000 $g \cdot mol^{-1}$, respectively. Due to the low molecular weight and the high measuring temperature, the melt viscosity turned out to be too low for analysis with a plate-plate system. To measure such low-viscosity samples, an alternative measuring system, e.g. a double column system, needs to be used. In this case, no further analyses were carried out. The only measurable crossover point was obtained for the PS sample with the highest molecular weight ($M_w = 260,000\ g \cdot mol^{-1}$), for which the crossover point (G'=G'') was received using the Rheocompass software. The mean crossover point from the measurement in triplicate was at an angular frequency of 66.86 rad/s, and 28115 Pa. This means that elastic effects are predominant above 66.86 rad/s. Based on this relation between viscosity and elastic effects, the elastic amount of the PS sample could be estimated. Based on the inverse dependency of the relaxation time λ_S, a value of 93.87 ms was found.

Table 3.4: Results from the shear analysis of PS $M_w = 260,000\ g \cdot mol^{-1}$. Due to missing surface tension and density analysis at this temperature, the *Ec* number could not be calculated.

$G' = G''$ [Pa]	ω [rad/s]	λ_S	E_C
28115	66.86	14.96	-

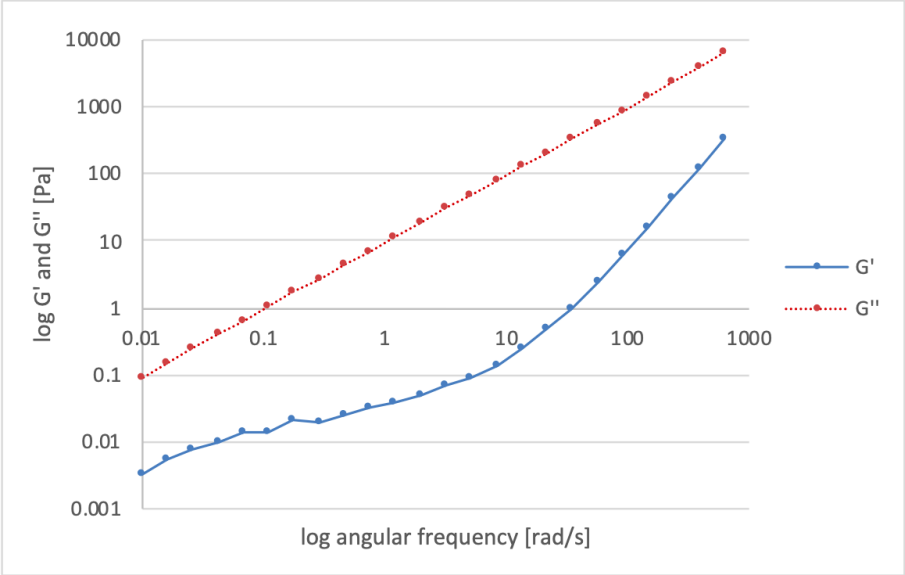

Figure 3.9: Frequency sweep of PS $M_w = 1,200\ g \cdot mol^{-1}$. The loss modulus is shown in dotted lines, and the storage modulus in continuous lines. The crossover point (G′ = G″) is outside the range of the plate-plate system.

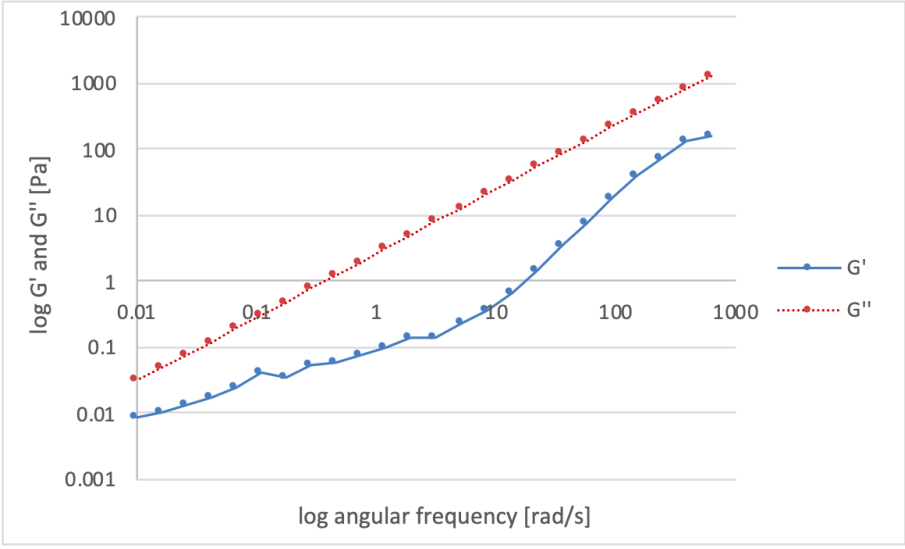

Figure 3.10: Frequency sweep of PS $M_w = 45,000\ g \cdot mol^{-1}$. The crossover point (G′ = G″) is outside the range of the plate-plate system.

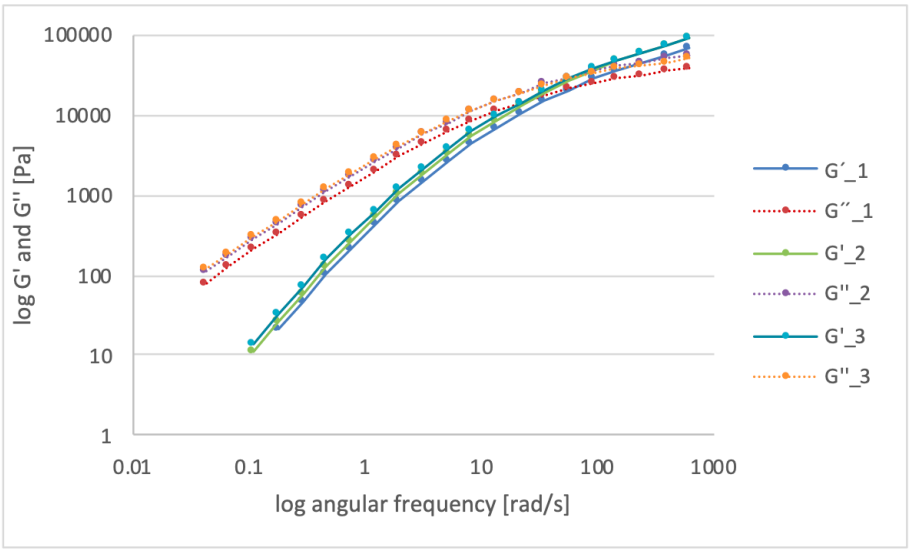

Figure 3.11: Frequency sweep of PS $M_w = 260,000\ g \cdot mol^{-1}$. Threefold measurement of the evolution of G′ and G″ as a function of a variable angular frequency. The loss modulus is illustrated in dotted lines, and the storage modulus in continuous lines.

3.2. CaBER Measurements with Prototype 2

3.2.1. Newtonian Fluids

3.2.1.1. Poly(dimethyl siloxane) PDMS 5 (η= 4.6 mPa·s)

The necking process of samples with a viscosity lower than 70 mPa·s is mainly controlled by inertiacapillary effects. Hence, the break-up time t_v and the capillary velocity v_{cap} can be calculated by Equation 1.39 and Equation 3.1. In order to analyze PDMS 5 with its very short experimental period of 38.6 ms, a high frame rate of 2000 must be set. The maximum recording duration of one picture was 542 μs. To reach this rate, the image field was reduced by a partial scan of Top= 1050 (Cl Configtool). The advantage of this adjustment is that many pictures could be recorded during the experiment over a short period of time. The disadvantage is that only a short part of the experimental area is visible and it cannot be guaranteed that the smallest diameter is in the analysis region.

In theory, the sample to be analyzed is out of the operational limit of 70 mPa·s for CaBER measurements (Figure 1.14). Hence, the sample should not be able to form a stable fluid bridge between the two endplates. Aiming to confirm the limitations postulated by Rodd *et al.* (12), it was tried to measure the break-up time and the capillary velocity (Equation 3.1 to Equation 3.3).

$$t_v = \int_R^0 \frac{dR}{U_\rho} = 1.9531 \cdot \sqrt{\frac{\rho R^3}{\sigma}} \tag{3.1}$$

$$t_v = 1.9531 \cdot \sqrt{\frac{911.2\ kg/m^3 \cdot (2.0\ mm)^3}{0.0186\ N/m}} = 38.6\ ms \tag{3.2}$$

$$v_{cap} = 0.3413 \cdot \sqrt{\frac{0.0186\ N/m}{911.2\ kg/m^3 \cdot 2.0\ mm}} = 34.48\ mm/s \tag{3.3}$$

The experimental results show that it is possible to place a stable fluid bridge between the endplates at their initial position of h_0= 1.5 mm. The inertiacapillary forces are strong enough to stabilize the fluid against gravitational sagging and effects from surface tension. As soon as the endplates start moving, the fluid stability decreases very fast. Already in the first recorded picture after 542 μs, it was noted that the fluid bridge was broken. Thus, it was not possible to reach the final endplate position with a stable fluid bridge. In conclusion, neither the break-up time nor the capillary velocity is measurable with this experimental set-up.

3.2.1.2. Poly(dimethyl siloxane) PDMS 100 (η= 100 mPa·s)

The viscosity of the sample is in the range of the limiting value for viscocapillary controlled filament thinning velocities. Hence, it was assumed that the capillary velocity is influenced by two different forces, namely inertia- and viscocapillary forces. For the discussion of the force ratio, the Ohnesorge number can be calculated, which yields the ratio of inertia forces and the viscosity. The inertia-controlled thinning is dependent on the filament radius in contrary to the viscocapillary-controlled velocity. Thus, this sample was used to evaluate the endplate diameter as influencing factor. In this study, endplate diameters of 4 mm, 6 mm, and 8 mm were used. For each experiment, the capillary velocity and the break-up time were calculated. Additionally, the predominant velocity was determined over the pathway from the initial diameter to the break-up event. The thinning velocities were plotted over time; the intersection point gives information about the particular amount of force. A summary of all results is listed in Table 3.5 and shown in Figure 3.20. The experimental settings for the CaBER measurements were a frame rate of 2000 fps and a maximum recording duration of 753 μs. The partial scan of the recorded picture was Top = 784. The temperature was fixed at 20 °C. During the first experiments, it was observed that the fluid was sensible to occurring air streams in the chamber: The air cooling system of the device causes problems during the filament observation. The fluid

bridge shows vibrations caused by the air stream and, due to these instability mechanisms, the fluid bridge breaks much faster than expected. In conclusion, the initial experiments with continuous air cooling yielded irreproducible results.

Aiming to overcome this problem, the chamber was previously cooled to -15 °C. After sample loading, the air stream was switched off, and the enclosed system was heated to the targeted temperature. At an accuracy of ± 0.05 °C, the measurement was started. The theoretical calculation of the capillary velocity and the break-up time is presented in Equation 3.4 to Equation 3.10.

$$v_{cap(visco)} = 0.0709 \cdot \frac{0.0202\ N/m}{0.106\ Pa \cdot s} = 0.0135\ m/s \tag{3.4}$$

$$v_{cap(inertia(D_P=4\ mm))} = 0.3413 \cdot \sqrt{\frac{0.0202\ N/m}{966.0\ kg/m^3 \cdot 2.0\ mm}} = 0.0011\ m/s \tag{3.5}$$

$$v_{cap(inertia(D_P=6\ mm))} = 0.3413 \cdot \sqrt{\frac{0.0202\ N/m}{966.0\ kg/m^3 \cdot 3.0\ mm}} = 0.0009\ m/s \tag{3.6}$$

$$v_{cap(inertia(D_P=8\ mm))} = 0.3413 \cdot \sqrt{\frac{0.0202\ N/m}{966.0\ kg/m^3 \cdot 4.0\ mm}} = 0.00078\ m/s \tag{3.7}$$

$$t_{v(D_P=4\ mm)} = 14.1 \cdot \frac{0.106\ Pa \cdot s \cdot 2.0\ mm}{0.0202\ N/m} = 0.148\ s \tag{3.8}$$

$$t_{v(D_P=6\ mm)} = 14.1 \cdot \frac{0.106\ Pa \cdot s \cdot 3.0\ mm}{0.0202\ N/m} = 0.222\ s \tag{3.9}$$

$$t_{v(D_P=8\ mm)} = 14.1 \cdot \frac{0.106\ Pa \cdot s \cdot 4.0\ mm}{0.0202\ N/m} = 0.296\ s \tag{3.10}$$

Figure 3.12 and Figure 3.13 illustrate the results of the analysis of PDMS 100 with an endplate diameter of 4.0 mm. In Figure 3.12, the filament evolution over the whole experimental period is shown. At the beginning of the experiment, the filament diameter is the same as the endplate diameter and starts to decrease as the endplates start moving. The movement of the lower endplate to its final position can be followed in the diagram. The time period until a stable linear filament decrease is visible took approximately 24 ms. The difference to the real time for the achievement of the endplate position arises from the fact that not all pictures were evaluated: In order to reduce the amount of data, only the pictures that were recorded a few milliseconds before the endplate movement were analyzed. Hence, the first milliseconds are not included in the experimental time. The calculation of the filament thinning forces is not affected by this evaluation method. Based on specific thinning controlling forces, the endplate position can be reconstructed from the generated diagrams.

The diameter ratio D/D_0 at the final endplate position for this sample was 0.12. The range from D/D_0 = 0.12 (R = 0.476 mm) to filament break is plotted in Figure 3.13. The mean linear slope of the diameter ratio D/D_0 as a function of time is -2.5242.

Aiming to identify the predominant material property, the inertia- and viscosity-controlled thinning velocity was plotted as a function of the filament radius in Figure 3.14. The thinning mechanism changes as the filament diameter decreases, depending on the material property with the highest resistance against squeezing of the surface tension. In this case, the path of the predominant velocity was marked in a dashed line. For bigger filament radii, inertial material properties dominate the filament thinning process. At the intersection point of R= 0.534 mm, the thinning-controlled velocity changes to viscosity-controlled thinning. In summary, at Oh $\leq$ 1.038, viscous effects determine the filament thinning. As described herein above, the stable linear filament decreases after 24 ms and a

filament radius of 0.4776 mm. Thus, the inertia effects do not have an impact on the capillary velocity. The capillary velocity can be theoretically calculated by viscocapillary thinning forces only. The experimental capillary velocity was calculated from the diameter evolution as a function of time. The mean capillary velocity of 0.0125 m/s shows a deviation of only 0.000707 m/s to the theoretical value.

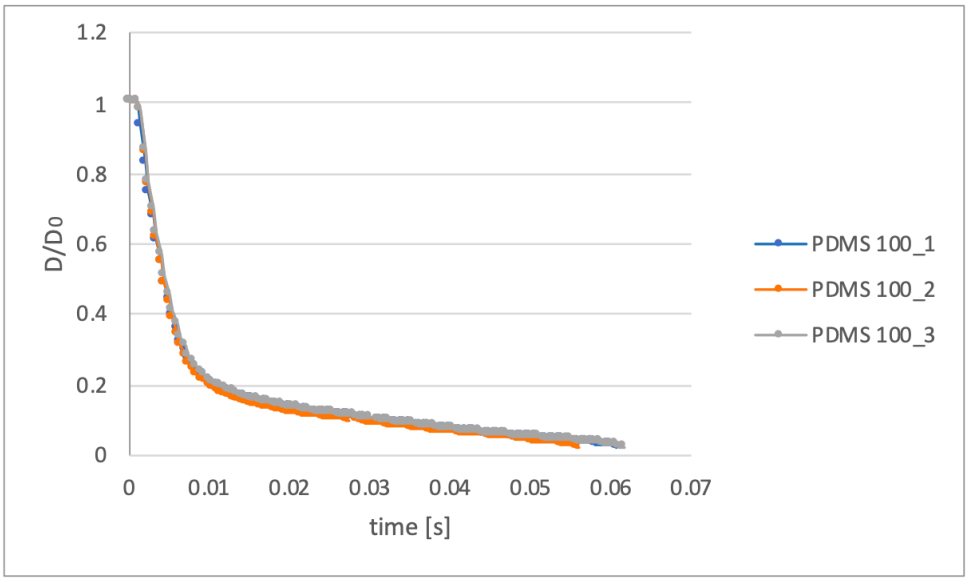

Figure 3.12: Filament evolution of PDMS 100 at 20 °C and D_P= 4.0 mm.

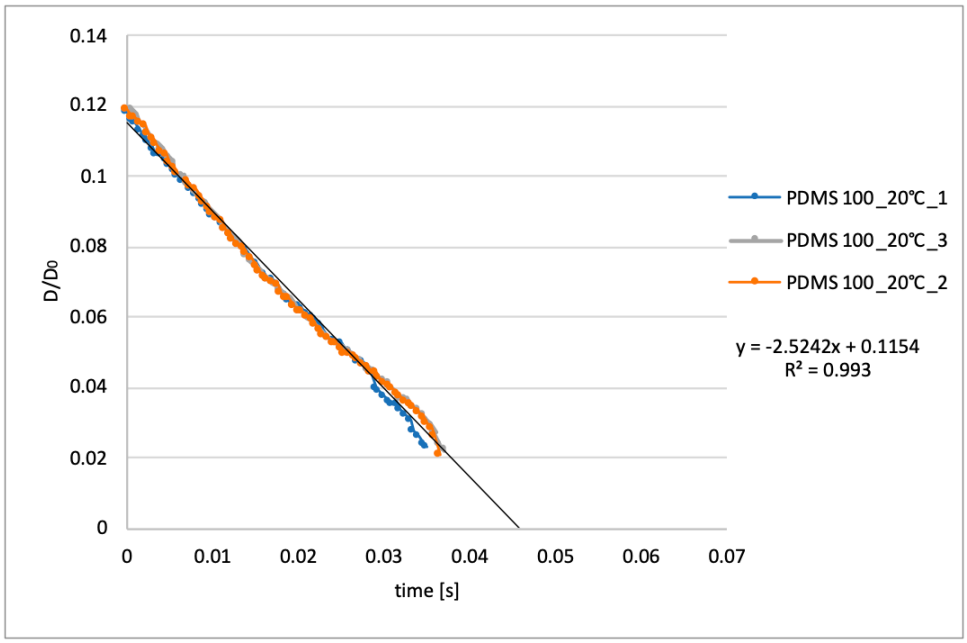

Figure 3.13: Calculation of the capillary velocity of PDMS 100 at 20 °C and an endplate diameter of D_P= 4.0 mm.

The result is in the range of the theoretical value for the viscocapillary thinning velocity of 0.0135 m/s and confirms the observations form Figure 3.14. The break-up time of the filament was found at 0.0615 s. By increasing the endplate diameter, it was tried to increase the experimental period. An increased filament break-up time would facilitate the observation of the filament evolution. In theory, the increasing of the diameter should yield an increased filament lifetime with a ratio $t_{v(4\ mm)}/t_{v(6\ mm)}$= 0.667.

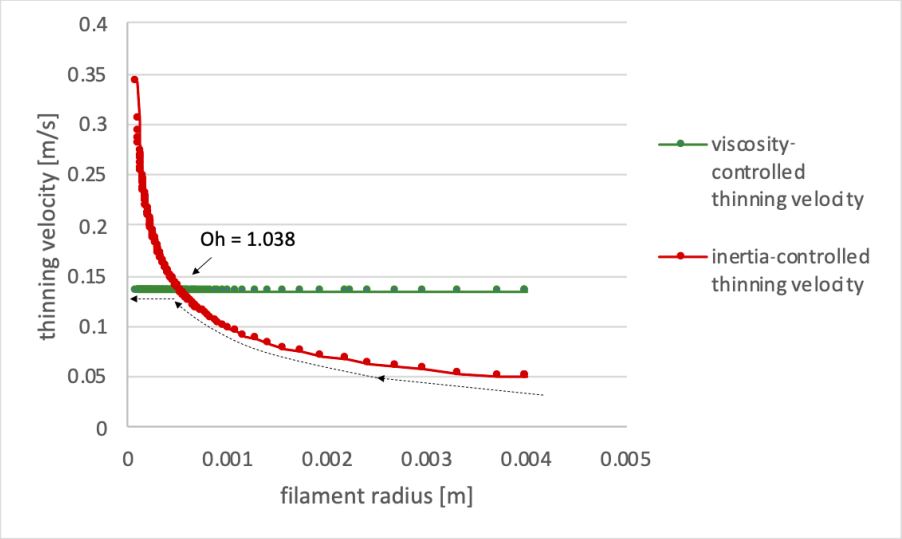

Figure 3.14: Illustration of the thinning-controlling velocities of the sample PDMS 100 for an endplate diameter of D_p= 4.0 mm. The evolution direction of the filament radius is from right to left (from the biggest filament radius to the smallest radius until the break-up event). The dashed line represents the direction of the filament thinning evolution.

The experiment was repeated with the same conditions except for the increased endplate diameter of D_P= 6.0 mm. The results are illustrated in Figure 3.15 and Figure 3.16. In order to compare the results with other endplate diameters, the linear slope was also plotted after D/D_0= 0.12 was reached. The mean linear slope of the samples with an endplate of 6.0 mm was -1.979. The mean calculated capillary velocity of this linear region was 0.0130 m/s which a deviation of 0.0005 m/s to the theoretical value. Figure 3.17 shows the thinning velocities for an endplate diameter of 6.0 mm. The intersection point of inertia- and viscosity-controlled thinning velocity shifts to lower Oh values. The filament radius at this point was 0.62 mm and is below the defined limit of the endplate position after t = 24 ms (R = 0.70 mm).

Based on this observation, it can be argued that the filament thinning is slightly affected by inertia material properties. However, the calculated capillary velocity shows no significant alterations. The time of impact for inertia-controlled thinning velocities is too short to create significant changes in the slope of the filament thinning. The conclusion of these observations is that the capillary velocity remains unaffected by an increased endplate diameter. This result is in line with the theoretical background. From the equation of the viscosity-controlled thinning, it is known that the velocity is independent of the filament radius. In comparison with the thinning velocity, the maximum break-up time of the fluid bridge is dependent on the initial radius. The filament lifetime rises up to 0.0825 s. The experimental ratio of $t_{v(4mm)}/t_{v(6mm)}$ was 0.676. Although the experimental values differ from the theoretically calculated ones, the ratio lies in the expected range. It is assumed that the differences in the break-up times occur due to observation limitations based on the reduced illustration part.

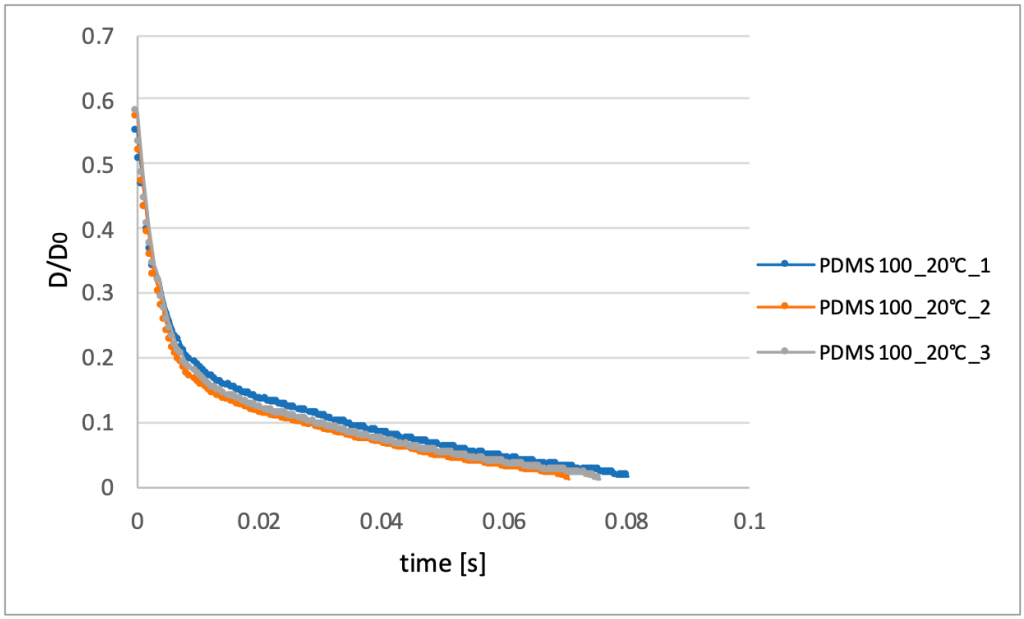

Figure 3.15: Filament evolution of PDMS 100 at 20 °C and D_P=6.0 mm.

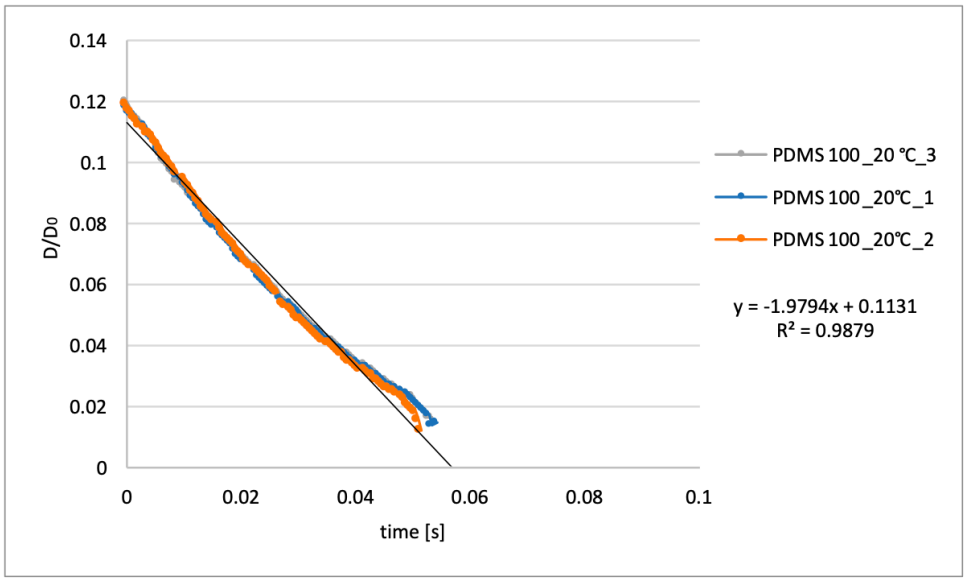

Figure 3.16: Calculation of the capillary velocity of PDMS 100 at 20 °C and an endplate diameter of D_P= 6.0 mm.

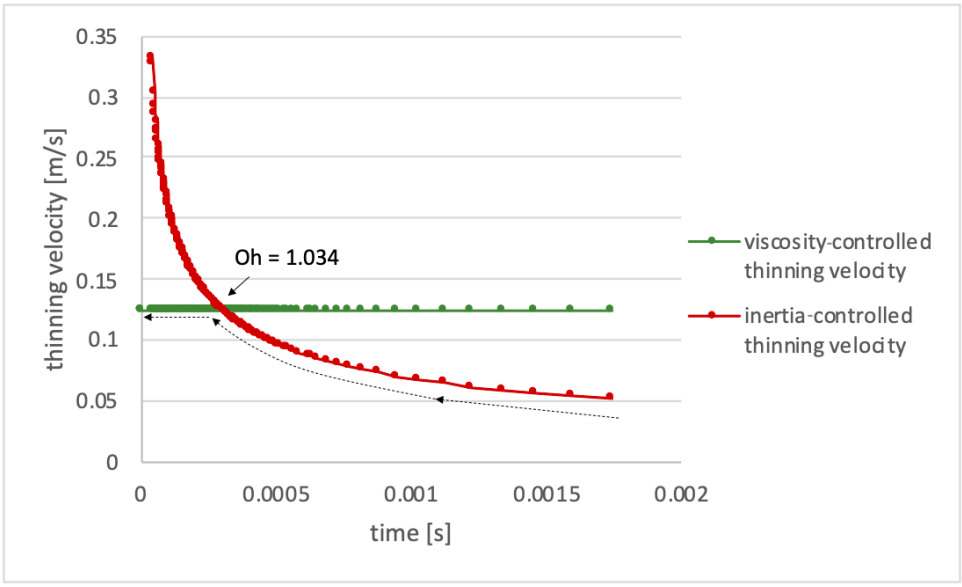

Figure 3.17: Illustration of the thinning-controlling velocities of the sample PDMS 100 for an endplate diameter of D_P= 6.0 mm. The dashed line represents the direction of the filament thinning evolution.

As a last step, the experiment was repeated with an endplate diameter of D_P= 8.0 mm (Figure 3.18 and Figure 3.19). The evaluation of the experimental data was performed as for the other endplate diameters. The mean calculated capillary velocity was 0.0154 m/s and shows the biggest deviation of 0.00134 m/s from the theoretical value. For the comparison of these results, Figure 3.20 was drawn. Due to the increased initial diameter, the filament radius after 24 ms was 0.11 mm. This value is reasonable higher than for the other experiments and causes an

increased influence of inertiacapillary mechanisms in measurement. The analysis of the same time period reveals that the fluid is affected by inertia thinning velocities until t = 51 ms. The experimentally found ratio of $t_{v(6mm)}/t_{v(8mm)}$ is 0.82.

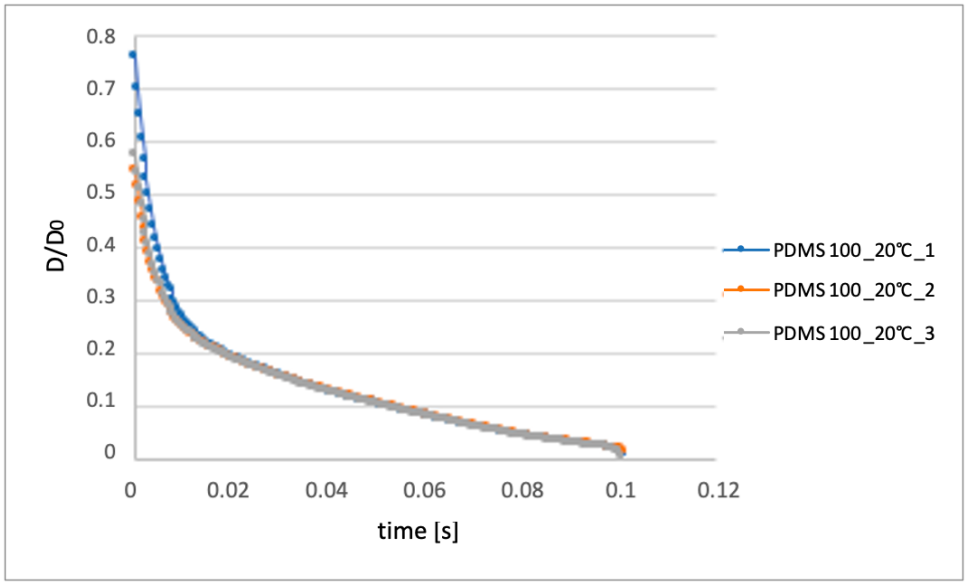

Figure 3.18: Diagram of the filament thinning evolution of PDMS 100 (20 °C and D_P= 8.0 mm).

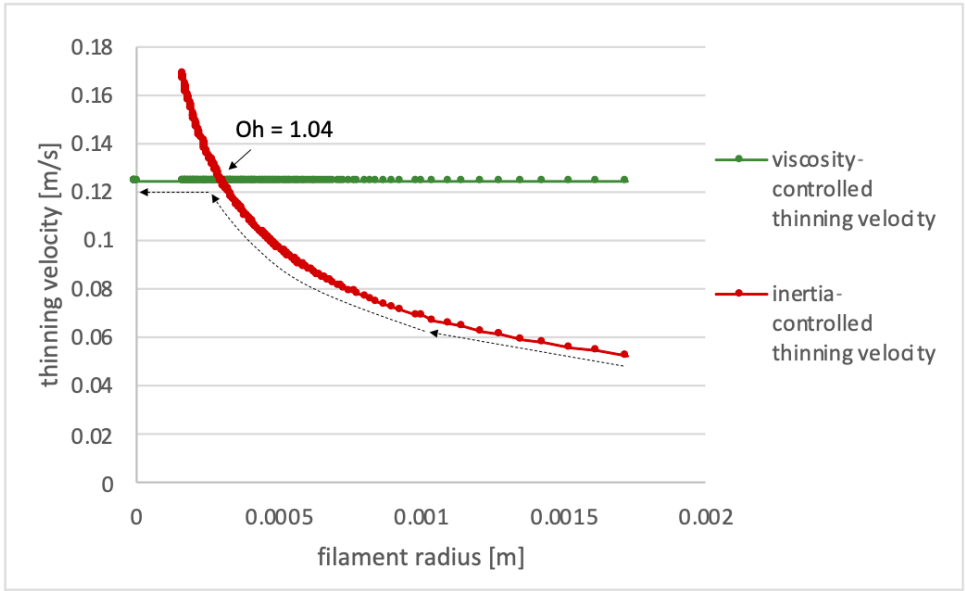

Figure 3.19: Illustration of the thinning velocities during the CaBER experiment with the sample PDMS 100 and an endplate diameter of D_P= 8.0 mm. The dashed line represents the direction of the radius evolution in dependence of time.

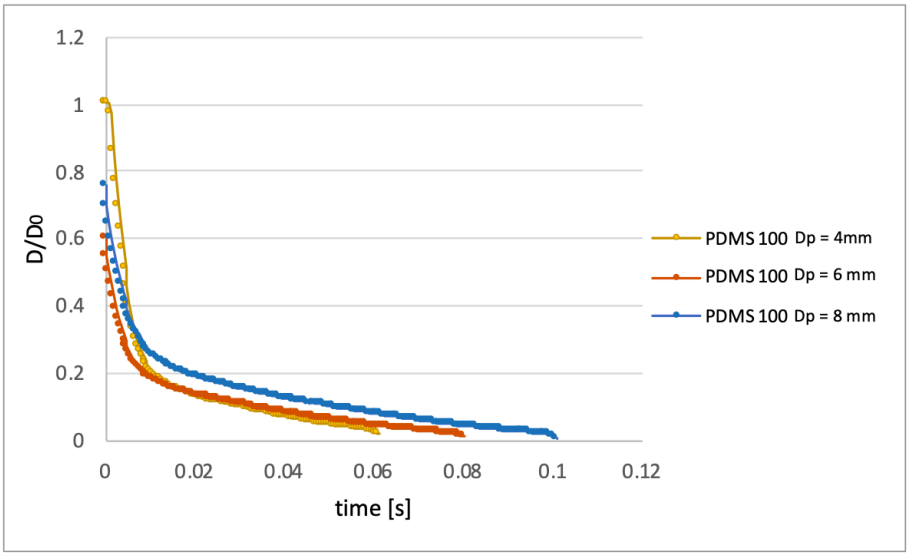

Figure 3.20: Overview of the results from the endplate determination with the sample PDMS 100 at 20°C.

Table 3.5: Summary of the data from CaBER analyses of PDMS 100 with different endplate diameters.

D_P [mm]	Temperature [°C]	v_{cap} [m/s]	O_h[1]	Slope D/D_0 vs time
4.0	20	0.0120	1.038	-2.52
4.0	20	0.0131	1.041	-2.69
4.0	20	0.0125	1.038	-2.52
6.0	20	0.0128	1.034	-1.86
6.0	20	0.0131	1.036	-1.98
6.0	20	0.0132	1.038	-1.86
8.0	20	0.0147	1.04	-2.47
8.0	20	0.0156	1.04	-2.52
8.0	20	0.0160	1.04	-2.52

[1]The Ohnesorge number was calculated at the intersection point of the thinning controlling velocities.

3.2.1.3. Poly(dimethyl siloxane) PDMS 5000 (η= 5.0 Pa·s)

The high-viscosity sample PDMS 5000 was used to determine the influence of the air stream and the temperature during the experiment. The determination of the impact of air stream was performed with PDMS 5000 due to the fact that the results are transferable to all other samples with a lower viscosity. As described in subsection 2.2.3, temperature control was achieved using a gas chiller device. The air stream is previously cooled down and is continuously injected in the CTD chamber during the whole experiment. This method is very effective to yield a homogeneous temperature distribution and a narrow temperature variation of 0.02 °C. During the first experiments, doubts arose on the accuracy of the measurements because of great fluctuations within the experimental results. An exemplary measurement is shown in Figure 3.21. The filament bridge shows strong vibrations caused by the air stream in the chamber. Especially small diameters were affected by the air stream. As a consequence, the evaluation of the filament thinning and the capillary thinning velocity was impossible. The results of this observation show that it is essential to switch off the air stream before the experiment starts.

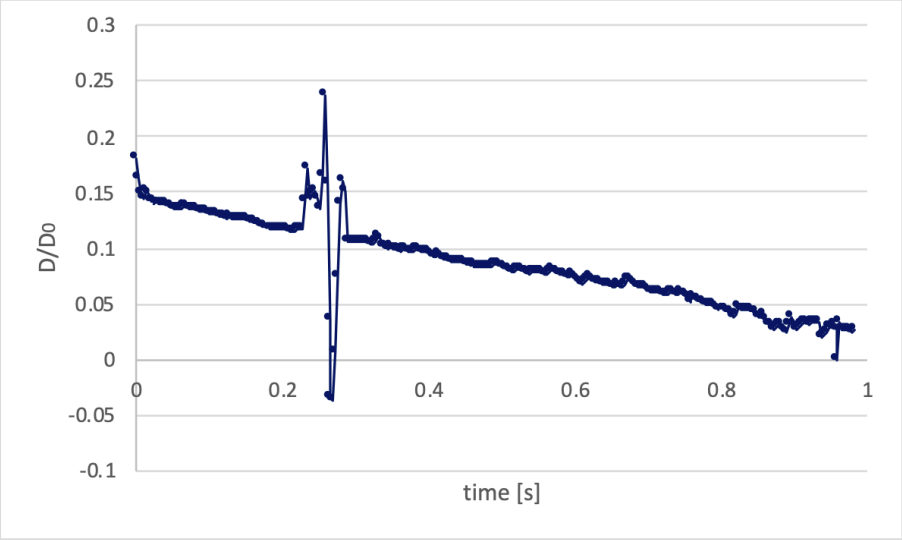

Figure 3.21: Diagram of the PDMS 5000 thinning mechanism under continuous air flow. The course of the thinning curve illustrates the filament oscillations caused by the convective air flow.

Temperature influence on the thinning process

The viscosity of a sample is an important parameter for the evaluation of the driving mechanisms in the filament thinning processes and has great impact on the filament lifetime. In principle, the viscosity describes the resistance of a fluid against flow mechanisms. At a given temperature, Newtonian fluids have a constant shear viscosity. If the temperature is raised, the flow resistance decreases and, thus, the viscosity also decreases. For the observation of this phenomenon in free surface flows, CaBER measurements were performed at 20, 50 and 100 °C. At the respective temperatures, the capillary velocity and the apparent viscosity were calculated. The calculated apparent viscosities and shear viscosities were used for the determination of the Trouton ratio.

The thinning-controlling velocities were plotted to evaluate the influencing material properties during the experiment. In contrary to PDMS 100, the thinning velocity of PDMS 5000 is only driven by viscosity (Figure 3.22). The amount of the elastic-controlled velocity was determined by shear rheology measurements.

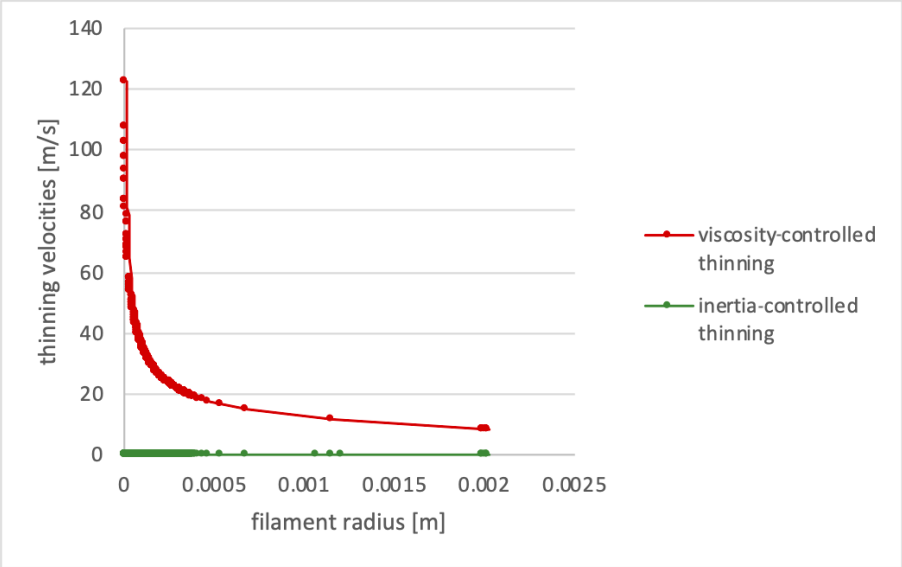

Figure 3.22: Diagram of the thinning-controlling velocities of PDMS 5000 (20 °C and D_P= 4.0 mm). The direction of thinning is in the direction of large diameters (right) to small diameters (left).

Amplitude sweep measurements were performed to determine the linear viscoelastic region of PDMS 5000. A MCR rheometer with a cone plate (CP50.05 and L-PP50/TDTTS) was used for the experiment. A constant angular frequency

of 3.14 rad/s was set. It was found that the Newtonian region was extended to high shear rates and, thus, the end of the linear viscoelastic region was outside of the measurement limit of the device. Therefore, the elastic amount of the sample was set as negligible for the evaluation of thinning mechanisms. The theoretically calculated value for the capillary velocity of PDMS 5000 was 0.0035 m/s. The values of the surface tension and density of the sample were taken from literature. The theoretical values of v_{cap}, η_{app} and *Tr* could only be calculated for the sample at room temperature (Table 3.7). The measured and calculated results are given in Table 3.6 and Table 3.7.

Table 3.6: Summary of the CaBER results with PDMS 5000 at different temperatures. The calculated mean value and deviation refers to v_{cap} at a given temperature.

Temperature [°C]	v_{cap} *[m/s]*	*Mean value* v_{cap} *[m/s]*	*Deviation [m/s]*	*SlopeD/D$_0$ vs time*
20	0.00048			-0.120
20	0.00039			-0.109
20	0.00051	0.00046	$6.25 \cdot 10^{-5}$	-0.128
50	0.00060			-0.174
50	0.00061			-0.183
50	0.00062	0.00061	$1.0 \cdot 10^{-5}$	-0.186
100	0.0011			-0.284
100	0.0010			-0.274
100	0.0010	0.00103	$5.77 \cdot 10^{-5}$	-0.283

Table 3.7: Calculated η_{app} and the according Trouton ratio (Tr) of PDMS 5000 at 20 °C.

Temperature [°C]	η_{app} *[Pa·s]*	*Tr*
20	22.32	4.34
20	18.31	3.56
20	17.01	3.31

Figure 3.23 illustrates the comparison of the capillary viscosity at different temperatures. In general, the filament lifetime was set as approximate value. As described above, the observation line is too imprecise to determine the thinnest diameter of the filament during the experiment. A solution of this problem would be an evaluation method, in which the whole filament bridge is analyzed. The advantage compared to a partial examination is the possibility to follow the evolution of filament bridge over the whole experimental region; thus, the correct

smallest diameter can be easily identified. To generate the real break-up time, it is essential to calculate the data for the smallest diameter of the filament. However, the generated data can be used for the interpretation of the temperature influence of the capillary velocity. The ratio between the filament thinning velocity at different temperatures was determined at the filament break-up position. The time consumed to reach this point was used as reference to calculate the ratio between the experiments.

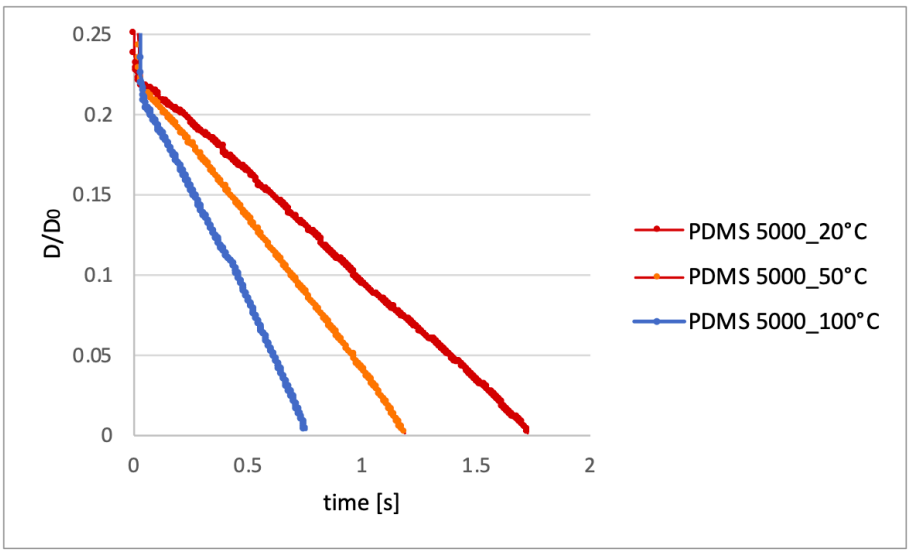

Figure 3.23: Illustration of the filament thinning of PDMS 5000 at different temperatures, recorded as a function of time.

At 20 °C, the sample consumed the longest time of 1.722 s for filament break-up. The high viscosity of the sample leads to a higher filament lifetime. The measurement at 50 °C shows a reduced time consumption of 1.177 s. Correspondingly, the increased temperature decreases the capillary velocity with a ratio t_{v20}/t_{v50} of 1.5. A similar effect was found at a temperature of 100 °C. The low viscosity at high temperatures leads to short filament lifetimes. The thinning process was increased with a ratio of 1.6, resulting in a break-up time of 0.733 s. The experimental data were verified by theoretical calculations at the viscosity-controlled thinning velocity (σ/η). The surface tension at the particular temperatures was calculated by contact-angle measurements. The viscosity η was determined by shear rheological measurements described in section 3.1.

Influence of the separation velocity on the filament thinning

The influence of the endplate separation velocity was examined with two different moving profiles. According to subsection 2.1.2, the separation profile of the endplates was set in non-damped mode. The data of the Newtonian fluid were compared with the results from the measurements under damped-step mechanism at 20 °C. The high-viscosity sample showed, in contrast to PDMS 100 and PEO, no vibrational interferences. The molecules in the fluid are able to stabilize the collision vibrations much faster than in the lower-viscosity samples. Thus, the collision event showed no influence on the data. Also, v_{cap} remains unaffected by the increased separation velocity. The values obtained are listed in Table 3.8. The calculation of η_{app} and the Trouton ratio was performed as for the damped-step moving profile. According to the narrow deviation value, it can be argued that Newtonian fluids are independent of the separation velocity.

Table 3.8: CaBER results of PDMS 5000 at non- damped endplate separation mode.

Temperature [°C]	v_{cap} *[m/s]*	*SlopeD/D$_0$ vs time*	η_{app} *[Pa·s]*	*Tr*
20	0.00046	-0.1147	18.88	3.67
20	0.00048	-0.1228	18.55	3.55
20	0.00045	-0.1148	19.45	3.78

3.2.2. Non-Newtonian Fluids

3.2.2.1. Poly(ethylene oxide) Solution (3 $wt\%$ M_w= 10^6 $g \cdot mol^{-1}$)

The examination of the viscoelastic extensional behavior was performed with a poly(ethylene oxide) solution. According to the study of Arnolds *et al.* (3), the experiment was operated at a temperature of 20 °C and an initial endplate separation of h_0 = 3.0 mm. The exponential thinning of the filament diameter was plotted as a logarithmic scale of D/D_0 as a function of time. To evaluate the endplate influence on the filament thinning mechanism, also for the viscoelastic fluid, different endplate diameters were used (D_p= 4.0 and 6.0 mm).

The relaxation time of PEO was investigated by evaluating the slope of the linear region with a continuous deformation rate $\dot{\epsilon}$. Figure 3.24 shows an exemplary exponential thinning profile with the continuous deformation rate marked as a black line. According to Equation 3.11, the relaxation time of the sample was calculated.

$$ln(\frac{D_t}{D_0}) \propto -\frac{1}{3\lambda_E} \cdot t \tag{3.11}$$

From literature, it is known that a specific relaxation time can only be measured at a concentration between the saturated concentration c^* and the entanglement concentration c_e. If the concentration increases, the deformation rate $\dot{\epsilon}$ decreases, and λ_E increases. As a result, the fluid shows much higher filament lifetimes. A PEO concentration of 3 $wt\%$ fulfills the denoted limitations ($c^* < c < c_e$), while for higher concentrated samples, the exponential evolution cannot be followed any more.(3)

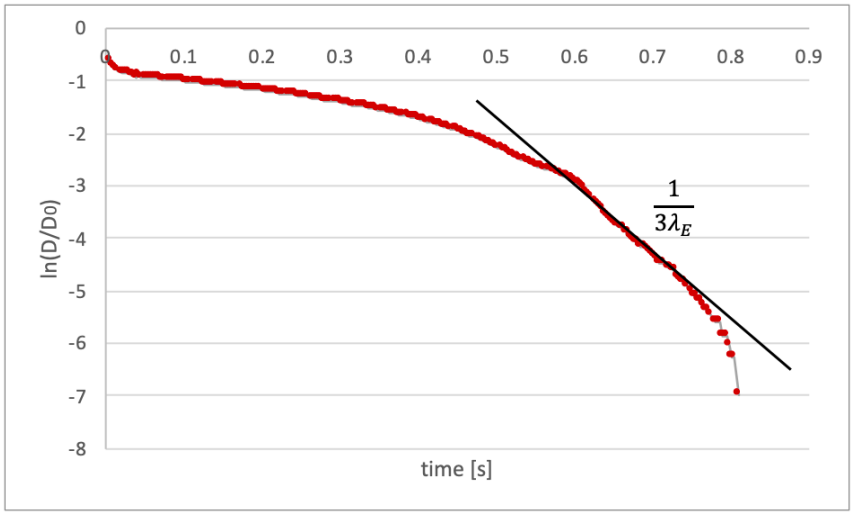

Figure 3.24: Exponential thinning of low-viscosity non-Newtonian liquids. The diagram shows an exemplary thinning profile of PEO. In addition, the continuous deformation range is shown as a black line. The formula for the calculation of the resulting relaxation time is shown in the diagram.

Endplate diameter influence

It was observed that the sample was highly affected by dry-out processes. The gas chiller experimental set-up (for the temperature regulation) is not suitable for measuring drying-sensitive samples due to changes of the sample concentration. This effect was visible especially for long-lasting temperature adjustments.

The high sample-to-volume ratio at the resting state yields a large contact surface for the injected cooling gas, which facilitates dry-out processes. The occurring water evaporation has great impact on the obtained data and the calculated relaxation times. In conclusion, it was found that no reproducible results could be obtained for dry-out sensitive samples with this experimental setting. To overcome this problem, a reasonable compromise was found in pre-tempering the CTD-chamber and subsequent sample loading without continuous air stream. Due to the absence of circulating air in the chamber after sample loading, an accurate tempering of the sample liquid cannot be ensured; a temperature variation of $\pm$ 5 K (15 - 20 °C) needs to be assumed. However, with this tempering method, more reproducible results could be obtained in comparison to the continuous convectional gas flow method. Nevertheless, occurring temperature variations cause issues (Figure 3.25). The diagram shows significant variation between the individual measurements. This observation was related to temperature adjustment issues and a consequently higher fluid temperature during the extensional measurement. An increase of the fluid temperature leads to an increase of $\dot{\epsilon}$ and a decrease of λ_E. The blue curve was neglected for the calculation of the mean relaxation time of the PEO sample with an endplate diameter of D_P= 6.0 mm.

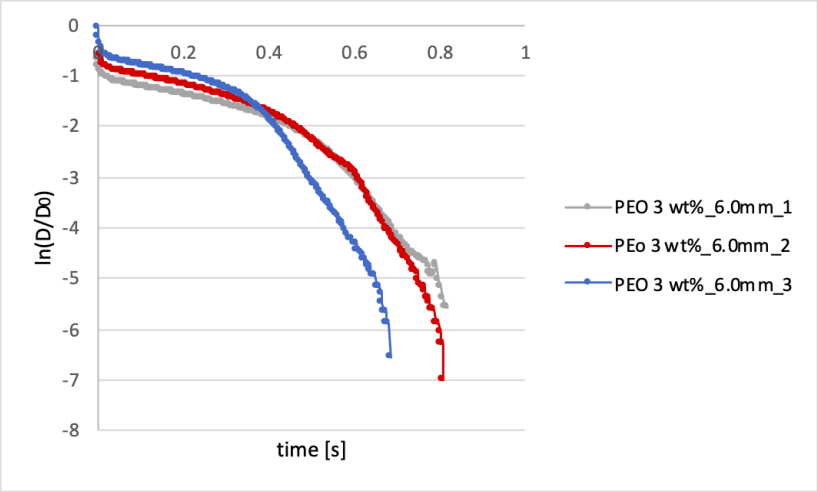

Figure 3.25: Exponential thinning of the viscoelastic PEO solution at 20 °C and an endplate diameter of 6.0 mm.

The thinning curves with an endplate diameter of 4.0 mm are shown in Figure 3.26. The mean relaxation time was calculated from all three measurements of the sample.

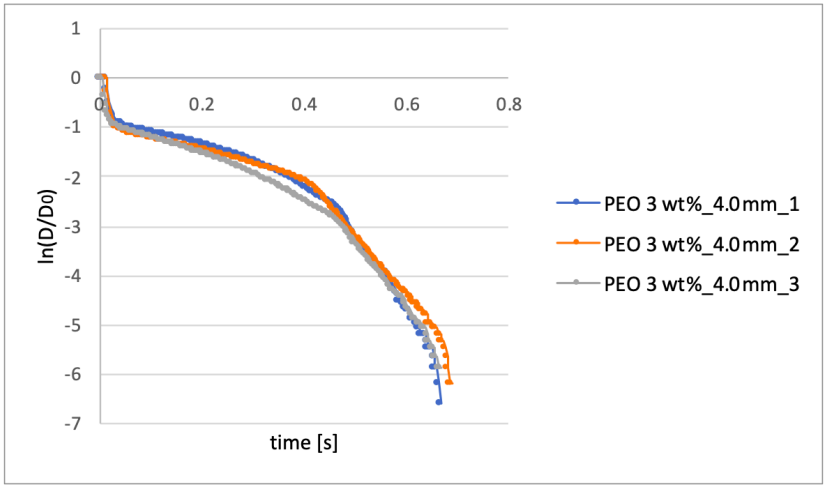

Figure 3.26: Exponential thinning of the viscoelastic PEO solution at 20 °C and an endplate diameter of 4.0 mm.

For an endplate diameter of 4.0 mm, the mean relaxation time was 49.54 ms, and the corresponding break-up time was 0.675 s. For an endplate diameter of 6.0 mm, a slightly lower relaxation time of 48.54 ms was found. A higher deformation rate leads to lower relaxation times and higher filament lifetimes of 0.746 s. Both measurements lie in the range of the literature value of 49.3 ± 7.4 ms. In summary, minor influences of the endplate diameter can be determined for the viscoelastic fluid. Since the denoted standard deviation of ± 7.4 ms is large, no exact influence of the endplate diameter on the relaxation time could be proven. The results of the extensional measurements and the calculated values are listed in Table 3.9.

Table 3.9: List of the obtained relaxation times of PEO 3 wt% and the according calculated η_{app} and Trouton ratio.

D_p [mm]	$\dot{\epsilon}$ [m/s]	λ_E [ms]	η_{app} [Pa·s]	Trouton ratio
4.0	-15.45	43.16	521.02	9.560
4.0	-13.19	50.55	744.14	11.05
4.0	-12.14	54.91	478.88	9.241
6.0	-14.51	45.98	871.39	9.312
6.0	-12.86	51.85	646.87	10.44
6.0	-9.908	67.29	128.04	4.319
4.0 (RT)[2]	-12.97	51.40	678.2	10.64
4.0 (RT)	-14.10	47.27	1099	12.99
4.0 (RT)	-12.78	52.15	627.0	10.31

[2]The shortcut *RT* acronyms room-temperature measurements.

Temperature and concentration influence

The effect of temperature and concentration changes on λ_E was proven by room-temperature measurements. The measurements were performed with an endplate diameter of D_p= 4.0 mm, without any additional cooling or heating treatment (Figure 3.27). The standard deviation of the relaxation time was 2.63 in comparison to the experiments at 20 °C (D_p= 4.0 mm), at which the deviation was 5.94. Hence, the reproducibility of measurements can be improved by maintaining specific influencing factors. The calculated value of λ_E of 50.27 ms is in the range of the literature value. However, the value is slightly increased in comparison with the measurements at 20 °C. In conclusion, for polymeric solutions, the absence of side-reactions simplifies the sample loading, and more accurate results can be obtained. The measurement at room-temperature should be favored for dry-out sensitive samples.

As described in the theory part, the yield viscosity during CaBER measurements is called apparent, if no additional axial force is measured. As it was impossible to measure the occurring axial forces with the developed measuring device, only one value of η_E and the resulting Trouton ratio was calculated. The values were calculated according to Equation 3.12 and Equation 3.13.

From the research of Sachsenheimer *et al.* (*37*), it is known that for poly(ethylene oxide) (10^6 $g \cdot mol^{-1}$) solutions with low concentrations, a Trouton ratio of 9.5 $\pm$ 0.8 can be found. These observations were referred to non-linear changes of the polymer concentration during the initial step strain. Consequently, the capillary thinning does not start from the equilibrium position, where the Trouton ratio equals three times η_S. The same findings were also established in this study. The calculated ratios between extensional and shear viscosity were much higher than the predicted relation of Trouton. For an endplate diameter of D_P= 4.0 mm, a mean *Tr* of 9.95 was found. The experiments at room-temperature showed an increased *Tr* ratio by a factor of 1.14 in comparison to the measurements at 20 °C. Obviously, small changes in the fluid viscosity and surface tension based on slightly increased temperatures result in significant variations. The outlier meas-

urement shown in Figure 3.25 exhibits great variations also in these calculations. The found *Tr* ratio shows the smallest influence to the initial step strain.

$$\eta_{app} = \frac{3 \cdot \sigma \cdot \lambda}{2 \cdot D_0} \cdot exp(\dot{\epsilon}) \tag{3.12}$$

$$Tr \propto exp(\frac{\dot{\epsilon}}{2}) \tag{3.13}$$

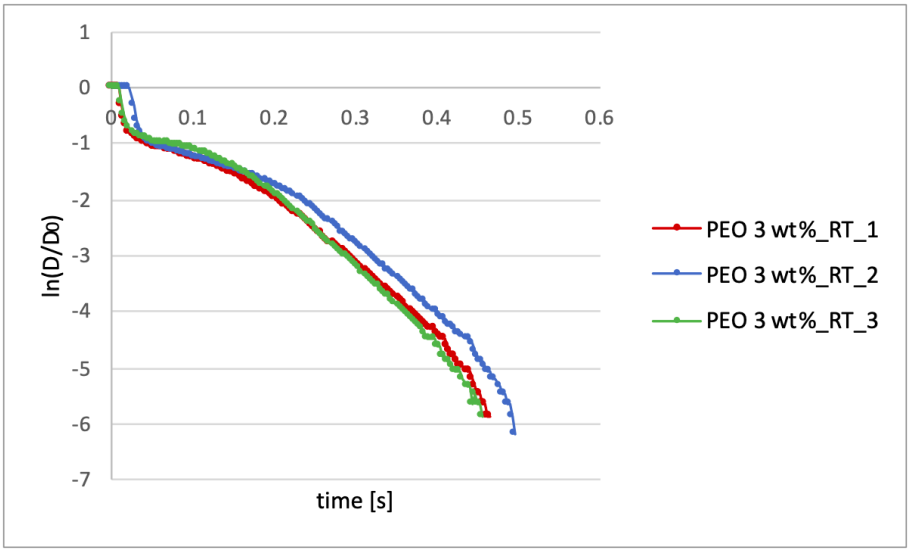

Figure 3.27: Exponential thinning of the viscoelastic PEO solution at room temperature and an endplate diameter of 4.0 mm.

Thinning behavior

The thinning-controlling velocities are plotted in Figure 3.28. The diagram illustrates the impact of the influencing factors from high to low filament ratios. Diverse to Newtonian fluids, the resistance of viscoelastic fluids against surface tension in free surface flows is also driven by elastic effects. The elastic thinning controlling velocity decreases linearly with the filament radius, which results in a constant extension rate $\dot{\epsilon}$ of the filament. Since the *Ec* number is inverse proportional to the filament diameter (Equation 1.42), also the elastocapillary number is a time-dependent value. According to this relation, the Ec number increases as the filament diameter decreases. The Ec was calculated for the CaBER experiment at room temperature and an endplate diameter of $D_P = 4.0\ mm$. The values of Ec range from $1.8 \cdot 10^{-3}$ to 0.89. As described by Clasen *et al.* (13), many

diluted polymer solutions show an *Ec* number lower than 4.7 and, thus, they are described as weak elastic fluids. The *Ec* evolution during the whole experiment is illustrated in Figure 3.28 as a function of the filament radius. The value of the shear relaxation time λ_S was calculated according to Equation 1.22. The value for the surface tension σ was taken from literature (*78*).

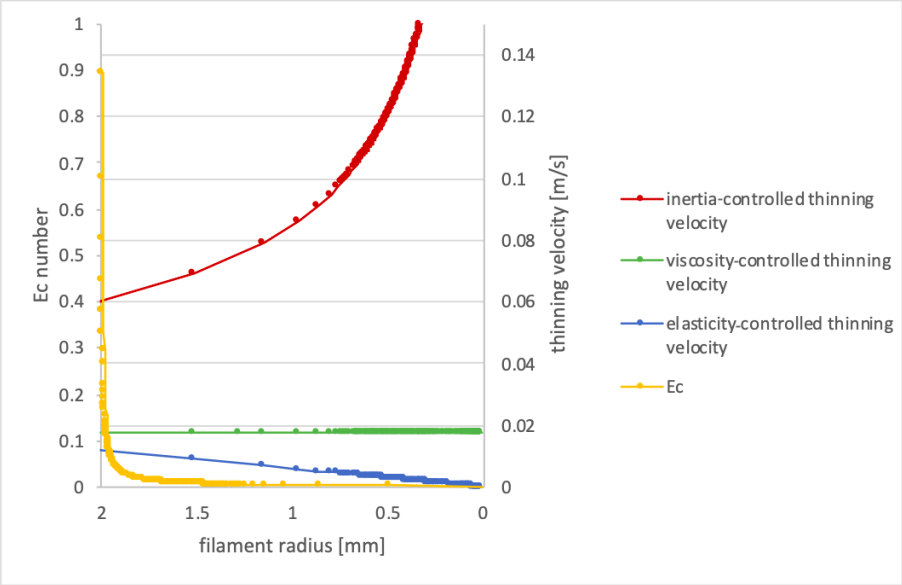

Figure 3.28: Diagram of the filament-thinning velocities over the whole experiment from large (left) to small (right) diameters of PEO. The yellow curve illustrates the time dependent elasto-capillary number.

Beads-on-a-string

The smallest measurable PEO thread diameter that can be analyzed with the image processing program ImageJ was about $D_{min} = 0.0112\ mm$. The resultant ratio between the maximum and the minimum diameter was $D/D_0 = 3.3 \cdot 10^{-3}$. This value was compared with the data from literature of $D/D_0 = 5 \cdot 10^{-3}$ found by Arnolds *et al.* (*3*). Thus, it was found that the image processing method is sensitive enough to measure small diameters of viscoelastic polymer solutions. However, occurring reflections at the filament center can cause interferences during the image processing step.

The beads-on-a-string formation is a phenomenon occurring only in viscoelastic fluids, like the PEO solution. The appeared droplets were examined by the measuring tool of the ImageJ image processing program. A droplet size distribution of

$D_{droplet} = 5.6 - 39.2 \cdot 10^{-3}\ mm$ could be found. The value for the smaller droplet diameter conforms with the reported data from literature (3).

3.2.2.2. Poly(isobutylene) SRM 2490

The thinning behavior of the SRM 2490 sample was analyzed at room-temperature and elevated temperature. The measurements are given in Figure 3.29 and Figure 3.30. Due to the fact that SRM 2490 is a standard reference material for shear measurements, the shear viscosity values at various temperatures were extracted from the NIST publication. It was found also for the non-Newtonian sample that the temperature influence on the viscosity is significant. If the temperature increases from 25 to 50 °C, the shear viscosity decreases from 98.3 to 37.5 Pa·s. This corresponds to a viscosity decrease of 60.8 Pa·s (- 62%). The effect of a decreasing viscosity in extensional measurements is expressed by a decrease of the filament lifetime and an increase of the capillary velocity. Figure 3.31 shows a direct comparison of the thinning curves at different temperatures. Additional investigations of the sample properties were carried out for PIB only at room temperature. The values for the surface tension, density, and the shear relaxation time were received from literature (13).

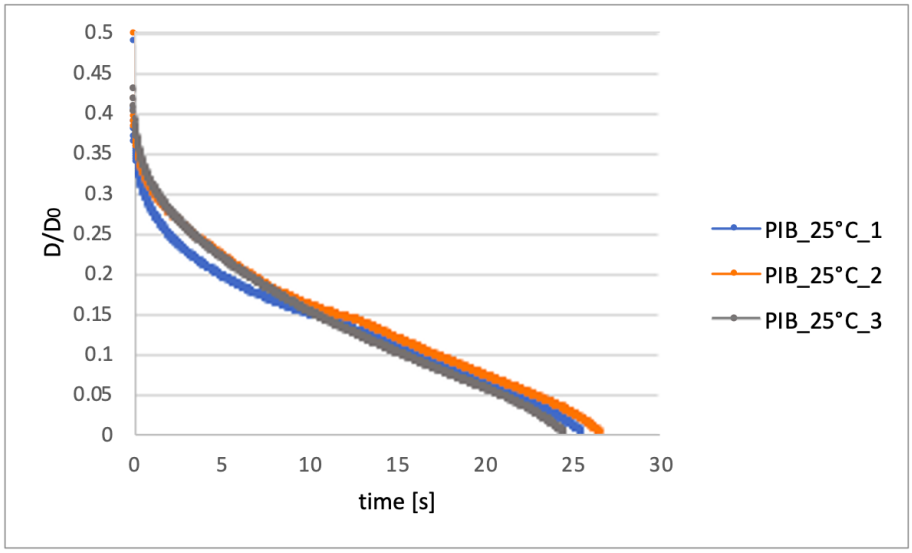

Figure 3.29: Filament thinning of PIB in decaline at room temperature.

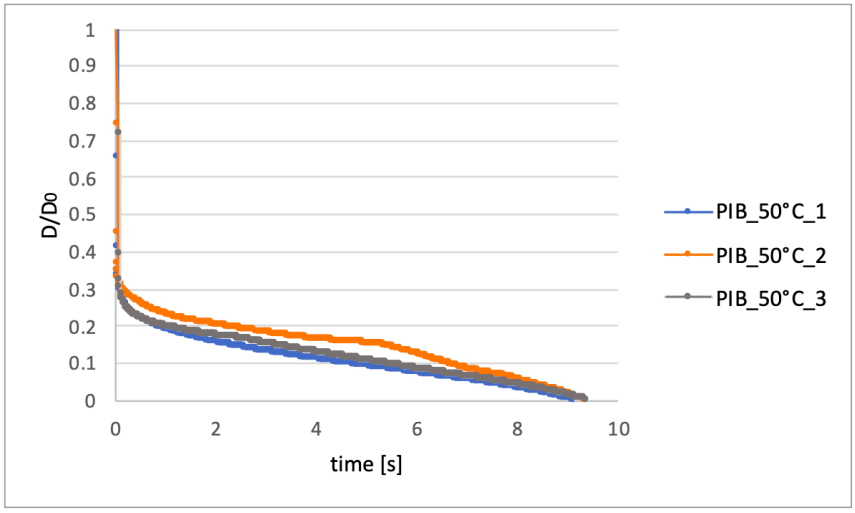

Figure 3.30: Filament thinning of PIB in decaline at 50 °C.

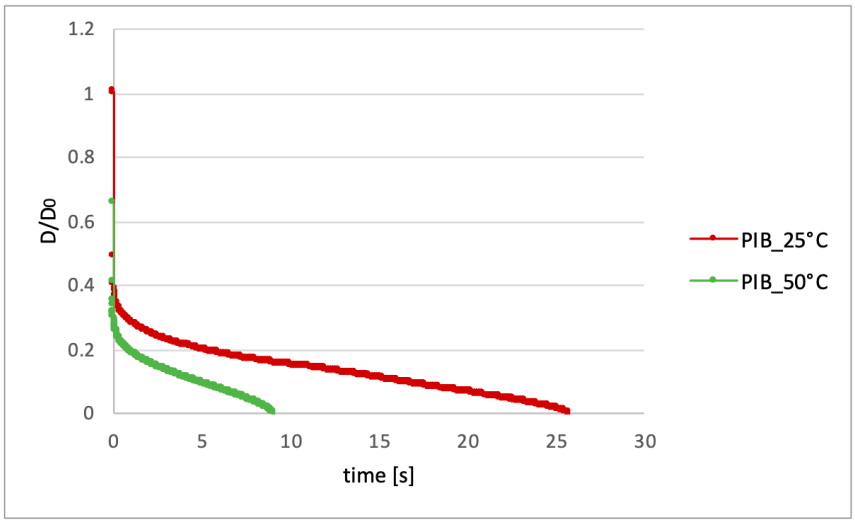

Figure 3.31: Comparison of the thinning behavior of PIB at two different temperatures.

Thinning behavior

For the estimation of the dominant thinning velocities, the inertia-, viscosity- and elasticity-controlled thinning velocities were plotted in Figure 3.32 as a function of the filament radius. From the crossover point of the inertia- and viscosity-controlled thinning velocity, an Ohnesorge number of 0.126 was calculated. At large filament diameters, viscous and elastic effects mainly drive the filament thinning process until the crossover point is reached. After $Oh < 0.126$, the thinning process is controlled by inertia effects. Furthermore, the balance of viscous and elastic effects was investigated by calculating the Ec number. During the experiment, a Ec range from 0.014 to 2.58 was found.

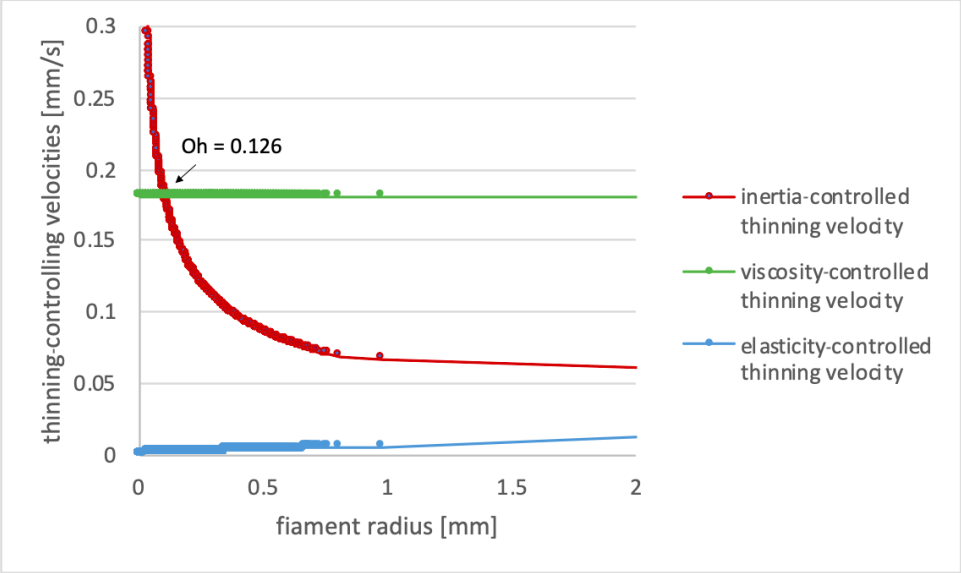

Figure 3.32: Filament thinning controlling velocities of PIB (T = 25 °C) plotted as a function of the filament radius.

The evolution of the internal numbers (*De, Oh, Ec*) during the filament thinning is reported in Figure 3.33. Based on the study by Clasen *et al.*, the PIB sample was identified as a weakly elastic fluid (Oh >> 0.2 and Ec << 4.7).(*13*) The dominant elastic effects were visible in the later region of the thinning process. In comparison to the thinning of Newtonian fluids, the sample shows a sharper decline of the thinning curve a few seconds before the break-up event. It can be assumed that this area is mainly driven by elastic effects, which leads to an uneven thread distribution. The relation between the inertia and elastic effects can be calculated by the *De* number; the obtained data range from 46.6 to 0.003. A crossover point between the viscous/elastic effects or between inertia/elastic effects (*De*) was not found. Obviously, small elastic effects play an important role for the thread-thinning over the whole experiment. Especially at the beginning and end position of the thinning curve, the elastic influence of the sample on the diameter evolution is visible (Table 3.10).

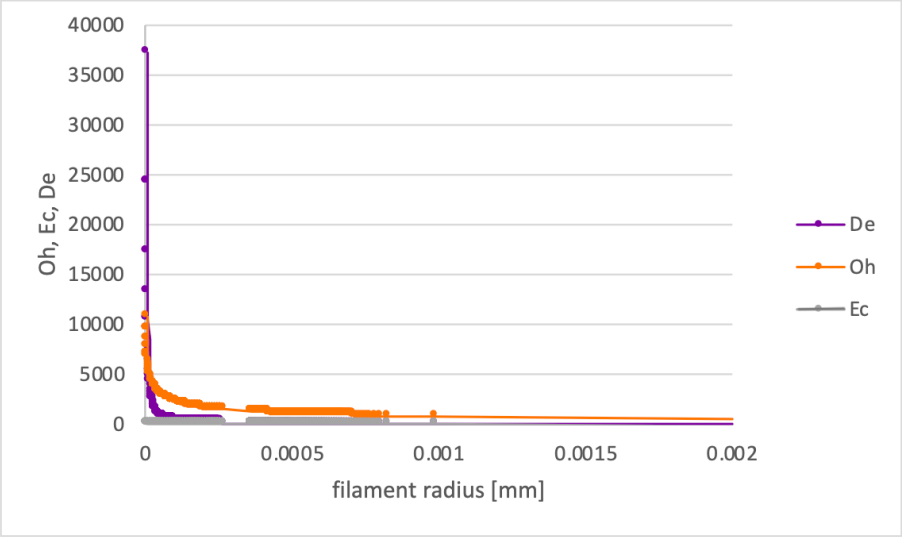

Figure 3.33: Evolution of the *De* number, *Ec* number, and *Oh* number of PIB (T = 25 °C) during the elongation experiment plotted as a function of the filament radius.

Table 3.10: List of the results from CaBER analysis of the PIB sample at room-temperature and elevated temperature.

Sample	*Temperature [°C]*	v_{cap} *[m/s]*	*SlopeD/D*$_0$ *vs time*	t_v *[s]*
SRM 2490	25	0.000049	-0.0093	25.72
SRM 2490	25	0.000066	-0.0104	21.14
SRM 2490	25	0.000063	-0.0111	20.56
SRM 2490	50	0.000091	-0.0243	9.10
SRM 2490	50	0.000078	-0.0195	9.33
SRM 2490	50	0.000091	-0.0228	9.37

3.2.2.3. Polystyrene

To analyze polystyrene samples in free surface flows, it is necessary to find the ideal temperature at which the sample behaves as a viscoelastic liquid. From thermogravimetric analysis (TGA), it is known that the decomposition of polystyrene starts at a temperature of 270 °C (*74*). Therefore, the analysis was performed in a temperature range from 100 to 250 °C. Based on the different molecular weights of the samples, the ideal temperature was investigated by trial-and-error experiments. If the temperature setting is not correct, the sample behaves like a solid, and cannot be measured in the CaBER. An example of an observed solid state behavior of PS 45,000 $g \cdot mol^{-1}$ is shown in Figure 3.34.

At this specific temperature, no filament dilution can be observed because the elastic content of the sample is too high and, thus, prevents continuous filament formation.

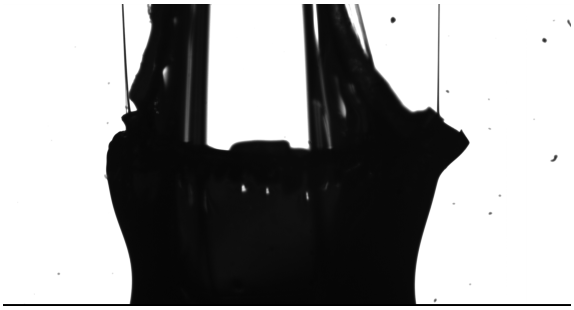

Figure 3.34: Solid behavior of PS $M_w = 45,000\ g \cdot mol^{-1}$ at a temperature of 150 °C. The lower black rectangle represents the specimen. The upper part of the picture shows some thread formations due to sticking of the sample on the upper endplate. The sample stores the deformation energy, and no further physical deformation was observed.

In order to estimate the viscous and elastic influence during the experiment, the results obtained were compared with the viscosity-controlled PDMS 5000 sample (marked green) and the elastic-controlled PIB sample (marked yellow); an overview of all examples is shown in Figure 3.35. The first line of the PS images represents the recorded pictures just before the break-up event. The second line illustrates the pictures recorded shortly after the thread break-up. PS 45,000 $g \cdot mol^{-1}$ shows the lowest amount of elastic effects at a temperature of 200 °C. The filament thinning evolves uniformly over the whole thread just like it was observed for the Newtonian PDMS 5000 sample. Obviously, the sample is characterized by the fact that it is less influenced by elastic forces. On the other hand, PS 1,200 $g \cdot mol^{-1}$ and PS 260,000 $g \cdot mol^{-1}$ resemble more the (elastic) PIB image. An uneven thread distribution was recorded with an increased sample volume at the endplates. Even after filament breakage, the liquid exhibits shape stabilization mechanisms that can be attributed to dominant elastic effects. The relaxation of the polymer molecules took much more time than with mainly viscosity-controlled thinning samples. However, one can see that the amount of elasticity-controlled thinning is different for PIB and the two PS samples. From the pictures recorded, an order from the highest to the lowest amount of elastic effects was obtained: $PIB > PS260,000 > PS1,200$. Since the temperatures during CaBER analysis cannot be set to the same value for all polymer melts,

the direct relationship between relaxation time and molecular weight cannot be clearly observed. However, from the images recorded, it can be seen that the PS with the highest molecular weight shows the greatest influence of elastic forces, especially after the break-up event.

The results obtained by image evaluation were confirmed by the calculation of v_{cap} and t_v. A summary of the calculated parameters is given in the Table 3.11, and the recorded CaBER experiments are illustrated in Figure 3.36, Figure 3.37 and Figure 3.38. For the recording of PS 1,200 $g \cdot mol^{-1}$, the lowest frame rate of 100 fps had to be set to be able to observe the entire thinning process within the time-out period of the high-speed camera. The other two samples were recorded at a frame rate of 300 fps.

Table 3.11: Summary of the results obtained from the PS melts with the CaBER set-up. Beside the experimental conditions, also the calculated capillary velocity and break-up time are given.

Sample	*Temperature [°C]*	v_{cap} *[m/s]*	*SlopeD/D$_0$ vs time*	t_v *[s]*
PS 1,200	100	$0.531 \cdot 10^{-3}$	-0.1378	2.07
PS 1,200	100	$0.605 \cdot 10^{-3}$	-0.1669	2.07
PS 1,200	100	$0.498 \cdot 10^{-3}$	-0.1339	1.98
PS 45,000	200	$0.555 \cdot 10^{-3}$	-0.1817	0.693
PS 45,000	200	$0.533 \cdot 10^{-3}$	-0.1621	0.777
PS 45,000	200	$0.632 \cdot 10^{-3}$	-0.1986	0.627
PS 260,000	250	$1.37 \cdot 10^{-3}$	-0.3318	0.193
PS 260,000	250	$0.481 \cdot 10^{-3}$	-0.2480	0.153
PS 260,000	250	$1.05 \cdot 10^{-3}$	-0.1846	0.250

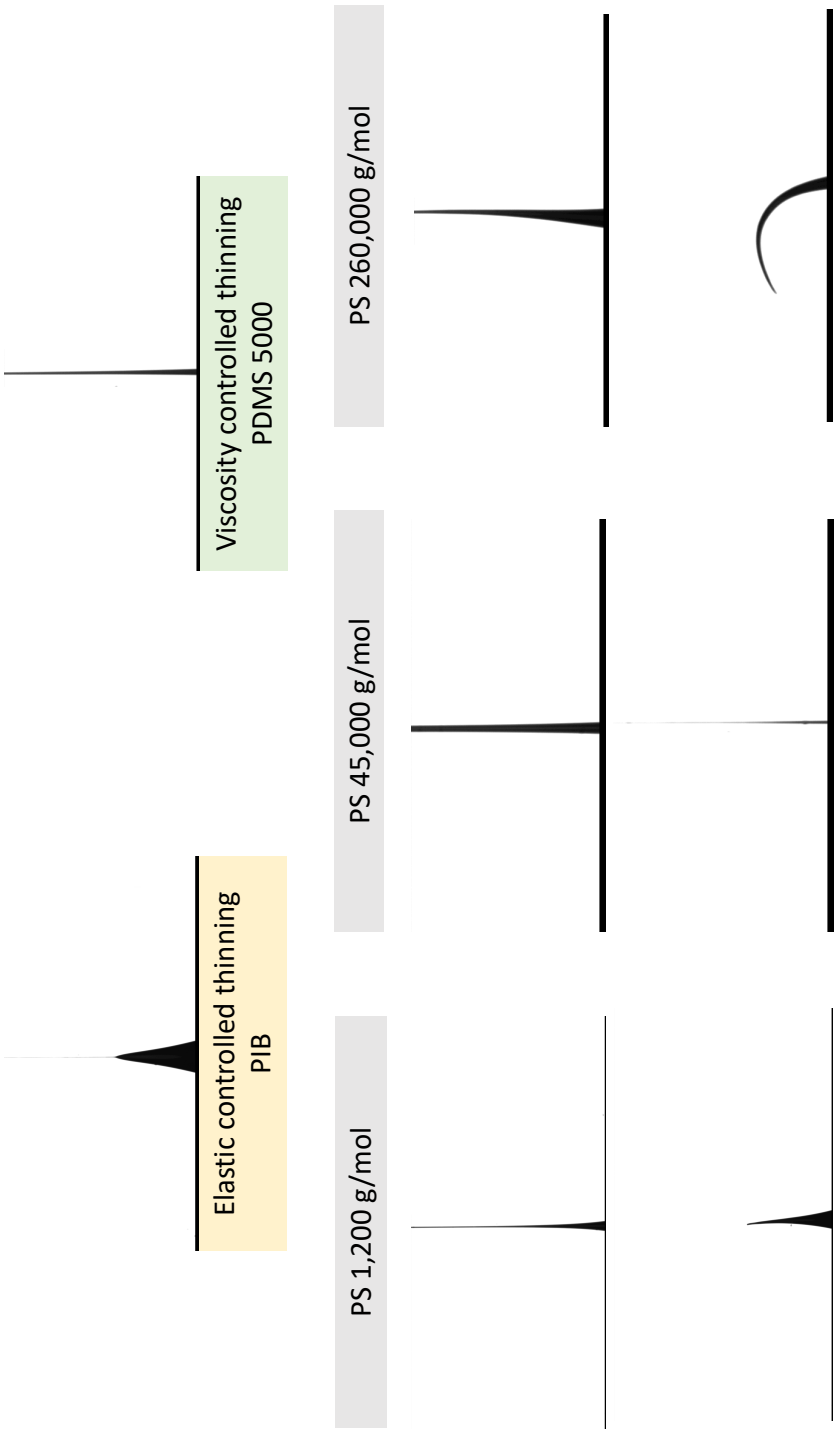

Figure 3.35: Comparison of elasticity- and viscosity-controlled thinning mechanisms of the recorded PS pictures with the pictures from PIB (yellow) and PDMS 5000 (green). The pictures illustrate the shape of the thread just before (first row) and after the break-up event (second row).

The mean thinning velocity (v_{cap}) of PS 1,200 $g \cdot mol^{-1}$ was $0.545 \cdot 10^{-3}$ m/s. For PS 45,000 $g \cdot mol^{-1}$, a v_{cap} of $0.573 \cdot 10^{-3}$ m/s was found. The PS sample with the highest molecular weight (260,000 $g \cdot mol^{-1}$) has a v_{cap} value of $0.967 \cdot 10^{-3}$ m/s. Although v_{cap} for PS 1,200 and PS 45,000 are nearly the same, they exhibit different filament lifetimes. This result is in accordance with the obtained information from the image evaluation. Elastic effects in the sample lead to an increased stabilization of the thread and, subsequently, longer lifetime. In comparison with these two samples, it was more difficult to identify the linear slope of PS 260,000 $g \cdot mol^{-1}$. Obviously, side-reactions took place during the experiment, revealed by color changes from white to yellow. As no further information on the exact composition is known, it must be assumed that the sample contains plasticizers or additives that react at this temperature. The sample showed the highest value of v_{cap} and the shortest filament lifetime, although elastic effects were proven.

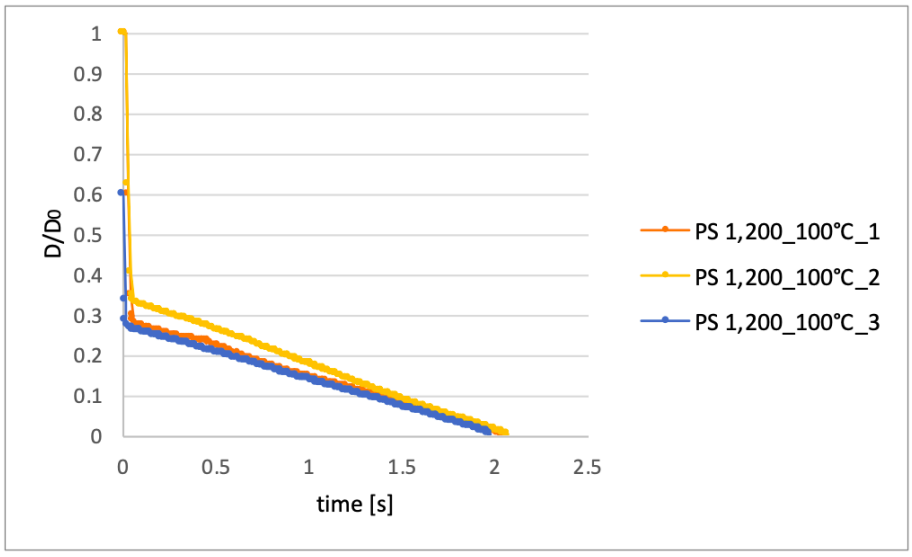

Figure 3.36: Filament thinning of PS $M_w = 1,200$ $g \cdot mol^{-1}$ at a temperature of 100 °C.

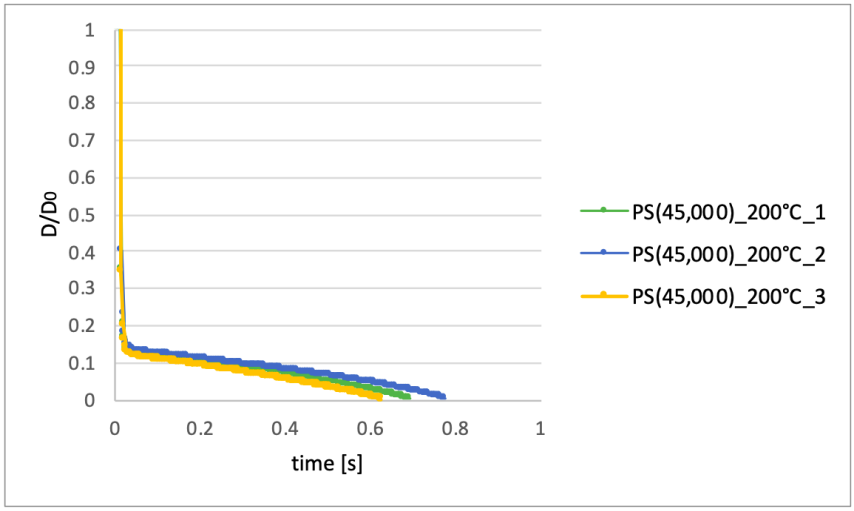

Figure 3.37: Filament thinning of PS $M_w = 45,000\ g \cdot mol^{-1}$ at a temperature of 200 °C.

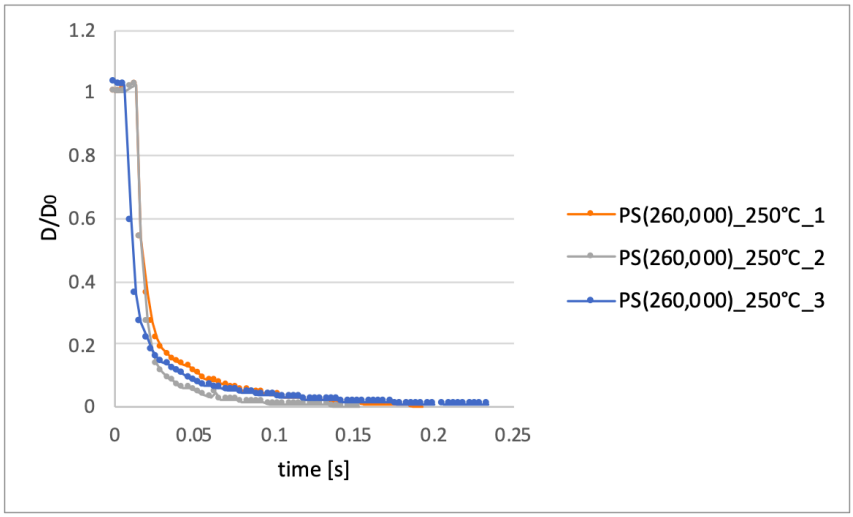

Figure 3.38: Filament thinning of PS $M_w = 260,000\ g \cdot mol^{-1}$ at a temperature of 250 °C.

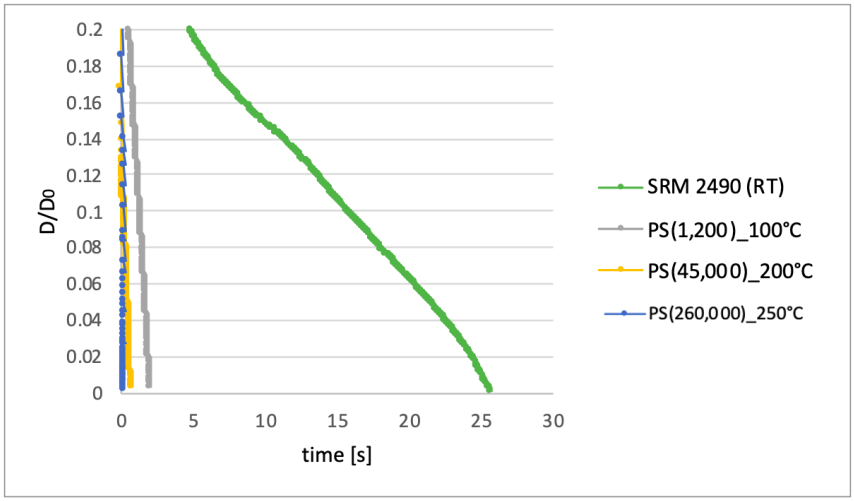

Figure 3.39: Filament thinning of all PS samples in comparison to SRM 2490.

4. Conclusion and Outlook

Motivated by the broad applicability of the CaBER measurements as well as the low sample amounts required, a modular compact rheometer (MCR) of Anton Paar GmbH was extended by an optical set-up. This set-up includes a telecentric lens, a collimator lens and a LED backlight. In addition, a high-speed camera was mounted to record the experiment. The pixel pitch of the BAUMER HXC20 high-speed camera is 5.5 μm at 2048 x 1088 pixels. This corresponds to a sensor size of 11.264 mm x 5.984 mm. With this optical extension, the recording of CaBER experiments within the CTD chamber in a limited image area of 5 x 5 mm is possible. Due to the limited field of view, not the entire test area of 9.55 mm can be displayed. Nevertheless, it was shown that it is possible to observe the thinning characteristic of Newtonian and non-Newtonian fluids. Furthermore, with the high-speed camera, a maximum frame rate of 2000 fps was achieved by reducing the imaging area. This enables the observation of fast thinning velocities of low viscosity fluids until a viscosity of 70 mPa·s.

The evaluation of the obtained image sequences was performed by an image processing program (ImageJ). On the example of the poly(ethylene oxide) solution, it was found that the smallest detectable filament diameter with the image processing diagram is 11.2 μm. In addition, a fixed evaluation position was defined in order to achieve reproducible results. As a result, it cannot be guaranteed that the smallest diameter development was observed. Furthermore, the MCR was equipped with a heating chamber, enabling the measurement of polymer melts and expanding the range of measurements.

A series of Newtonian fluids (PDMS of different molecular weights) was used to identify the parameters influencing the experiment. The expected linear dilution behavior of the Newtonian fluid was detected in all experiments carried out. The evaluation of the factors influencing the thinning velocity and the resulting break-up time was accomplished by changing the temperature, the endplate diameter, and the speed of endplate separation. As expected, the capillary velocity of

Newtonian fluids decreases with increasing temperature. The increased temperature reduces the viscosity of the sample and, consequently, its resistance against surface tension. This reveals the a clear dependency of the temperature during the CaBER measurements. Furthermore, an increase of the endplate diameter leads to a slight increase of the capillary velocity as well as to an increase of the break-up time of the low-viscosity Newtonian filament thread. This proves that the use of larger endplates is useful for low-viscosity samples, as more images of the thinning mechanism can be recorded. Thus, a more precise interpretation of the occurring mechanisms is possible. The third influencing parameter was the speed of the endplate separation. Three different separation profiles were designed with the aim to compare the advantages and disadvantages of the methods. It turned out that the advantage of a faster separation is accompanied by the disadvantage of further vibrations of the endplate and the filament thread. The investigations showed that, both the non-damped step displacement and the damped step displacement, require almost the same amount of time ($\sim$ 60 ms) to reach a stable end position. In conclusion, the damped step endplate separation profile was used for all experiments, as side-reactions due to filament oscillations can be avoided.

Beside the linear thinning of Newtonian fluids, also the exponential thinning of viscoelastic fluids was investigated. A 3 $wt\%$ PEO (10^6 $g \cdot mol^{-1}$) solution was prepared. The thinning mechanism as well as the characteristic beads-on-a-string formation were analyzed by the new designed elongation device. It could be shown that the sample is extremely sensitive to external influences, such as the air flow in the chamber. Although exponential thinning was observed in all experiments, small variations in concentration and temperature caused large changes in the flow relaxation time. Thus, it was shown that it is necessary to perform the experiment at least three times in order to obtain representative results. Furthermore, it has been proven that ImageJ is able to analyze and determine occurring effects like bead formation. The analytical method enables the detection of droplet sizes from 5.6 mm to $39.2 \cdot 10^{-3}$ mm and fits well into the given literature values of PEO.

More concentrated viscoelastic liquids such as PIB in decaline or PS melts no longer show exponential thinning. The middle part of the thinning curve follows a linear decrease and allows the calculation of a capillary velocity. Instead, the beginning and end of the thinning curve show thread stabilization mechanisms resulting from additional elastic forces in the sample. Depending on the amount of elasticity, different stabilization intensities were visible especially at the snapshot just after the break-up event. As for PEO, the CaBER experiment with PS melts showed the importance of repeating the experiment in triplicate. In summary, it was demonstrated that the analysis of polymer solutions and melts is possible with the newly developed CaBER device. The values obtained are consistent with the literature references and the results based on the theory.

The high-temperature CaBER analysis method is an important tool for quick and easy measurement of polymer melts under free surface flows. However, in order to identify all instability mechanisms, it is necessary to extend the field of view to 10 x 10 mm. By covering the entire experimental field, finding the smallest thinning area is much easier and, in addition, interferences like gravitational sagging at the endplates can be observed and quantified. In addition to improving the equipment, further development work on the rheocompass software is also necessary. Further improvements to the software are required to generate rapid changes in endplate position and subsequent Hencky strain. The analysis of the PEO showed the importance of additional work on the temperature control of the chamber. Since the CTD 600 itself is not able to reach temperatures below room temperature, it is necessary to cool down the temperature by an external convective air flow. The drying processes caused by the external air flow could be reduced by humidifying the air flow or by designing a sample protection device.

After a successful improvement of the device and sample preparation, further steps of the CaBER technology can be considered. Due to the fact that the MCR is originally designed for shear analysis, both measuring techniques could be combined with the aim of obtaining more information about the behavior of polymers. According to the state-of-the-art, no other commercial device is

capable of combining both technologies. The measurement could be carried out without additional exchange of the measuring system or unwanted heat losses. In addition to the combination of technologies, it is also possible to extend and improve the CaBER analysis itself. Especially the possibility of the CTD chamber for measurements at high temperatures opens new fields of application. In the current state, only measurements of diluted polymer solutions and measurements up to 80 °C were possible. The newly designed CaBER in combination with the CTD chamber and the linear drive allows measurements up to 600 °C. Thus, not only polymer solutions, but also materials with high melting points can be analyzed.

5. Abstract

The present master thesis details the development and evaluation of a high-temperature capillary break-up extensional rheometer (CaBER). The device enables the measurement of polymer melts under free surface flows. Other commercially availably measurement systems, like shear rheometers are not able to quantify extensional behavior. Thus, the newly developed high-temperature CaBER offers a new method for the understanding of polymer behavior during different production steps with inherent extensional processes. Additionally, costs and time can be saved in industrial processing steps. In this study, the CaBER was developed on the basis of a MCR rheometer and a CTD 600 chamber from Anton Paar GmbH.

Firstly, a literature research on comparable measurement systems was performed in order to identify the set-up parts of the CaBER. Secondly, first prototypes were developed and the results found and the suffered set-backs were evaluated. After the first successful test series, the suitability of the device for CaBER measurements was evidenced by standard Newtonian and non-Newtonian fluids, like poly(dimethyl siloxane) (PDMS) and aqueous solution of poly(ethylene oxide) (PEO). Based on different thinning mechanisms and the underling thinning controlling forces, different results and phenomena were found for PDMS and PEO. Especially, the 'beads-on-a-string-formation' of viscoelastic fluids was examined. Furthermore, other influencing parameters like endplate diameter, temperature and endplate separation speed were examined. Finally, polystyrene melts were analyzed in a temperature range of 100 to 250 °C. The sample processing method of the three different molecular weight samples was evaluated. The subsequently aquired data from the CaBER measurement were compared with the standard reference material, namely poly(isobutylene) dissolved in decaline (SRM 2490). The standard reference material was accurately examined in shear rheological measurements by the 'National Institute of Standards and Technology' (NIST) in 2001. At room temperature, the shear rheological measurement of the fluid showed a similar behavior to polymer melts.

In summary, it was found that this newly developed device is capable of monitoring the different thinning mechanisms of Newtonian and non-Newtonian fluids. Furthermore, it was evidenced that CaBER measurements of polymer melts offer important information about the molecular weight and the molecular weight distribution.

6. Zusammenfassung

Die vorliegende Masterarbeit zeigt die Entwicklung und Evaluierung eines Hochtemperatur-Dehnrheometers. Das Rheometer soll auf der Grundlage von kapillarer Abbruch-Dehnrheologie (CaBER) die Messung von niedrig-viskosen Polymerschmelzen in freien Oberflächenströmungen erlauben. Mithilfe dieser Untersuchungsmethode sollen dehnrheologische Effekte während der Polymerverarbeitung besser verstanden und Produktionsschritte optimiert werden. Da bereits kommerziell erhältliche Messgeräte nicht in der Lage sind, Prozesse während starker Dehnströmungen vorherzusagen, kann das neu entwickelte Gerät signifikante Verbesserungen im Zeit- und Kostenmanagement ermöglichen. In dieser Studie wurde ein MCR 702 Rheometer mit unterem Linearmotor und eine CTD 600 Kammer von der Firma Anton Paar GmbH als Basiseinheit verwendet. Der erste Teil der Arbeit beschäftigt sich mit der Literaturrecherche zu vergleichbaren Messgeräten und Messmethoden. Anschließend werden erste Prototypen und gewonnene Erkenntnisse für weitere Optimierungen geschildert. Nach erfolgreichem Abschluss erster Testreihen wurden das Hochtemperatur-Rheometer mit standardisierten Newtonschen und nicht-Newtonschen Fluiden, wie Poly(dimethyl siloxan) (PDMS) und wässrigen Lösungen des Poly(ethylenoxid) (PEO) auf potentielle Anwendungen evaluiert. Da die Filament-Einschnürung in Newtonschen und viskoelastischen Fluiden von unterschiedlichen Kräften bestimmt wird, können probenspezifische Phänomene evaluiert und untersucht werden. Besonders auffällig ist die 'Perlen-auf-einer-Schnur' Formation bei viskoelastischen Fluiden. Neben der Untersuchung von Einschnürungsmechanismen und Abbruchzeiten wurden auch Einflussparameter wie unterschiedliche Endplattendurchmesser, Temperatur und Trenngeschwindigkeit untersucht. Als letzter Schritt erfolgte die Hochtemperaturmessung von Polystyrol-Schmelzen. Basierend auf der Zersetzungstemperatur des Polymers wurde ein Temperaturbereich von 100 bis 250 °C gewählt. Die Auswertung der gewonnen Daten erfolge durch den Vergleich mit einem standardisiertem Referenzmaterial (SRM 2490). Das SMR wurde im Jahre 2001 vom 'National Institute of Standards and

Technology' (NIST) ausführlich unter scherrheologischen Messungen untersucht und zeigt bei Untersuchungen bei Raumtemperatur ein polymerschmelzen-ähnliches Verhalten. Die literaturbekannten Daten wurden zur Berechnung von den auf die Probe wirkenden Kräfte während der CaBER-Messung verwendet. Zusammenfassend konnten Unterschiede in der Einschnürung und Abbruchzeit für alle Proben nachgewiesen werden. Die gefunden Unterschiede können auf die unterschiedliche Probenzusammensetzung und die damit einhergehende Viskosität zurückgeführt werden.

7. Acknowledgement

I would like to take the opportunity to thank everybody who supported and motivated me during the completion of my master's thesis. The valuable cooperation between the Polymer Competence Center Leoben GmbH, the Graz University of Technology, and the company Anton Paar GmbH enabled me to complete my studies successfully.

First of all, I would like to thank Priv.-Doz.Dr. Frank Wiesbrock, who supervised and assessed my master's thesis. I would like to thank him for his helpful suggestions and constructive criticism during the preparation of this thesis.

I would also like to thank my colleagues at the Anton Paar GmbH, who provided me with the working equipment as well as access to technical literature and internal reports. I would also like to express my gratitude for the good cooperation within the company and the technical staff. Last but not least, I am grateful for suggestions and ideas from all the people involved that have pushed the project forward and improved it. Furthermore, I would like to thank my colleagues and supervisors, Dr.techn. Wolfgang Baumgartner, Dr.mont. Matthias Walluch and Dipl.-Ing. Alexander Troiss, who supported me during the research and always had an open ear for questions. I would also like to thank all my other colleagues for welcoming me with open arms and creating a pleasant working atmosphere.

I would especially like to thank my friends Anna Stark and Carmen Oberjakober for their strong emotional support throughout my studies. Finally, I would like to thank my parents, who made my studies possible with their support and supported me in all my decisions.

8. Experimental

8.1. Materials

Poly(dimethyl siloxane) PDMS with viscosities of 5 mPa·s and 5,000 mPa·s were supplied by Bluestar Silicones. The PDMS viscosity standard was purchased from AMETEK Brookfield. It has a viscosity of 100 mPa·s with an accuracy of ± 1%. The poly(ethylene oxide) sample PEO was supplied by Sigma-Aldrich, and the polystyrene pellets were provided by Scientific Polymer Products. The poly(isobutylene) PIB sample (SRM 2490) preparation were performed according to the SRM 2490 NIST special publication (*75*).

8.2. Instrumentation

8.2.1. Settings for Gel-Permeation Chromatography

PDMS 5000

Gel-Permeation Chromatography (GPC) is one of the most powerful techniques for the characterization of the disperisty of polymers.(*79*) The principle of the GPC measurements is the separation of molecules according to their hydrodynamic volume. During analysis, the degree of purity and the molecular weight distribution of all PDMS samples was determined. The samples were dissolved in THF. 112.0 μL of the dissolved samples were placed at the column. The flow rate of the eluent (THF) was adjusted at 1000 mL/min, and the duration of the measurement was 30 min. Due to the low viscosity of PDMS 5, the GPC measurement was impossible. GPC analyses with a Merck Hitachi L-6000 A pimp a column of Polymer Standard Solutions (8/300 mm S TV linear XL 5 μm grade size), and differential refractometer Walters 410 detector.

8.2.2. Settings for Shear Rheology

PDMS 5000

From literature, it is well known that the viscosity is dependent on the temperature; significant viscosity changes are possible at just small temperature changes. For the shear rheological measurements, a MCR 702 rheometer was used with a heating and cooling element at the bottom (P-PTD200/56). The rotational measurements were performed with a cone-plate (CP50.2; α= 2.003 °), and a shear rate from 0 to 100 [1/s]. To avoid the formation of temperature gradients, a hood (H-PTD200) was mounted at the sample. To avoid measuring errors, the mechanical inertia was measured without a loaded sample. Afterwards, PDMS 5000 was analyzed at 20, 25, 50 and 100 °C. Each measurement was performed three times. A new sample was loaded if a new temperature was set. It was shown that sample preparation and the trimming process have a major impact on the measurement results. The repetitive measurement of a single sample can significantly reduce the risk of measurement errors and thus improve reproducibility.

PEO and PIB solutions

The high-viscous polymer PEO solutions were analyzed by a MCR rheometer from Anton Paar. As with the silicone oil measurements, a heating and cooling device (P-PTD200/56) was also used for measuring PEO. A plate-plate system was used with an endplate diameter of 25 mm (PP25.1). The amplitude sweep of PEO was performed at an angular frequency of 6.28 rad/s and a temperature of 20 °C. The frequency sweep was performed at a constant shear strain γ of 10%. The angular frequency region was set from 314 rad/s to 0.0628 rad/s. The settings for the PIB solutions for the amplitude sweep were an angular frequency of 6.28 rad/s and a temperature of 25 °C. The frequency sweeps were also performed at a temperature of 25 °C and a shear strain γ of 10%. The angular frequency was recorded from 628 rad/s to 0.01 rad/s.

PS

The polymer melts were analyzed by a 502 MCR rheometer with an additional electrical temperature device (H-ETD 400). Initially, the linear viscoelastic region was determined by amplitude sweep measurements. For all samples, a shear rate of 10% was set for the subsequent frequency sweep measurements. The PS 260,000 $g \cdot mol^{-1}$ sample showed a higher viscosity compared to the other samples. Due to the higher molecular weight, PP50.2 with a gap of 0.204 mm was used as measuring system for PS 260,000 $g \cdot mol^{-1}$ melt. The other PS melts were analyzed with a larger plate system.

8.3. Development of the device

The capillary thinning experiments (CaBER) were carried out using the air-bearing-based modular compact rheometer (MCR) from the Anton Paar GmbH (Graz, Austria) with an additional lower linear drive and convection temperature device (CTD). The CTD chamber was equipped with an optical set-up containing a Telecentric SilverTL^{TM}-Objective TECHSPEC (Edmund Optics, Mainz, Germany) with a magnification of 2.0 and a high-speed camera from Baumer GmbH (Germany, Friedberg). In this study, endplate diameters of $D_P = 4mm$, $D_P = 6mm$, and $D_P = 8mm$ were used. For the endplates of 4 and 8 mm, measuring systems (PP04; PP08) from Anton Paar GmbH were used. For $D_P = 6mm$, a measuring shaft with detachable plates was applied. More detailed information about the development of the high temperature CaBER device are given in section 2.1.

List of Figures

List of Tables

List of Abbreviations

A Shear area

b Bond length

Bo Bond number

c^* Saturated concentration

c_e Entanglement concentration

CaBER Capillary break-up extensional rheology

CTD Convection temperature device

De Deborah number

D_{mid} Midpoint diameter

D_P Endplate diameter

Ec Elasto-capillary number

F Shear force

F_{el} Electric force

FiSER Filament stretch rheometer

F_z Surface tension force

G′ Storage modulus

G″ Loss modulus

H Enthalpy

h_0 Initial endplate separation

h_f Final endplate separation

k_B Boltzmann constant

l_{cap} Capillary lenght

LVE Linear-viscoelastic region

MCR Modular compact rheometer

N Number of free lattice sites

Oh Ohnesorge number

PAM Poly(acrylamide)

PEO Poly(ethylene oxide)

PDMS Poly(dimethyl siloxane)

PIB Poly(isobutylene)

PS Polystyrene

r End-to-end distance

S Entropy

s Radius of gyration

Tr Trouton ratio

t_R Rayleigh time scale

t_v Viscous time for break-up

U Potential energy

V_η Viscosity controlled thinning velocity

V_λ Elastic controlled thinning velocity

V_ρ Interia controlled thinning velocity

γ Shear strain

$\dot{\gamma}$ Shear rate

ϵ Hencky strain

$\dot{\epsilon}$ Rate of extension

η Viscosity

η_{app} Apparent viscosity

η_E Extensional viscosity

η_S Shear viscosity

λ_E Relaxation time

λ_S Shear relaxation time

μ Chemical potential

ν Kinematic viscosity

ρ	Density
σ	Surface tension
τ	Shear stress
ϕ	Deflection angle
ω	Angular frequency

Appendix A.

Technical Specifications

Table A.1: List of the device specifications of the MCR 702 MultiDrive.

Parameter	Specification	Unit
Maximum force	40	N
Minimum force	0.0005	N
Maximum walk	9400	μm
Minimum walk	0.01	μm
Maximum frequency	100	Hz
Minimum frequency	0.001	Hz
Maximum temperature	600	°C
Minimum temperature	-160	°C
Maximum heating rate	35	K/min
Minimum heating rate	30	K/min
Maximum torsional moment	230	mNm
Minimum rotational moment	1	nNm
Minimum moment of oscillation	0.5	nNm
Angle excursion	0.05 - ∞	μrad
Minimum angular speed	10^{-9}	rad/s
Maximum angular speed	314	rad/s
Maximum angular frequency	10^{-7}	rad/s
Minimum angular frequency	628	rad/s
Normal force range	0.005 - 50	N

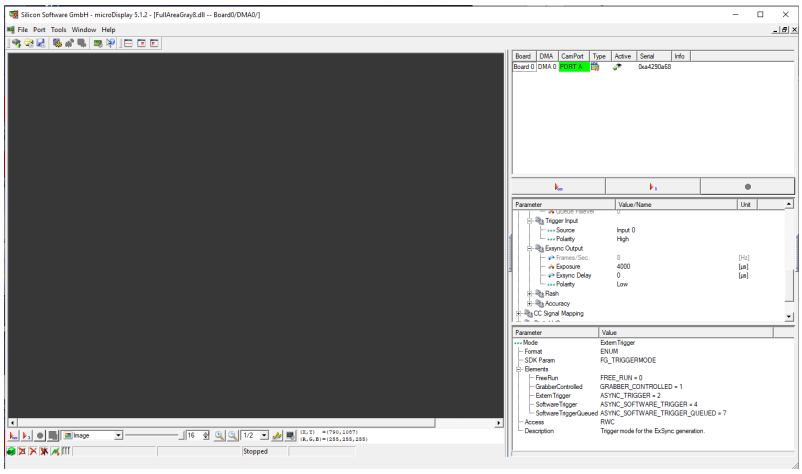

Figure A.1: Silicon software-micro display: Specification of the high-speed camera for the frequency generator (Aligent).

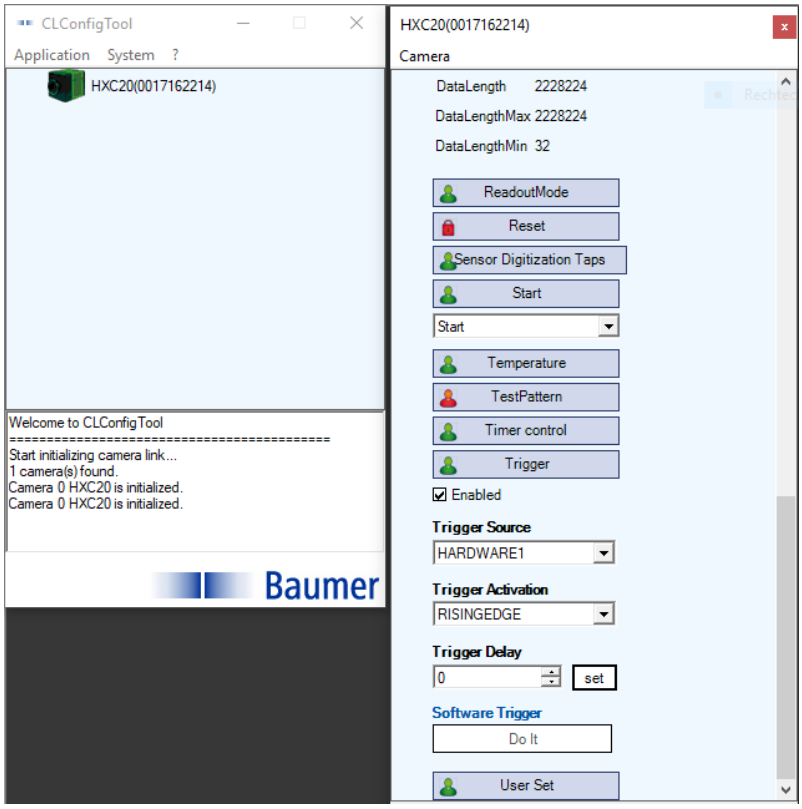

Figure A.2: CL ConfigTool specifications of the BAUMER high-speed camera for the usage of the frequency generator.

Figure A.3: Connection point of the MCR 702 to the frequency generator.

Figure A.4: Connection point of the frequency generator to the high-speed camera.

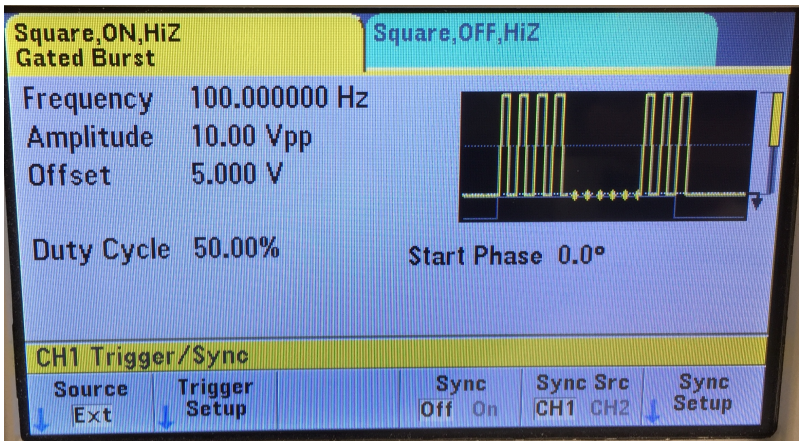

Figure A.5: Specification of the frequency generator. At a voltage setting of 5 V, the camera starts recording pictures and stops at a signal of 0 V.

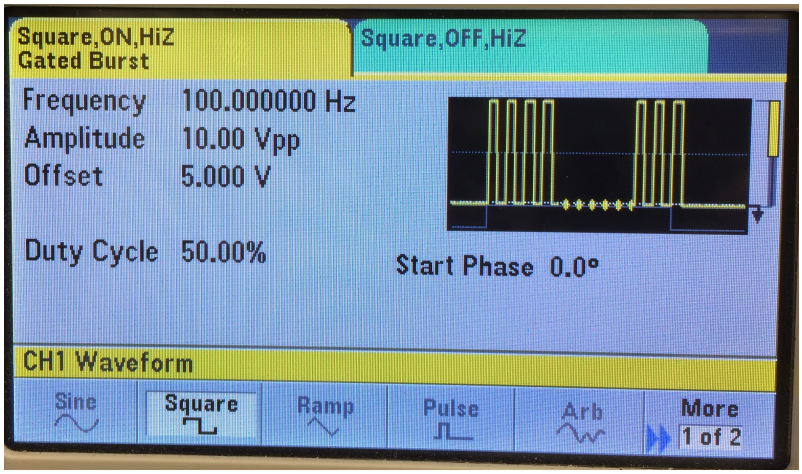

Figure A.6: Specification of the frequency generator.

Appendix B.

Additional Measurements

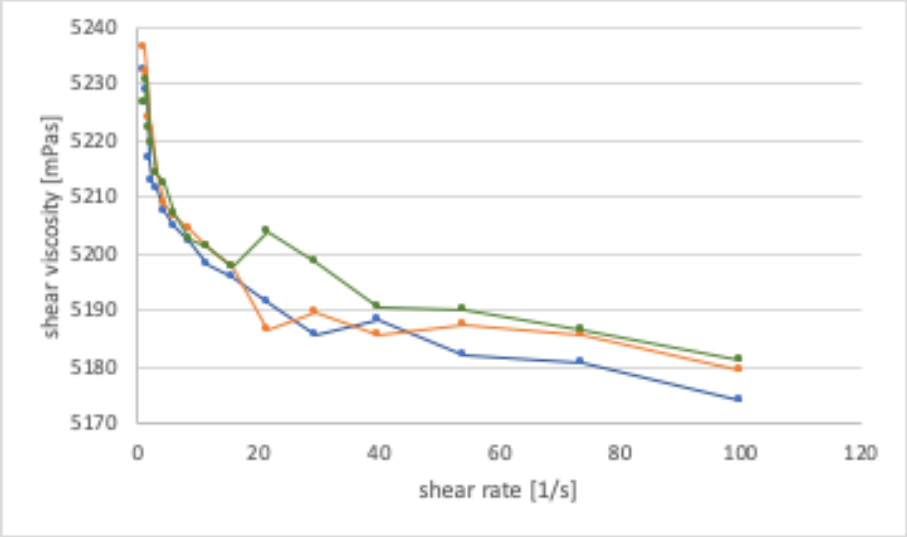

Figure B.1: Rotational shear analysis of PDMS 5000 (T= 25 °C).

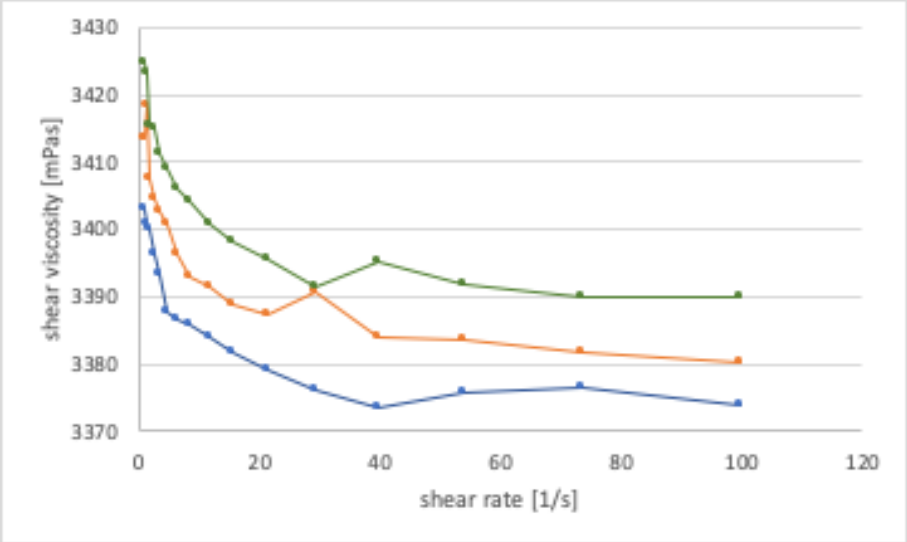

Figure B.2: Rotational shear analysis of PDMS 5000 (T= 50 °C).

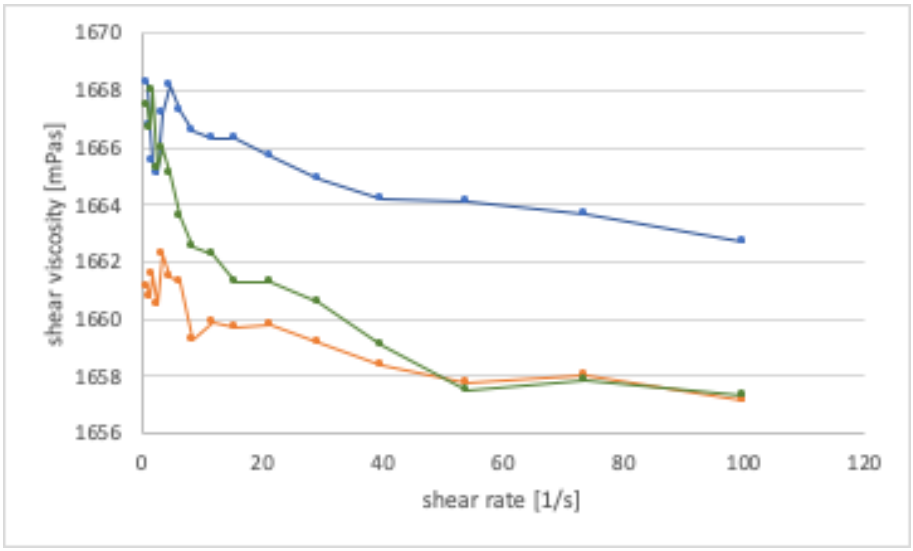

Figure B.3: Rotational shear analysis of PDMS 5000 (T= 100 °C).

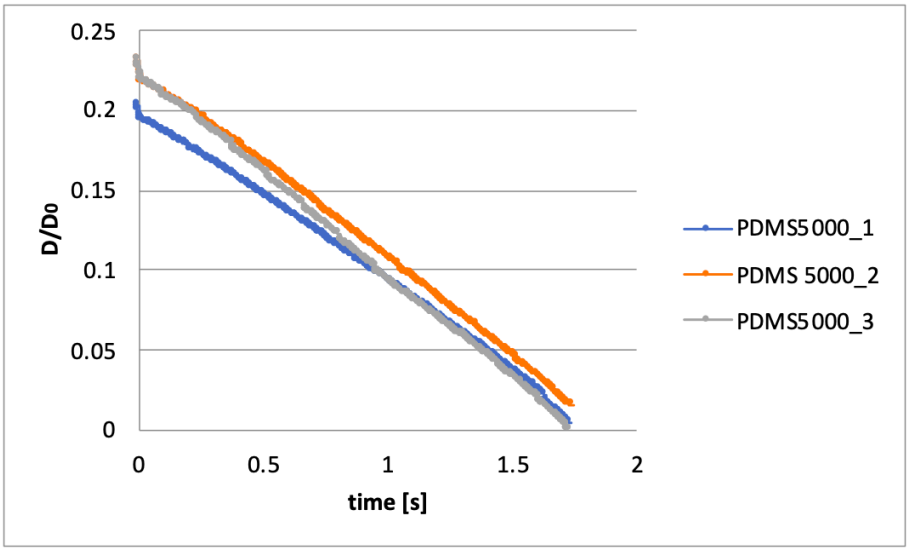

Figure B.4: CaBER analysis of PDMS 5000 (T= 20 °C).

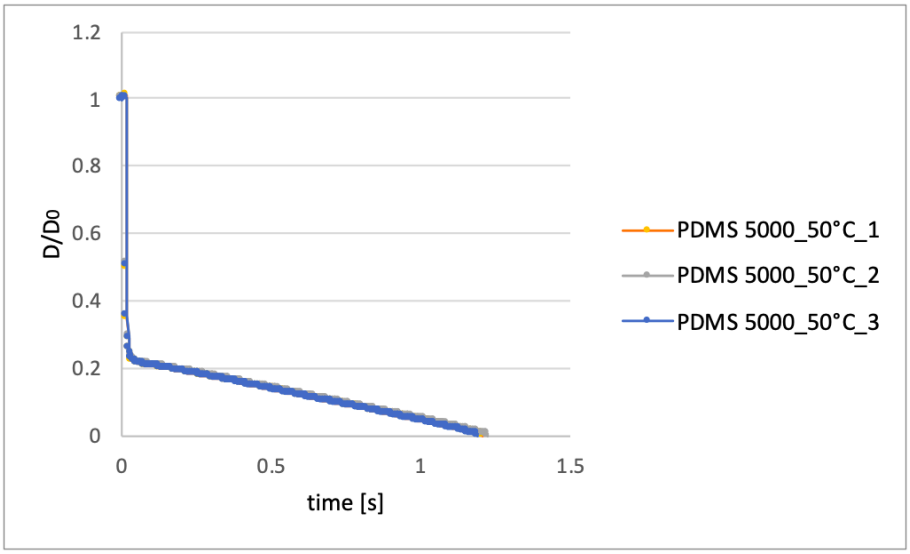

Figure B.5: CaBER analysis of PDMS 5000 (T= 50 °C).

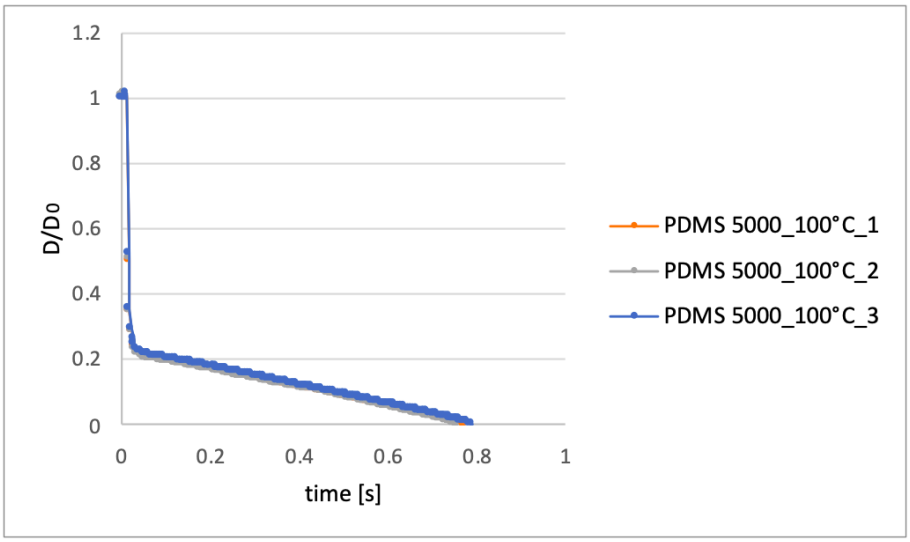

Figure B.6: CaBER analysis of PDMS 5000 (T= 100 °C).

Bibliography

(1) Odell, J., and Carrington, S., (2006). Extensional flow oscillatory rheometry. *Journal of non-Newtonian Fluid Mechanics 137*, 110–120 (cit. on pp. iii, iv).

(2) McKinley, G. H., and Sridhar, T., (2002). Filament-Stretching Rheometry of Complex Fluids. *Annual Review of Fluid Mechanics 34*, 375–415 (cit. on pp. iii, 14, 15, 17, 19, 27, 28).

(3) Arnolds, O., Buggisch, H., Sachsenheimer, D., and Willenbacher, N., (2010). Capillary breakup extensional rheometry (CaBER) on semi-dilute and concentrated polyethyleneoxide (PEO) solutions. *Rheologica Acta 49*, 1207–1217 (cit. on pp. iii, iv, 19, 27, 39, 44, 61, 66, 88, 89, 94, 95).

(4) Miller, E., Clasen, C., and Rothstein, J. P., (2009). The effect of step-stretch parameters on capillary breakup extensional rheology (CaBER) measurements. *Rheologica Acta 48*, 625–639 (cit. on pp. iii, 19, 24, 25, 29, 30).

(5) Mezger, T., *Angewandte Rheologie: Mit Joe Flow auf der Rheologie-Straße*; Anton Paar GmbH, Austria: 2018 (cit. on pp. iii, 7–13, 19, 20).

(6) Vadodaria, S. S., and English, R. J., (2016). Extensional rheometry of cellulose ether solutions: flow instability. *Cellulose 23*, 339–355 (cit. on pp. iii, 17, 22, 25, 26).

(7) (visited on 09.12.2020)., `http://www.rheologysolutions.com/thermo-scientific-haake-caber-1/` (cit. on p. iii).

(8) McKinley, G. H., and Tripathi, A., (2000). How to extract the Newtonian viscosity from capillary breakup measurements in a filament rheometer. *Journal of Rheology 44*, 653–670 (cit. on pp. iii, 17, 20, 21, 24, 59).

(9) Clasen, C., (2010). Capillary breakup extensional rheometry of semi-dilute polymer solutions. *Korea-Australia Rheology Journal 22*, 331–338 (cit. on pp. iii, 17).

(*10*) Anna, S. L., McKinley, G. H., Nguyen, D. A., Sridhar, T., Muller, S. J., Huang, J., and James, D. F., (2001). An interlaboratory comparison of measurements from filament-stretching rheometers using common test fluids. *Journal of Rheology 45*, 83–114 (cit. on pp. iii, 14, 16, 17, 21).

(*11*) Galindo-Rosales, F. J., Alves, M., and Oliveira, M. S., (2013). Microdevices for extensional rheometry of low viscosity elastic liquids: a review. *Microfluidics and Nanofluidics 14*, 1–19 (cit. on pp. iii, iv, 14, 15, 19, 27).

(*12*) Rodd, L. E., Scott, T. P., Cooper-White, J. J., and McKinley, G. H., (2005). Capillary break-up rheometry of low-viscosity elastic fluids. *Applied Rheology 15*, 12–27 (cit. on pp. iii, 14, 17, 22, 23, 25, 27, 39, 49, 66, 74).

(*13*) Clasen, C., Phillips, P. M., Palangetic, L., Vermant, and Jan, (2012). Dispensing of rheologically complex fluids: the map of misery. *AIChE Journal 58*, 3242–3255 (cit. on pp. iv, 23–26, 31, 59, 62, 93, 95, 97).

(*14*) Lagnado, R., and Leal, L. i., (1990). Visualization of three-dimensional flow in a four-roll mill. *Experiments in Fluids 9*, 25–32 (cit. on p. iv).

(*15*) Teegarden, D. M., *Polymer Chemistry: Introduction to an Indispensable Science*; NSTA Press, Virginia: 2004 (cit. on p. 1).

(*16*) Shrivastava, A., *Introduction to Plastics Engineering*; William Andrew, Cambridge: 2018 (cit. on p. 1).

(*17*) Lechner, M. D., Gehrke, K., Nordmeier, E. H., and Guhr, U., *Makromolekulare Chemie*; Springer, Basel: 2003 (cit. on pp. 2, 4).

(*18*) Münstedt, H., and Schwarzl, F. R., *Deformation and Flow of Polymeric Materials*; Springer, Berlin Heidelberg: 2014 (cit. on pp. 2–4, 19, 20).

(*19*) Girifalco, L. A., *Statistical Mechanics of Solids*; OUP USA, NewYork: 2003; Vol. 58 (cit. on p. 2).

(*20*) Baughman, D. R., and Liu, Y. A., *Neural Networks in Bioprocessing and Chemical Engineering*; Academic Press, London: 2014 (cit. on p. 5).

(*21*) de Gennes, P.-G., (1971). Reptation of a polymer chain in the presence of fixed obstacles. *The journal of chemical physics 55*, 572–579 (cit. on pp. 5, 6).

(22) De Gennes, P.-G., and Gennes, P.-G., *Scaling Concepts in Polymer Physics*; Cornell University Press, Ithaca: 1979 (cit. on p. 6).

(23) (visited on 04.10.2020)., http://polymerdatabase.com/polymer%20physics/Reptation.html (cit. on p. 6).

(24) Mezger, T., *The Rheology Handbook: For Users of Rotational and Oscillatory Rheometers*; European Coatings, Hanover: 2020 (cit. on pp. 7, 8).

(25) Shenoy, A. V., *Rheology of Filled Polymer Systems*; Springer Science & Business Media, Netherlands: 2013 (cit. on p. 7).

(26) Viswanath, D. S., Ghosh, T. K., Prasad, D. H., Dutt, N. V., and Rani, K. Y., *Viscosity of Liquids: Theory, Estimation, Experiment, and Data*; Springer Science & Business Media, Netherlands: 2007 (cit. on p. 7).

(27) Chen, Y., Zhou, Y., Pi, H., and Zeng, G., (2019). Controlling the shear thickening behavior of suspensions by changing the surface properties of dispersed microspheres. *RSC Advances 9*, 3469–3478 (cit. on p. 11).

(28) Yu, M., Qiao, X., Dong, X., and Sun, K., (2018). Shear thickening effect of the suspensions of silica nanoparticles in PEG with different particle size, concentration, and shear. *Colloid and Polymer Science 296*, 1119–1126 (cit. on p. 11).

(29) Rodrıguez-Rivero, C., Hilliou, L., del Valle, E. M. M., and Galán, M. A., (2014). Rheological characterization of commercial highly viscous alginate solutions in shear and extensional flows. *Rheologica Acta 53*, 559–570 (cit. on p. 13).

(30) Niedzwiedz, K., Arnolds, O., Willenbacher, N., and Brummer, R., (2009). How to characterize yield stress fluids with capillary breakup extensional rheometry (CaBER)? *Applied Rheology 19*, 41969–1 (cit. on pp. 17, 27, 36, 39).

(31) Sattler, R., Wagner, C., and Eggers, J., (2008). Blistering pattern and formation of nanofibers in capillary thinning of polymer solutions. *Physical Review Letters 100*, 164502 (cit. on pp. 17, 39).

(32) Sharma, V., Haward, S. J., Serdy, J., Keshavarz, B., Soderlund, A., Threlfall-Holmes, P., and McKinley, G. H., (2015). The rheology of aqueous solutions of ethyl hydroxy-ethyl cellulose (EHEC) and its hydrophobically modified analogue (hmEHEC): Extensional flow response in capillary break-up, jetting (ROJER) and in a cross-slot extensional rheometer. *Soft Matter 11*, 3251–3270 (cit. on p. 17).

(33) Lu, F., Zhang, C., Kang, H., Huang, Y., and Liu, R., (2016). Extensional rheology of cellulose/NaOH/urea/H 2 O solutions. *Cellulose 23*, 2877–2885 (cit. on p. 17).

(34) Choi, H., Mitchell, J. R., Gaddipati, S. R., Hill, S. E., and Wolf, B., (2014). Shear rheology and filament stretching behaviour of xanthan gum and carboxymethyl cellulose solution in presence of saliva. *Food Hydrocolloids 40*, 71–75 (cit. on pp. 17, 30).

(35) Bohr, D., *Bericht zu den Testmessungen mit dem CaBER Funktionsmuster*; 08.10.2018; Internal Publication Anton Paar GmbH: 2018 (cit. on p. 18).

(36) Sachsenheimer, D., Hochstein, B., Buggisch, H., and Willenbacher, N., (2012). Determination of axial forces during the capillary breakup of liquid filaments–the tilted CaBER method. *Rheologica Acta 51*, 909–923 (cit. on pp. 20, 21, 39).

(37) Sachsenheimer, D., Hochstein, B., and Willenbacher, N., (2014). Experimental study on the capillary thinning of entangled polymer solutions. *Rheologica Acta 53*, 725–739 (cit. on pp. 20, 21, 28, 92).

(38) McKinley, G. H., (2005). Visco-elasto-capillary thinning and break-up of complex fluids. *Massachusetts Institute of Technology, HML Report* (cit. on p. 22).

(39) Bazilevskii, A., Entov, V., Lerner, M., and Rozhkov, A., (1997). Failure of polymer solution filaments. *Polymer Science SeriesAC/C of Vysokomolekuliarnye Soedineniia 39*, 316–324 (cit. on p. 25).

(*40*) Oliveira, M. S., and McKinley, G. H., (2005). Iterated stretching and multiple beads-on-a-string phenomena in dilute solutions of highly extensible flexible polymers. *Physics of Fluids 17*, 071704 (cit. on pp. 26, 27, 39).

(*41*) Clasen, C., Eggers, J., Fontelos, M. A., Li, J., and McKinley, G. H., (2006). The beads-on-string structure of viscoelastic threads. *Journal of Fluid Mechanics 556*, 283–308 (cit. on p. 26).

(*42*) Chang, H.-C., Demekhin, E. A., and Kalaidin, E., (1999). Iterated stretching of viscoelastic jets. *Physics of Fluids 11*, 1717–1737 (cit. on p. 27).

(*43*) Klein, C. O., Naue, I. F., Nijman, J., and Wilhelm, M., (2009). Addition of the force measurement capability to a commercially available extensional rheometer (CaBER). *Soft Materials 7*, 242–257 (cit. on p. 28).

(*44*) Huang, Q., and Rasmussen, H. K., (2019). Extensional flow dynamics of polystyrene melt. *Journal of Rheology 63*, 829–835 (cit. on p. 28).

(*45*) Andrade, R., Harris, P., and Maia, J., (2014). High strain extensional rheometry of polymer melts: Revisiting and improving the Meissner design. *Journal of Rheology 58*, 869–890 (cit. on p. 28).

(*46*) Bach, A., Rasmussen, H. K., and Hassager, O., (2003). Extensional viscosity for polymer melts measured in the filament stretching rheometer. *Journal of Rheology 47*, 429–441 (cit. on p. 28).

(*47*) Huang, Q., Mangnus, M., Alvarez, N. J., Koopmans, R., and Hassager, O., (2016). A new look at extensional rheology of low-density polyethylene. *Rheologica Acta 55*, 343–350 (cit. on pp. 28, 29).

(*48*) Liang, J.-Z., and Zhong, L., (2011). Elongation properties of polyethylene melts. *Polymer Engineering & Science 51*, 2490–2494 (cit. on p. 28).

(*49*) Hachmann, P., Multiaxiale dehnung von polymerschmelzen., Ph.D. Thesis, Multiaxiale Dehnung von Polymerschmelzen, ETH Zurich, 1996 (cit. on p. 28).

(*50*) Nielsen, J. K., and Rasmussen, H. K., (2008). Reversed extension flow. *Journal of non-Newtonian Fluid Mechanics 155*, 15–19 (cit. on p. 28).

(51) Sur, S., Chellamuthu, M., and Rothstein, J., (2019). High-temperature extensional rheology of linear, branched, and hyper-branched polycarbonates. *Rheologica Acta 58*, 557–572 (cit. on p. 28).

(52) Feng, Y., Liu, J., Wang, S.-Q., Ntetsikas, K., Avgeropoulos, A., Kostas, M., and Mays, J., (2019). Exploring rheological responses to uniaxial stretching of various entangled polyisoprene melts. *Journal of Rheology 63*, 763–771 (cit. on p. 28).

(53) James, D. F., McLean, B. D., and Saringer, J. H., (1987). Presheared extensional flow of dilute polymer solutions. *Journal of Rheology 31*, 453–481 (cit. on p. 29).

(54) Park, A. E., Extensional viscosity of complex fluids and the effects of pre-shear., Ph.D. Thesis, Extensional Viscosity of Complex Fluids and the Effects of Pre-Shear, Massachusetts Institute of Technology, 2003 (cit. on p. 29).

(55) Bhardwaj, A., Richter, D., Chellamuthu, M., and Rothstein, J. P., (2007). The effect of pre-shear on the extensional rheology of wormlike micelle solutions. *Rheologica Acta 46*, 861–875 (cit. on pp. 29, 30).

(56) Day, L., and Golding, M., (2016). Food structure, rheology, and texture. *Encyclopedia of Food Chemistry* (cit. on p. 30).

(57) Torres, M., Hallmark, B., and Wilson, D., (2015). Effect of bubble volume fraction on the shear and extensional rheology of bubbly liquids based on guar gum (a Giesekus fluid) as continuous phase. *Journal of Food Engineering 146*, 129–142 (cit. on p. 30).

(58) Chesterton, A., Meza, B., Moggridge, G., Sadd, P., and Wilson, D., (2011). Rheological characterisation of cake batters generated by planetary mixing: elastic versus viscous effects. *Journal of Food Engineering 105*, 332–342 (cit. on p. 30).

(59) Norton, I. T., Spyropoulos, F., and Cox, P., *Practical Food Rheology: An Interpretive Approach*; John Wiley & Sons, UK: 2010 (cit. on p. 30).

(60) Weinstein, S. J., and Ruschak, K. J., (2004). Coating flows. *Annual Review of Fluid Mechanics 36*, 29–53 (cit. on p. 31).

(61) M.S. Owens, L. E. S., C. W. Macosko (2004). Rheology and Process Control Minimize Misting. *Presented at the 12th International Coating Science and Technology Symposium; Rheology and Process Control Minimize Misting* (cit. on p. 31).

(62) Azad, M. S., Dalsania, Y. K., and Trivedi, J. J., (2018). Capillary breakup extensional rheometry of associative and hydrolyzed polyacrylamide polymers for oil recovery applications. *Journal of Applied Polymer Science 135*, 46253 (cit. on p. 32).

(63) Speight, J. G., *Heavy Oil Recovery and Upgrading*; Gulf Professional Publishing, Laramie: 2019 (cit. on p. 32).

(64) (visited on 09.12.2020)., `https://www.anton-paar.com/at-de/produkte/details/rheometer-dma-mcr-702-multidrive/` (cit. on p. 35).

(65) Pfeifer, G., *Reflektoraufsatz für die kegelstab-Beleuchtung in der CTD-Kammer*; 27.04.2020; Internal Publication Anton Paar GmbH: 2020 (cit. on p. 38).

(66) Sousa, P. C., Vega, E. J., Sousa, R. G., Montanero, J. M., and Alves, M. A., (2017). Measurement of relaxation times in extensional flow of weakly viscoelastic polymer solutions. *Rheologica Acta 56*, 11–20 (cit. on p. 39).

(67) Sridhar, T., Acharya, M., Nguyen, D. A., and Bhattacharjee, P. K., (2014). On the extensional rheology of polymer melts and concentrated solutions. *Macromolecules 47*, 379–386 (cit. on p. 39).

(68) Tuladhar, T., and Mackley, M., (2008). Filament stretching rheometry and break-up behaviour of low viscosity polymer solutions and inkjet fluids. *Journal of non-Newtonian Fluid Mechanics 148*, 97–108 (cit. on p. 39).

(69) Omidvar, R., Dalili, A., Mir, A., and Mohammadigoushki, H., (2018). Exploring sensitivity of the extensional flow to wormlike micellar structure. *Journal of non-Newtonian Fluid Mechanics 252*, 48–56 (cit. on p. 39).

(70) Pfeifer, G., *Beleuchtung für die Anwendung CaBER*; 04.08.2020; Internal Publication Anton Paar GmbH: 2020 (cit. on p. 44).

(71) International, A., *Materials and Coatings for Medical Devices Cardiovascular: MPMD Materials and Processes for Medical Devices*; ASM International, United States of America: 2009 (cit. on p. 59).

(72) Liang, R., and Mackley, M., (1994). Rheological characterization of the time and strain dependence for polyisobutylene solutions. *Journal of non-Newtonian Fluid Mechanics 52*, 387–405 (cit. on p. 59).

(73) Bailey, F. J., *Poly(ethylene oxide)*; Elsevier, New York: 2012 (cit. on p. 60).

(74) Turowec, B. A., and Gillies, E. R., (2017). Synthesis, properties and degradation of polyisobutylene–polyester graft copolymers. *Polymer International 66*, 42–51 (cit. on pp. 61, 98).

(75) Schultheisz, C., and Leigh, S., (2001). NIST Special publication 260-143. *NIST Special publication 260-143* (cit. on pp. 62, 113).

(76) Parker, G., *Encyclopedia of Materials: Science and Technology*; Elsevier, Pergamon: 2001 (cit. on p. 62).

(77) Sastri, V., (2010). Chapter 6-Commodity Thermoplastics: Polyvinyl Chloride, Polyolefins, and Polystyrene. *Plastics in Medical Devices*, 73–119 (cit. on p. 63).

(78) Kim, M. W., (1997). Surface activity and property of polyethyleneoxide (PEO) in water. *Colloids and Surfaces A: Physicochemical and Engineering Aspects 128*, 145–154 (cit. on pp. 68, 94).

(79) Grubisic, Z., Rempp, P., and Benoit, H., (1967). A universal calibration for gel permeation chromatography. *Journal of Polymer Science Part C: Polymer Letters 5*, 753–759 (cit. on p. 113).